CFD Simulation of Reactant Transport Limitations in Low-Temperature Fuel Cells

By Usman Ahmad

Supervised by Dr. Sheikh Zahidul Islam

MSc Mechanical Engineering and Sustainable Energy Technologies

May 2026

School of Digital, Technologies and Arts
Department of Engineering

University of Staffordshire

Abstract

Proton Exchange Membrane fuel cells are regarded as a promising technology for transportation, distributed power generation or portable applications because they provide direct conversion of hydrogen into electrical energy and generate only water as by-product. However, their commercial deployment is restricted due to the limitations of reactant transport during operation under high current density in the cathode flow channel, where the rate of the oxygen consumption at the catalyst layer is faster than the rate of the diffusive supply through the gas diffusion layer (GDL), and a significant loss of concentration in the polarisation curve is observed. Though it has been proposed that the dominant transport mechanism can be changed from molecular diffusion to forced convection by introducing baffles in the cathode flow channel, a systematic three dimensional study on Rectangular Baffle height in cathode only baffled straight channel has not been reported in the open literature, along with detailed static pressure and velocity distribution in GDL, CL and Baffle region. This study aimed to explore the limitations in the transport of reactants in a low-temperature PEM fuel cell by reducing oxygen transport limitations at the cathode side of fuel cell under high current density operation through systematic study of the effect of varying rectangular baffle height using computational fluid dynamics by ANSYS, in which single-phase, steady-state model was created in ANSYS Fluent. The model was indirectly validated by comparing the results with those of the published numerical and experimental work, and numerical convergence was achieved by performing a mesh independence study on 122,300, 220,000 and 500,200 element meshes. Parametric sweeps on inlet relative humidity at four levels, GDL porosity at three levels between 0.4 and 0.8, GDL permeability at three levels between 1.76×10^{-8} and 1.76×10^{-12} m^2, number of baffles between 0 and 4 and baffle height between 0.2 mm and 0.5 mm were then performed. It was found that as inlet humidity was increased from very low to very high, the limiting current density was increased from about 0.35 A/cm2 to 1.05 A/cm2 while the power peak density was increased from 0.09 W/cm2 to 0.276 W/cm2 (211%). It was found that 0.8 porosity of GDL was larger than 0.4 porosity that can increase the limiting current density from ~1.0 to 1.08 A/cm2, but above 0.6 porosity, increase rate is reduced. The velocity of the cathode GDL and catalyst layer showed almost linear dependence upon the baffle number with the maximum velocity of 0.01478 m/s and 0.01231 m/s available at 0.5 mm baffle height, 4 baffles, which represented an enhancement of 377.1% and 475.4% over the baseline without baffle. Based on this, it was determined that the optimal geometry among the range of parameters tested was the configuration of four rectangular baffles, 10 mm deep and 0.5 mm high.

Acknowledgements

I would like to thank my supervisor, **Dr. Sheikh Zahidul Islam** for his mentoring, inspiration and support during this work. His wealth of knowledge and guidance were critical for the successful completion of this thesis.

His feedback and feedback questions throughout the project assisted in the development of my critical thinking skills and improved my problem-solving skills. His invaluable technical guidance in tackling the complexities of computational fluid dynamics, as well as the unwavering support to keep forging ahead in the rigours of postgraduate research, were greatly appreciated.

I am especially grateful for his availability and for being so generous with his time, knowledge and understanding. He has been a constant source of inspiration and guidance.

I am immensely grateful to have been able to learn at his feet. His outstanding mentorship and support are a critical element in bringing this work to its current stage.

Table of Contents

LIST OF FIGURES

LIST OF TABLES

Nomenclature

A – specific area of the anode / cathode catalyst layer (m^{-1})

a_k water activity

C molar concentration of species (mol m^{-3})

CAD – Computer Aided Design

CL – Catalyst Layer

D diffusion coefficient of species (m^2 s^{-1})

E equilibrium thermodynamic potential (V)

F Faraday constant (96485.309 C mol^{-1})

FCEV – Fuel Cell Electric Vehicle

FEA – Finite Element Analysis

GDL – Gas Diffusion Layer

H height (m)

HH – High Humidity

Hlp – Half of ellipse

HOR – Hydrogen Oxidation Reaction

I average current density (Acm^{-2})

IEA – Internation Energy Agency

I-Hlp – Inverted half of ellipse

I-Trp – Inverted Trapeze

K – Permeability

K permeability of porous layers (m^2)

LH – Low Humidity

M molar mass (kg mol^{-1})

MEA – Membrane Electrode Assembly

$M_{m,dry}$ – dry mass of membrane (Kg mol^{-1})

ORR – Oxygen Reduction Reaction

P – Pressure (Pa)

PEMFC – Proton Exchange Membrane Fuel Cell

R gas constant (8.314 J mol-1 K-1)

Rct – Rectangular

s liquid water saturation

S source term

SIMPLE – Semi-Implicit Method for Pressure-Linked Equations

T temperature (K)

tm thickness of membrane (m)

Trg – Triangular

Trp – Trapeze

$\boldsymbol{u}$ velocity vector (m s-1)

UDF – User-Defined Function

$Vcell$ cell voltage (V)

VHH – Very High Humidity

VLH – Very Low Humidity

W width (m)

X molar fraction

Subscripts and Superscripts

0 – before diffusion layer

a – anode

act – activation

av – average

c – cathode

conc – concentration

d – diffusion layer

eff – effective

el – electron

H_2 – hydrogen

k – species

L – limiting

lq – liquid

m – membrane

O_2 – oxygen

ohm – ohmic polarization

pro – proton

ref – reference

sat – saturation

wv – water vapour

Greek Symbols

α net water transfer coefficient

ε – *porosity*

η – overpotential (V)

μ – viscosity (kg m^{-1} s^{-1})

ρ – density (kg m^{-3})

ω – species mass fraction

ζ – stoichiometric ratio

Chapter 1: Introduction

The growing world energy needs, attributed to industrialization and technological progress, have fuelled an interest in the concept of environmental sustainability and the exhaustion of fossil fuel reserves. International Energy Agency (IEA, 2025) estimates that the world primary energy demand is about 14,800-15,000 million tonnes of oil equivalent (Mtoe). The world still relies heavily on fossil fuels, with most of the energy used by oil (~4,400 Mtoe), coal (~3,900 Mtoe), and natural gas (~3,100 Mtoe). Nuclear (~700 Mtoe), hydropower (~400 Mtoe), and modern renewables (~1,800-2,000 Mtoe) sources are considered as low-carbon, and these sources include wind, solar, bioenergy, and various other emerging technologies.

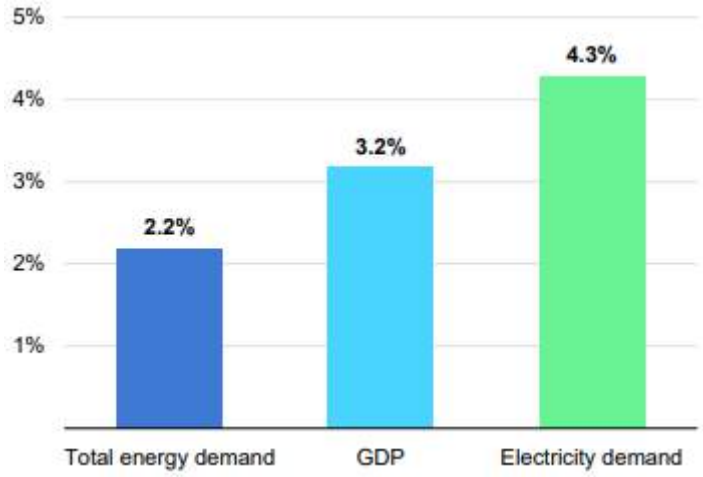

Figure 1 Key Global Growth Rates 2024 (IEA, 2025)

Traditional energy sources which involve combustion of fossil fuels are a major contributor to greenhouse gases and global warming. Consequently, there has been an increasing demand on clean, efficient and sustainable energy conversion technologies. Among others, fuel cells have become a possible solution, being highly efficient and environmentally friendly to operate (Hossain, Islam and Pollard, 2012).

Polymer Electrolyte Membrane (PEM) fuel cells have been regarded as one of the most appropriate technologies to adopt as a future energy system since they directly transform chemical energy into electrical energy with the least environmental impact and offering zero-emission power solutions of high efficiency and high-power densities (Yi et al., 2025). PEM fuel cells are a clean energy technology unlike the conventional systems, which rely on combustion reactions to generate electricity and water is the main by product (Hossain et al., 2013).

PEM fuel cells are of special interest because they have low operating temperature, high efficiency, fast start-up, compact design making it applicable in a large variety of uses such as transportation, portable power systems, and stationary energy production (Dutta, Shimpalee and Van Zee, 2001; Hossain et al., 2013). These attributes make PEM fuel cells the promising energy sources of the next generation in automobiles and distributed energy systems. Nonetheless, the high price, poor durability and performance remain some of the challenges that limit the wide use of PEM fuel cells. The expensive nature can be mostly linked to the fact that platinum catalysts are used in the electrode layers, and the performance constraints are usually related to transport effects like distribution of reactants and water in the cell (Hossain, Islam and Pollard, 2012; Hossain et al., 2013).

1.1 Working Principle of PEM Fuel Cells

A proton exchange membrane fuel cell (PEMFC) is operated on the principle of converting chemical energy into electrical energy through an electrochemical process, in which hydrogen fuel is directly turned into electrical energy, with water and heat as by-products. An average PEMFC is an anode, cathode, proton exchange membrane (PEM), gas diffusion layers (GDLs), and catalyst layers (CLs) (Pu et al., 2026).

Hydrogen gas is introduced to the anode side and oxygen (or air) is passed to the cathode via the appropriate flow channels during operation. The flow field is used to spread the reactant gases over and diffuse through the porous gas diffusion layers to the catalyst layers. Hydrogen is oxidized in the anode catalyst layer, where it reacts to give protons and electrons. The protons travel across the proton exchange membrane that is a solid electrolyte that only facilitates the transfer of ions, and not gases (Nair, Lal and Vangala, 2025; Jinyuan et al., 2024; Eikerling and Kulikovsky, 2014).

The electrons produced at the anode are unable to travel across the membrane and thus they are compelled to travel outside electrical circuit producing useful electricity power before reaching the cathode. It is at the cathode catalyst layer that the oxygen reacts with the protons and electrons that come in to produce water. It is an exothermic electrochemical reaction and, because of this process, heat is released, not just electricity (Nair, Lal and Vangala, 2025; Jinyuan et al., 2024; Eikerling and Kulikovsky, 2014).

In general, the operation of a PEMFC is influenced by the good convection of reactants to the catalysts, the good evacuation of products like water, and the ionic and electrical conduction in the cell. These are coupled electrochemical and transport processes which

determine the efficiency and characteristics of operation of the fuel cell. The working principle of PEM Fuel Cell is shown in Figure 2.

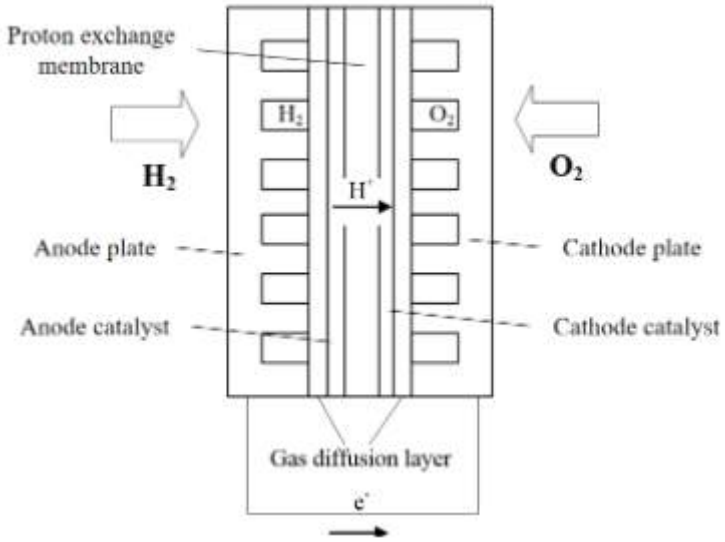

Figure 2 Working Principle of PEM Fuel Cell (Pu et al., 2026)

1.2 Baffles in PEM Fuel Cells

Mass transport of reactants in the gas diffusion layer (GDL) and catalyst layer (CL) of proton exchange membrane (PEM) fuel cells is a key factor in optimising fuel cell performance. Flow channel structure is an important factor in water, heat and mass transport in PEMFCs, as the flow field structure of a PEMFC can enhance mass transfer between the flow channels and gas diffusion layers, improve water and thermal management, and boost power density (Jiang et al., 2023). A major focus of PEM fuel cell design is to address mass transport issues, especially at higher current densities where the supply of oxygen to the catalyst layer of the cathode is the limiting factor. To overcome this, the use of baffles in the flow channel has been proposed as a passive flow modification technique. The inclusion of baffles to block gas flow in the flow field has been shown to enhance PEMFC performance, as baffles enhance the transport of the reactants by forcing them into the gas diffusion layer, and help to remove excess liquid water (Deng et al., 2022).

Different baffle shapes have been studied, such as trapezoidal, semicircular, wavy and rectangular, with varying benefits and drawbacks in terms of mass transport improvement and pressure drop increase. Among rectangular, trapezoidal, and semicircular baffles, rectangular baffles have been demonstrated to result in the highest oxygen mass fraction

at the cathode catalyst layer-GDL interface, with more uniform distributions of oxygen than trapezoidal and semicircular baffles (Wei et al., 2025). In addition, numerical investigations of different baffle structures have shown that the rectangular baffle makes the greatest contribution to the enhancement of performance (Chen et al., 2020) and is therefore a reasonable choice for studies of optimisation of reactant transport.

As such, this paper employs rectangular baffles in the cathode flow channel, and baffle height as the primary geometric variable of interest. Baffle height in the flow field greatly influences mass species distribution, current density and power density, and compared to the conventional straight channel, optimised baffle height can enhance cell performance (Li, Zhang and Shen, 2025). A greater number of baffles and an optimised configuration led to increased mass flux and better reactant distribution uniformity (Ghasabehi et al., 2024), thereby emphasising that design parametric studies on baffle dimensions are a valuable and successful research strategy. In this study, the impact of different heights of the rectangular baffles on species transport in PEM fuel cells is examined and the optimal baffle configuration, which improves oxygen delivery to the catalyst layer without excessive pressure drop, is determined. Complications in Efficient Fuel Design.

1.3 Polarisation Characteristics

In a proton exchange membrane fuel cell, the electrical energy conversion is affected by simultaneous half-cell reactions. The oxidation of hydrogen to yield protons and electrons occurs at the anode and the reduction of oxygen to water occurs at the cathode. The ideal (open circuit) voltage is about 1.23 V, but in practice, the voltage drops below this value as current is withdrawn from the cell, due to three types of irreversible losses.

$$Anode: H_2 \rightarrow 2H^+ + 2e^-$$

$$Cathode: 1/2\, O_2 + 2H^+ + 2e^- \rightarrow H_2O$$

$$Overall\ Reaction: H_2 + 1/2\, O_2 \rightarrow H_2O + electrical\ energy + waste\ heat$$

The activation overpotential(η_{act}) is due to the limited reaction rate of the electrochemical reactions. The O_2 reduction reaction at the cathode side is slower than the H_2 oxidation reaction at the anode side due to more complicated electron transfer process and thus, the overall activation loss is mainly determined by the cathode. This overpotential is related to the local current density, local exchange current density and oxygen concentration at the catalyst (Hossain, Islam and Pollard, 2012).

The ohmic overpotential(η_{ohm}) is caused by the membrane resistance to proton transport, and the resistance of porous electrodes to electron transport, and rises with an increase in current density.

The concentration overpotential(η_{conc}) is significant at higher current densities where the rate of the reaction occurring at the cathode catalyst layer is greater than the rate at which oxygen can be delivered to the catalyst layer by diffusion through the porous gas diffusion layer (GDL) resulting in a concentration gradient, which subsequently reduces the driving force for the reaction and determines the maximum attainable current density.

1.4 Challenges in Efficient Fuel Cell Design

Proton exchange membrane fuel cells (PEMFC) represent a promising clean energy source due to their low operating temperature, quick start-up and zero emissions. But they still face several challenges that limit their effective design and commercialisation. These include the ongoing technological hurdles in water management, membrane stability and catalyst efficiency (Jiang et al., 2023), which are all intricately tied to the effective distribution of reactants over the active region of the cell.

Mass Transport Limitations

Low reactant transport is one of the major challenges for high performance PEMFCs, especially at high current density when oxygen transport to the cathode catalyst layer becomes the rate-limiting step. Flow field structure is a critical component of water, thermal and mass transport in PEMFCs, and a properly designed flow field structure can allow for mass transfer between the flow channels and gas diffusion layers, improve water and thermal management, and enhance power density (Ghasabehi et al., 2024). In the classical straight channel, diffusion is the only mode of reactant transport into the GDL and the process is slow, resulting in an uneven distribution of oxygen over the active area. Passive structural modifications like baffles have been shown to be effective at increasing forced convection in the flow channel, converting the longitudinal momentum to a flow through the GDL and thereby improving reactant transport to the catalyst layer.

Reactant and Water Management

Water management is critical for reactant delivery in PEM fuel cells. Cathodic water production can accumulate in GDL pores and flow channels, obstructing the path of oxygen to the catalyst. Excessive and/or deficient water can damage the system, so

accurate water management methods such as novel flow field designs are vital for optimal PEMFC performance. (Xu et al., 2022) Variations in flow field designs affect flooding, which further affects the mass transport of oxygen in the cathode diffusion layer. Cathode-side baffles with rectangular shapes improve water removal via convection, while also increasing through-plane oxygen transport, solving the twin issues of flooding and reactant starvation with a single design change.

Concentration Polarisation

Concentration polarisation occurs when the local oxygen concentration at the catalyst surface is well below the bulk concentration in the flow channel due to the low diffusion rates through the GDL and becomes the major loss at high current densities. Baffles in the flow channel that obstruct the flow of gases have been shown to be an effective way of enhancing the performance of PEMFCs as baffles enhance reactant transport by forcing the gas into the gas diffusion layers. (Abubakar Unguwanrimi Yakubu et al., 2024). In addition, in the absence of baffles, reactant concentration is not uniform between the channel inlet and outlet, leading to current density distribution non-uniformity. A partially blocked channel has a more uniform distribution of reactants than a fully blocked channel and overcomes the issue of large pressure drop (Abubakar Unguwanrimi Yakubu et al., 2024).

Baffle Height Optimisation and Flow Field Design

Baffle design, and particularly its height, controls the level of forced convection and reactant transport into the GDL. Baffle heights in the flow field greatly influence species concentration, current density and power density, and compared to the conventional straight flow channel, with optimised baffle heights, cell performance can be improved (Deng et al., 2022). Consequently, it is important to optimise flow field modifications to improve reactant transport with minimal flow resistance. Rectangular baffles have been shown to be most effective in terms of oxygen mass fraction at the cathode CL-GDL interface, with the most uniform distribution compared to trapezoidal, and semi-circular baffles (Kaiser et al., 2023). Therefore, optimising height of rectangular baffles, as studied here, is a logical strategy to enhance reactant transport, and ultimately, cell performance.

1.5 Research Aims and Objectives

Aims:

The aim of this study was to study the transportation restrictions of the reactants in a low-temperature proton exchange membrane fuel cell using a three-dimensional computational fluid dynamic model to enhance the performance and the distribution of oxygen at the cathode side of the fuel cell during its operation at high current density.

Objectives:

- To critically assess the literature regarding design implications of PEM fuel cells, focusing on transport limitation, water management and modifying flow field geometries at the cathode side.
- To build and validate a three-dimensional, steady-state and single-phase numerical model of a full-sized PEM fuel cell with a parallel transport channel in ANSYS Fluent.
- To study the impact of inlet relative humidity on fuel cell performance through a parametric investigation with four different humidity levels, and to analyse the corresponding performance curves for voltage versus current and power versus current density.
- To assess the effect of gas diffusion layer (GDL) porosity and permeability on oxygen transport (oxygen concentration lean) and polarisation characteristics to validate the choice of GDL properties for the baseline baffle simulations.
- To disturb the cathode flow channel by placing rectangular baffles of different heights in it and to investigate the influence of baffle height on the static pressure, velocity, and through-plane transport of reactants in the gas diffusion layer and catalyst layer zones.
- To compare the pressure drop characteristics and velocity distribution in the baffle, GDL and catalyst layer regions for each baffle height, leading to optimal selection of the rectangular baffle height that provides maximum oxygen transport in the cathode with acceptable pressure drop values.

Chapter 2: Literature Review

Proton exchange membrane fuel cells (PEMFCs) have received significant and increasing attention in the last 20 years as a leading clean energy conversion technology. As reported by (Wang et al., 2022), PEMFCs have an efficiency of up to 65% and generate water as the sole product when hydrogen is used as fuel and have been successfully applied in fuel cell electric vehicles, stationary power and portable devices. Bibliometric analysis of Scopus-cited papers from 2000 to 2021 revealed over 31,500 research papers related to PEMFC technology, with the International Journal of Hydrogen Energy and Journal of Power Sources accounting for almost 27% of the global publication share. The top contributing countries - the United States, China, Canada, Germany, and France - demonstrate significant interests from industry and considerable government investment in research initiatives focused on the development of hydrogen infrastructure.

Other researchers have noted that to 2021 more than 10,000 fuel cell electric vehicles had been sold or leased in the US and more than 3,520 in Japan, indicating a move towards commercialisation (Wang et al., 2022). According to (Zhao, Tu and Chan, 2021), the bipolar plate represents about 70% of the PEMFC stack weight and 30% of the stack cost, making flow field design one of the most important economic design factors for the system. As a result, attention has been paid to all cell subsystems: membranes, catalyst layers, gas diffusion layers, and flow fields in bipolar plates, but especially flow fields because they are the only part of the cell design which can be directly optimised through numerical analysis, and they have a primary impact on reactant distribution, pressure drop, and hence, electrochemical performance.

Computational fluid dynamics (CFD) modelling has emerged as the most common approach to this type of research, with ANSYS FLUENT being the software of choice due to its PEMFC module, which couple's species transport, electrochemical kinetics, charge conservation, and heat transfer in a single simulation domain. Of the modelling strategies pursued, single-phase steady-state modelling, whereby water generated at the cathode is assumed to be present in vapour form and liquid water accumulation is neglected, has been widely adopted as an efficient and sound modelling framework for investigating reactant transport, velocity and pressure distributions in traditional and modified flow channel designs, especially at low to moderate current densities.

2.1 Single-Phase PEM Fuel Cells

The straight parallel channel is the baseline PEMFC flow channel geometry that is used as a point of reference for channel design and modification. The first single-phase three-dimensional CFD models of straight-channel PEMFCs were highly influential in describing the governing physics of reactant transport. However, it is widely reported that at high current densities the conventional straight parallel channels experience severe reactant depletion and sluggish convective transport towards catalyst layer which is seen as a large drop in polarisation curve concentration-loss region and the accumulation of product water in these GDLs clogs the GDL pores and restricts oxygen from reaching the active sites.

Since then, (SIVERTSEN and DJILALI, 2005) have developed a single-phase model to understand the three-dimensional coupled mass transport process and electrochemical reaction in PEM fuel cells with straight gas channels. They solved their model on a single computational domain, which included the gas channel, gas diffusion layer and catalyst layer of both the anode and cathode, and the solid polymer membrane. This work focused specifically on the influence of the three-dimensional flow structure in the air cathode on the electrochemical reaction, and demonstrated the model predicted cell performance over a moderate range of current densities reasonably well, based on a comparison with experimental polarisation curves as shown in Figure 3. Three-dimensional results for cathode flow structure and solution oxygen concentration showed that oxygen was depleted most in the sub-rib region (under the land between channels), which was the direct inspiration for the following modifications in the channel design. This sub-rib oxygen starving was noted as a key driver of the concentration overpotential and high voltage loss at higher current densities, when the rate of oxygen consumption at the catalyst layer was higher than the rate of diffusive supply from below the rib, through the GDL.

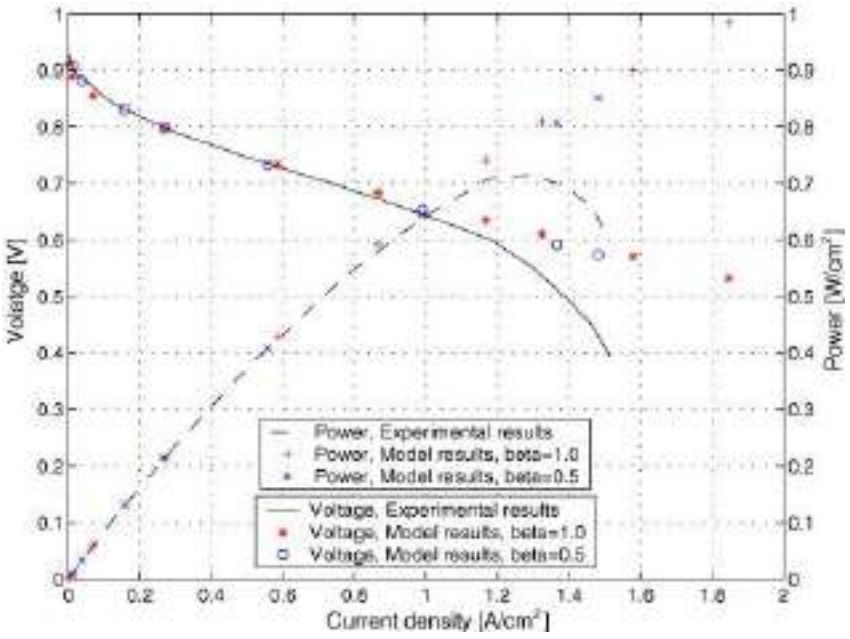

Figure 3 Polarisation Curves presented by (SIVERTSEN and DJILALI, 2005)

(Hashemi, Rowshanzamir and Rezakazemi, 2012) presented a detailed three-dimensional non-isothermal single-phase model to study and compare the performance of PEM fuel cells with straight and serpentine flow fields. They found that in the straight channel, distributions of oxygen and hydrogen mass fractions, current density and temperature were significantly affected by the geometry of the channel and activation overpotential distribution. The straight channel showed the strongest oxygen depletion along the axis of the channel, especially in the sub-rib zones, which led to non-uniform current density distribution with the maximum at the inlet and a decrease along the flow direction. This non-uniform current density distribution was also found to lead to localised heat generation and caused greater water build-up in the downstream regions, which tended to increase the voltage drop at higher current densities due to GDL flooding and partial channel blockage by liquid water drops. The serpentine flow field yielded more uniform current density due to the increased flow path length and the local pressure drop, but the straight channel was preferred for low-pressure-drop applications and to study the underlying transport phenomena. Comparisons with reported experimental results were made for both configurations to verify the single-phase modelling method. Some contours are shown in Figure 4.

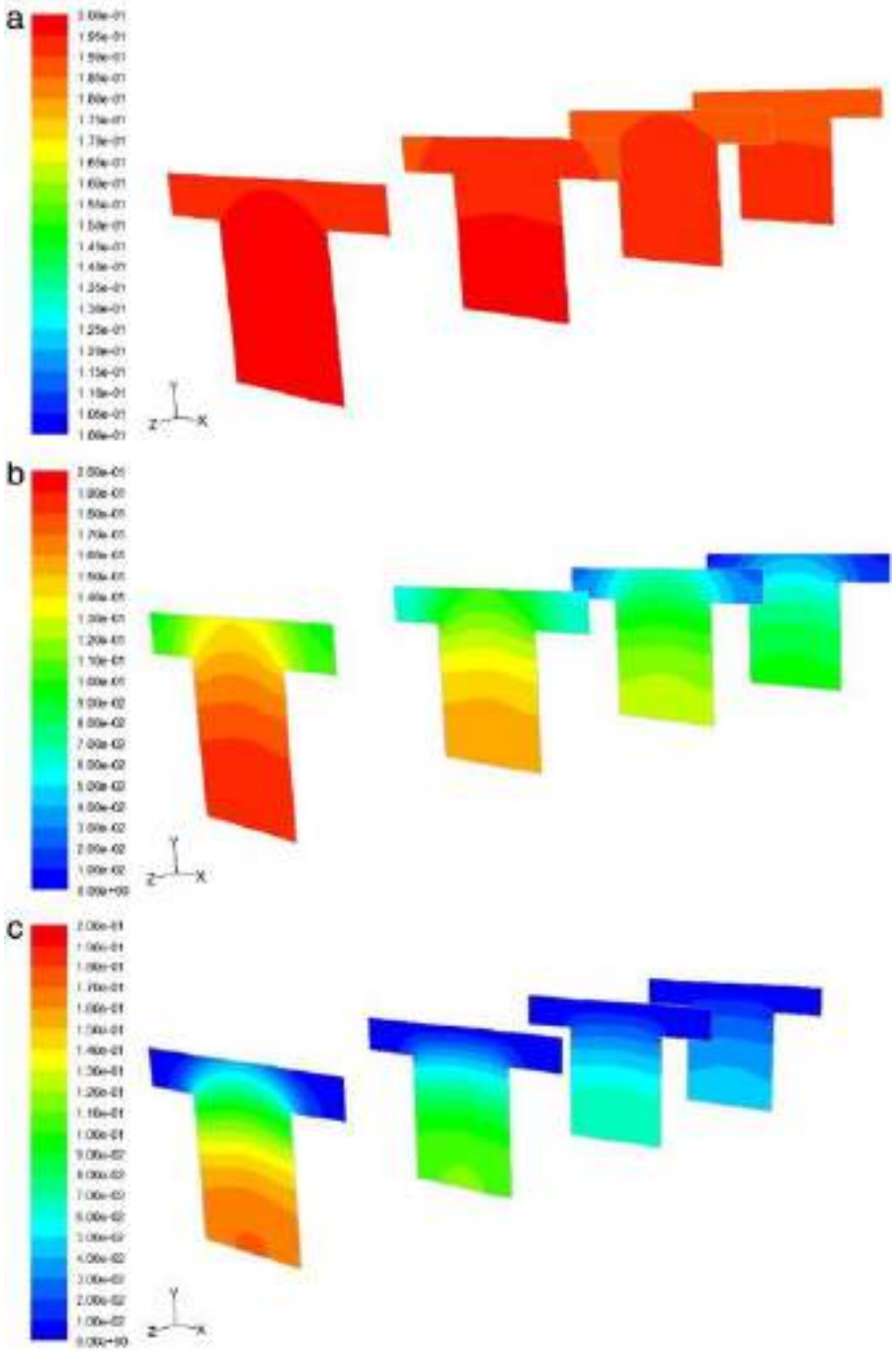

Figure 4 Oxygen Distribution in the PEM Fuel Cell at V=(a) 0.8V, (b) 0.6V, (c) 0.4V presented by (Hashemi, Rowshanzamir and Rezakazemi, 2012)

Others have also used straight-channel models to explore how channel cross-sectional shape affects the velocity distribution and reactant supply. (Mohammedi, Sahli and Ben Moussa, 2020) performed a full three-dimensional CFD study in ANSYS Fluent with six different cross-sectional shapes in a straight-channel PEMFC shown in Figure 5, and found the circular cross-section delivered the highest power density, with the rectangular cross-section being the most practical in terms of both performance and manufacturability.

Importantly, they found that the magnitude of the velocity at the surface of the GDL (and therefore the oxygen supply flux to the catalyst layer) was dependent on the cross-sectional geometry of the channel, despite identical inlet conditions for each geometry. The same study notes that low near-GDL velocities were correlated to inadequate convective removal of product water, which promoted the formation of liquid water films that blocked GDL pores and resulted in a sudden drop in voltage typically observed in the mass-transport-limited regime. This confirmed that velocity distribution is a key design-sensitive performance indicator in straight-channel PEMFC modelling. Other single-phase straight-channel parametric studies have demonstrated that current density is very sensitive to operating voltage, inlet mass flow rate and channel depth, whereas channel pressure drop is a function of channel aspect ratio and flow velocity. All of these drawbacks of the base-line straight parallel channel (sub-rib oxygen depletion, non-uniform current density and water-induced GDL flooding at high current densities) have been recognized as the key drivers to consider when implementing geometric changes – notably baffles, blocks, and tapered sections – in order to improve under-rib convection and reduce the associated concentration losses.

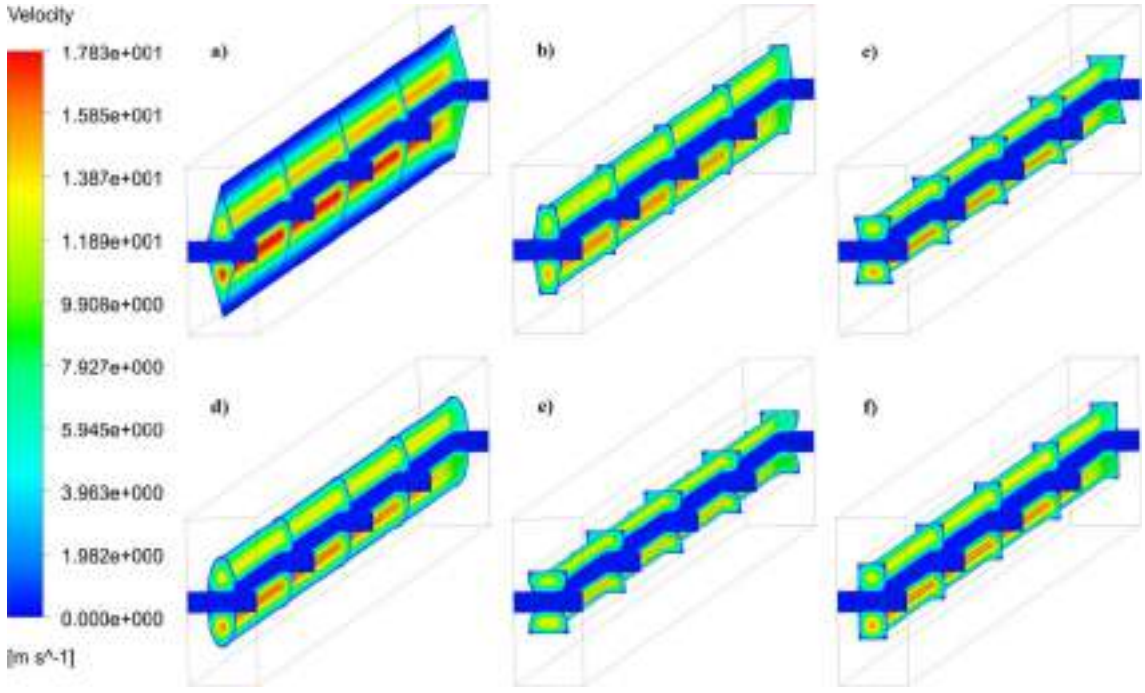

Figure 5 Velocity Fields presented by (Mohammedi, Sahli and Ben Moussa, 2020) on six different shapes (a) Trg (b) Trp (c) I-Trp (d) Hlp (e) I-Hlp (f) Rct

2.2 Baffles in PEM Fuel Cells

The use of baffles (transverse blockage plates) in a PEMFC flow channel was suggested as a purely passive structural design approach to address the transport limitation of straight channels which was limited by diffusion. (Soong et al., 2005) were among the first to propose a partially blocked flow channel with the baffle plates inserted transversely as shown in Figure 6 and noted that decreasing the baffle gap ratio and increasing the number of baffle plates improved the mass transport of reactant gas through the GDL, but with a penalty in pressure loss.

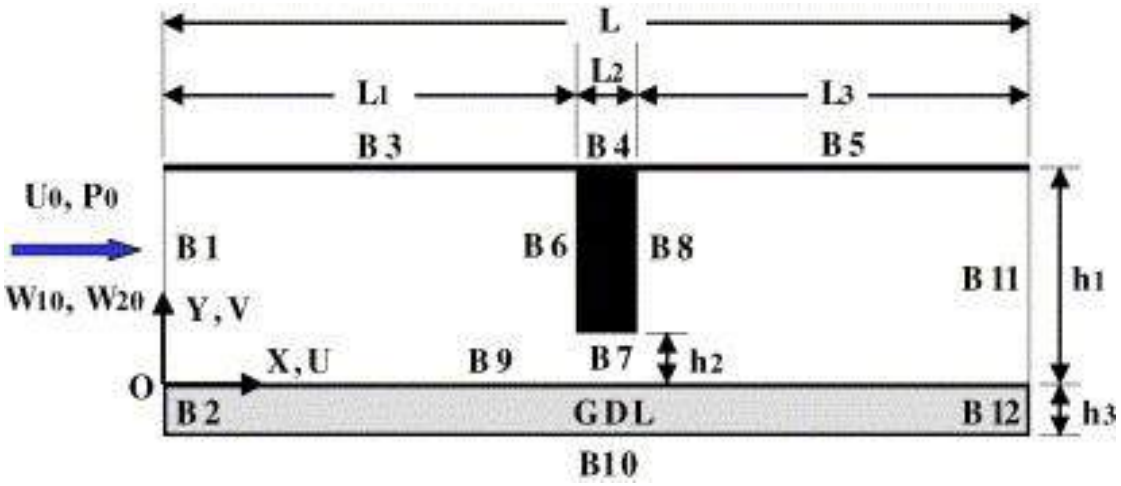

Figure 6 Half-cell model with baffles presented by (Soong et al., 2005)

This work identified the underlying physical basis: the partial blockage by the baffle induces a localised pressure drop between the upstream and downstream channel face, driving localised flow into the GDL and causing a perpendicular (to the channel flow) velocity component at the GDL surface and leading to increased reactant delivery to the catalyst layer (Figure 7).

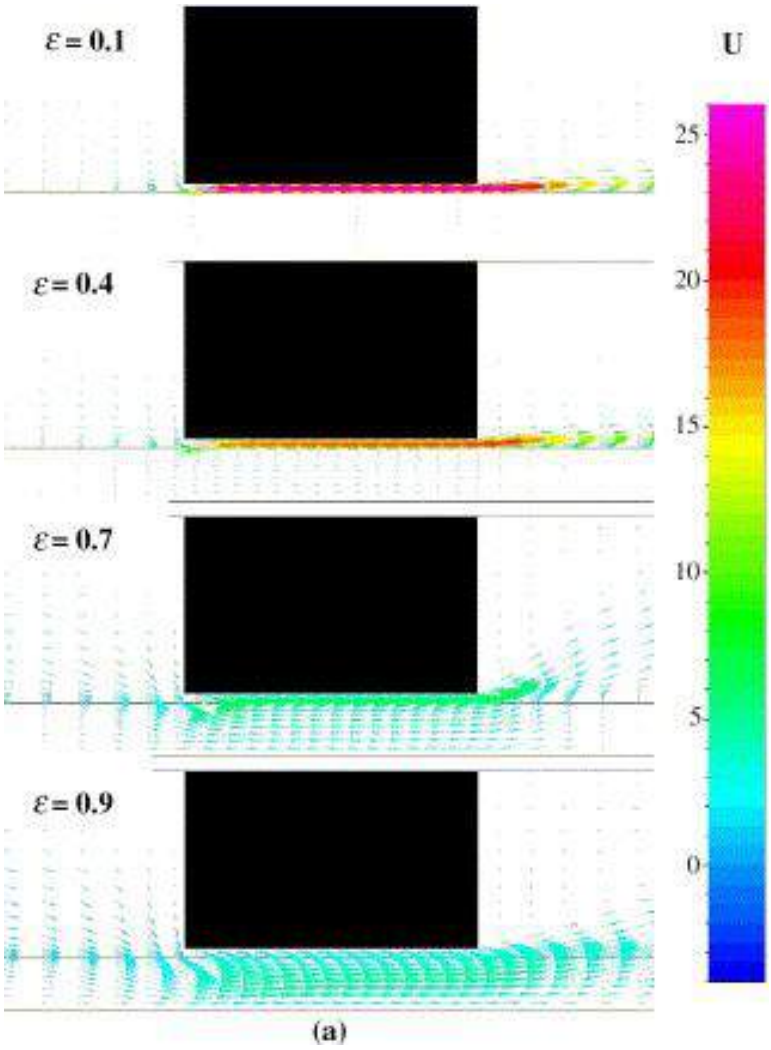

Figure 7 Views of the velocity vector field on the gap region of the baffle plate in the baffle-gap-GDL section of flow passage of a single baffle presented by (Soong et al., 2005)

They concluded that a minimum gap ratio of 0.1 with 3-5 plates was the optimal design considering both gas transport and pressure drop. (Yin et al., 2018) developed a three-dimensional PEMFC model with baffle plate (Figure 8) with user-defined functions to translate the conservation equations and physical properties.

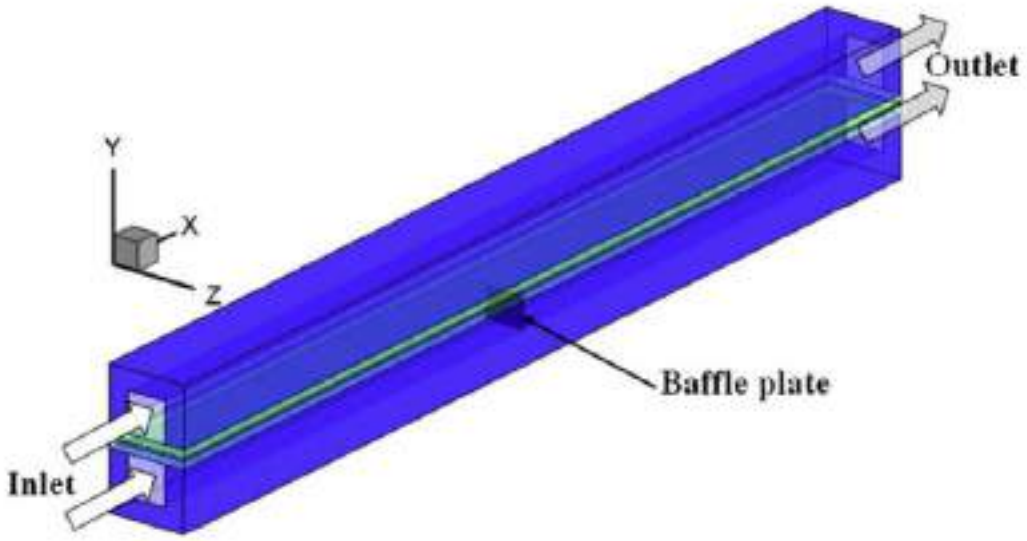

Figure 8 Model presented by (Yin et al., 2018)

Their findings demonstrated that baffles enhanced the local gas velocity in the channel, facilitated reactant distribution and water transport out of porous electrodes, enhanced the oxygen concentration in the GDL and reduced concentration overpotential. The number of baffles and their position along the flow channel significantly impacted oxygen distribution at the cathode GDL surface, with well-positioned plates achieving the best distributed oxygen component. Contours presented by (Yin et al., 2018) are shown in Figure 9 and 10.

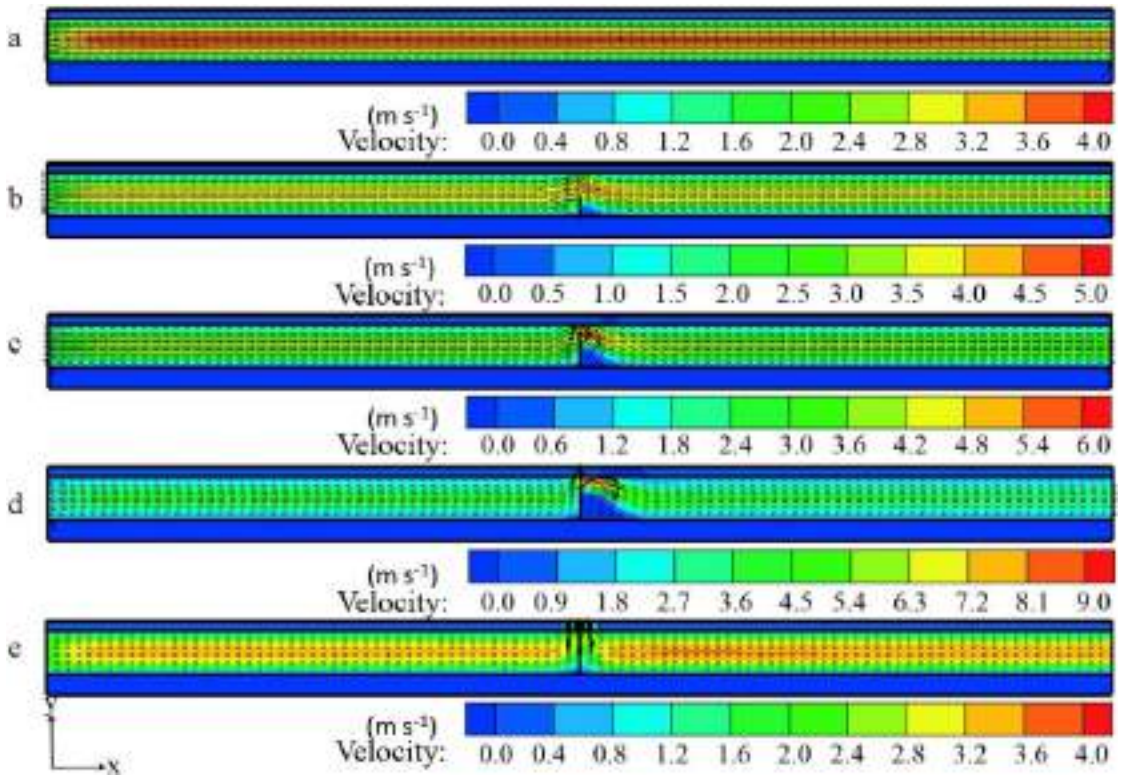

Figure 9 Impact on velocity by varying blockage ratio presented by (Yin et al., 2018)

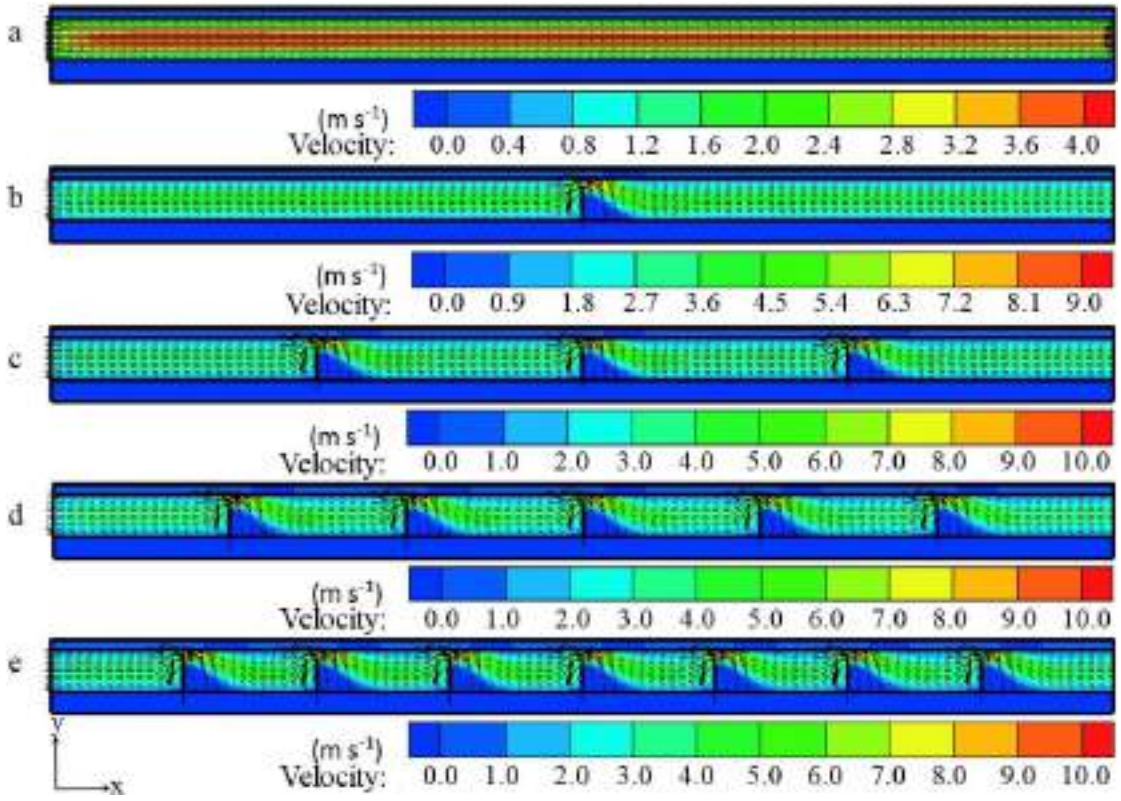

Figure 10 Impact of velocity by increasing the number of baffles presented by (Yin et al., 2018)

These numerical results were later confirmed in experimental measurements of a PEMFC with cathode side-blocked, straight flow channel by (Yin et al., 2018), who confirmed numerically and experimentally that baffles on the cathode side increased the local velocity component perpendicular to the GDL and increased the local oxygen concentration across the active area - offering essential experimental confirmation of the transport mechanism discovered in earlier numerical studies. The single most important geometric design factor for baffled flow fields is baffle height - which determines the degree of enforced through-plane convection to the GDL and the pressure drop along the channel.

(Perng and Wu, 2015) pioneered three-dimensional non-isothermal modelling of trapezoidal baffles, which found the optimal net power output (90% higher than that of the unbaffled straight flow channel) to be produced at a baffle inclination angle of 60° and a baffle height of 1.125 mm. They found that the through-plane GDL velocity increased dramatically at each baffle location, but that the dependence of performance on baffle height was non-linear and as the height exceeded the optimised value, the penalty from increased pressure drop began to outweigh the benefit for forced convection, and the net power output decreased. This non-linear interplay between baffle height, velocity increase, and pressure drop penalty has been independently verified by multiple sources as the key optimisation trade-off for baffles.

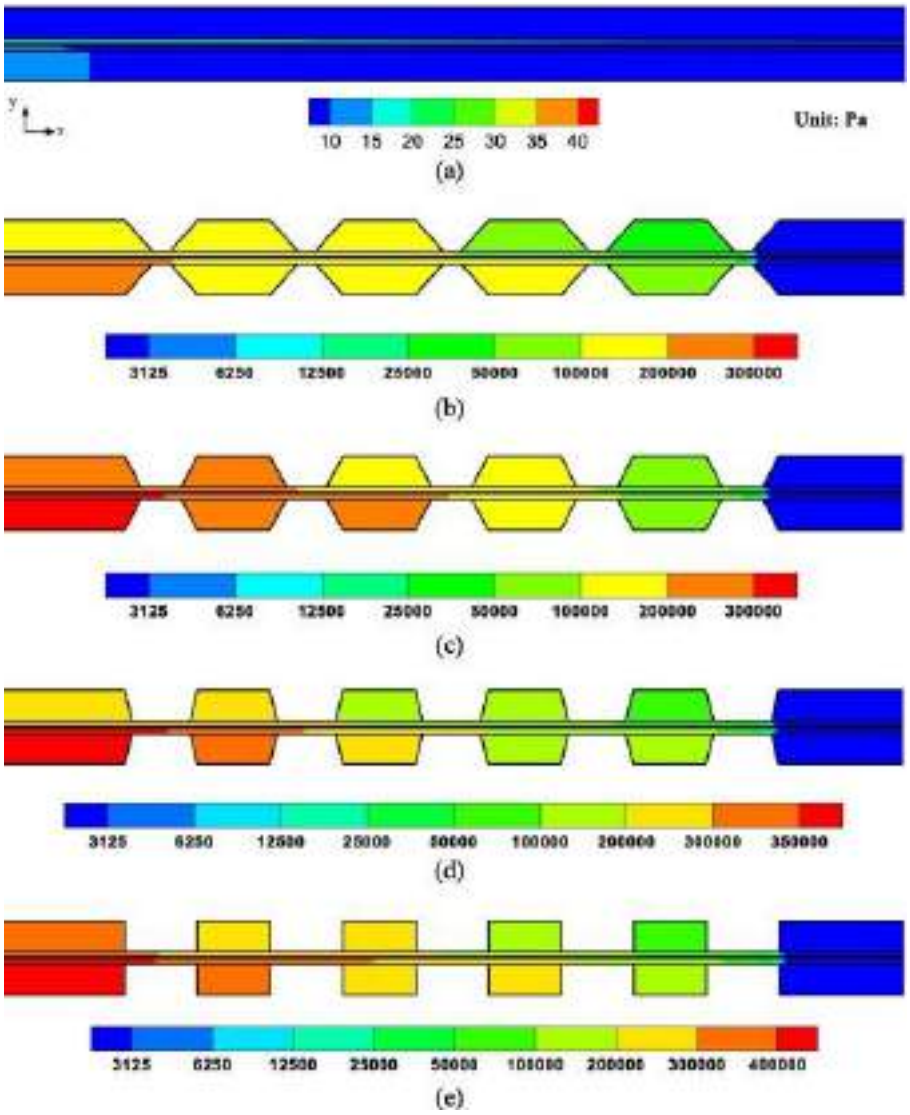

Figure 11 Pressure distribution along the channel with different types of baffles presented by (Perng and Wu, 2015)

(Li, Zhang and Shen, 2025) report the results of a comprehensive three-dimensional non-isothermal CFD study of high-temperature PEMFCs using rectangular baffles in the cathode channel: baffle height, number (positioning) and length were investigated.

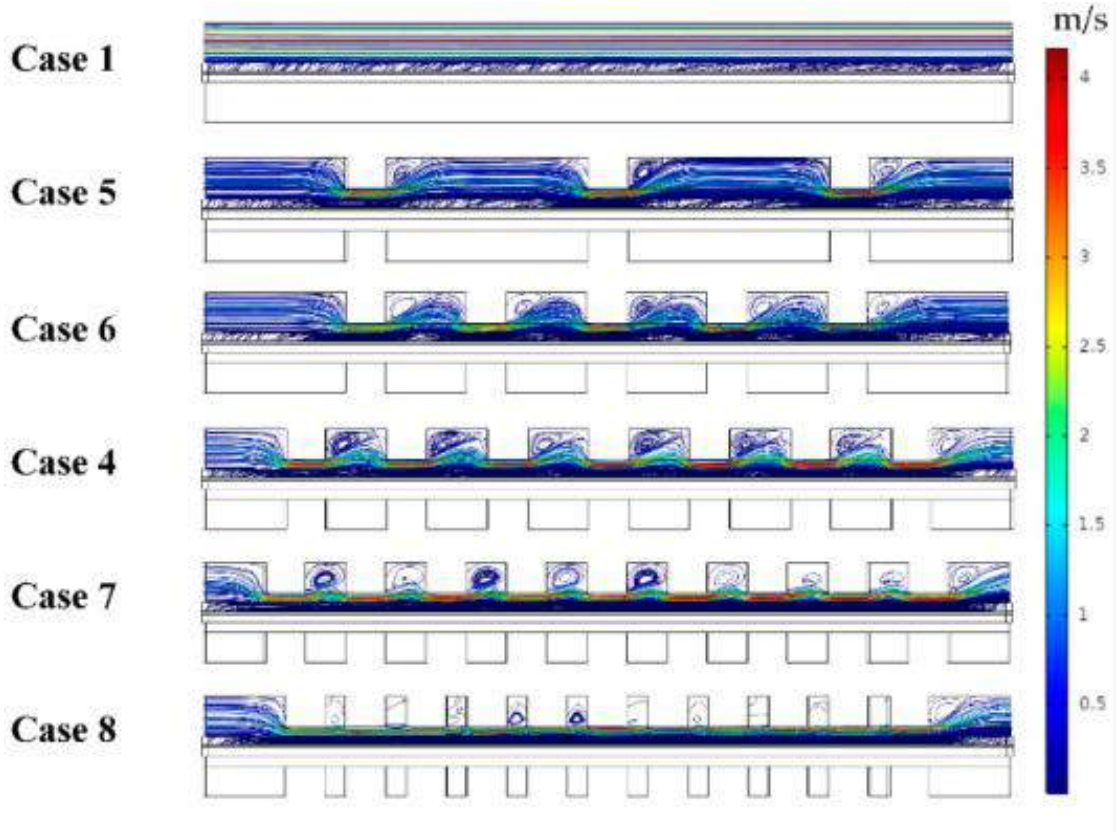

Figure 12 Velocity Profiles of Cathode Side in each case he changed height, length and number of baffles presented by (Li, Zhang and Shen, 2025)

At a cell voltage of 0.4 V, nine rectangular baffles, 0.75 mm high, raised current density from 1.390 A/cm² to 1.524 A/cm²: a 9.6% enhancement. Contour maps of static pressure revealed higher pressure immediately upstream and lower pressure immediately downstream of baffles, and the pressure difference increased as baffle height increased. The GDL velocity field correspondingly exhibited enhanced through-plane flux in the vicinity of baffles, and an associated increase of the oxygen concentration at the catalyst layer surface. They demonstrated that compared to the number and length of baffles, the baffle height was the most significant factor influencing the velocity distribution within the GDL and the oxygen transport in the cathode, giving a clear quantitative rationale for their study of baffle height. Others have also investigated the pressure drop behaviour of baffled cathode channels.

(Ghasabehi et al., 2024) used three-dimensional CFD combined with artificial intelligence-driven multi-objective optimisation for the cathode channels and reported that eight baffles with a taper ratio of 2.23 resulting in 67% improvement in power density. They analysed the static pressure contours in the channel and found pressure spikes at the

baffles which induced a localised transport event in the GDL. They found that while more baffles increased the multiplications of the GDL transport events driven by pressure peaks, an excessive baffle number increased the total pressure drop, ultimately penalising net power generation.

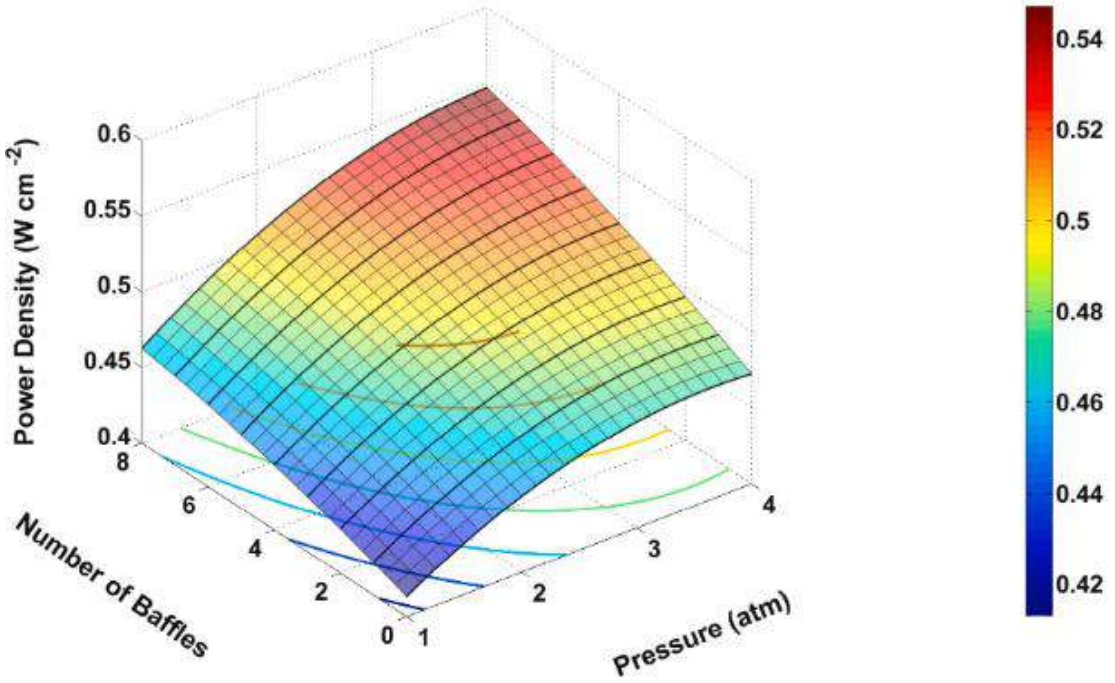

Figure 13 Effect of Number of Baffles and Pressure on Power Density presented by (Ghasabehi et al., 2024)

(Wu and Ku, 2011) employed the Taguchi method in a three-dimensional PEMFC model to optimise the design factors of rectangular cylinders placed transversely in the flow channel, and found that the optimal rectangular baffle configuration provided the highest oxygen supply to the cathode catalyst layer with a moderate pressure drop, also confirming the effectiveness of rectangular baffles to enhance transport in the cathode.

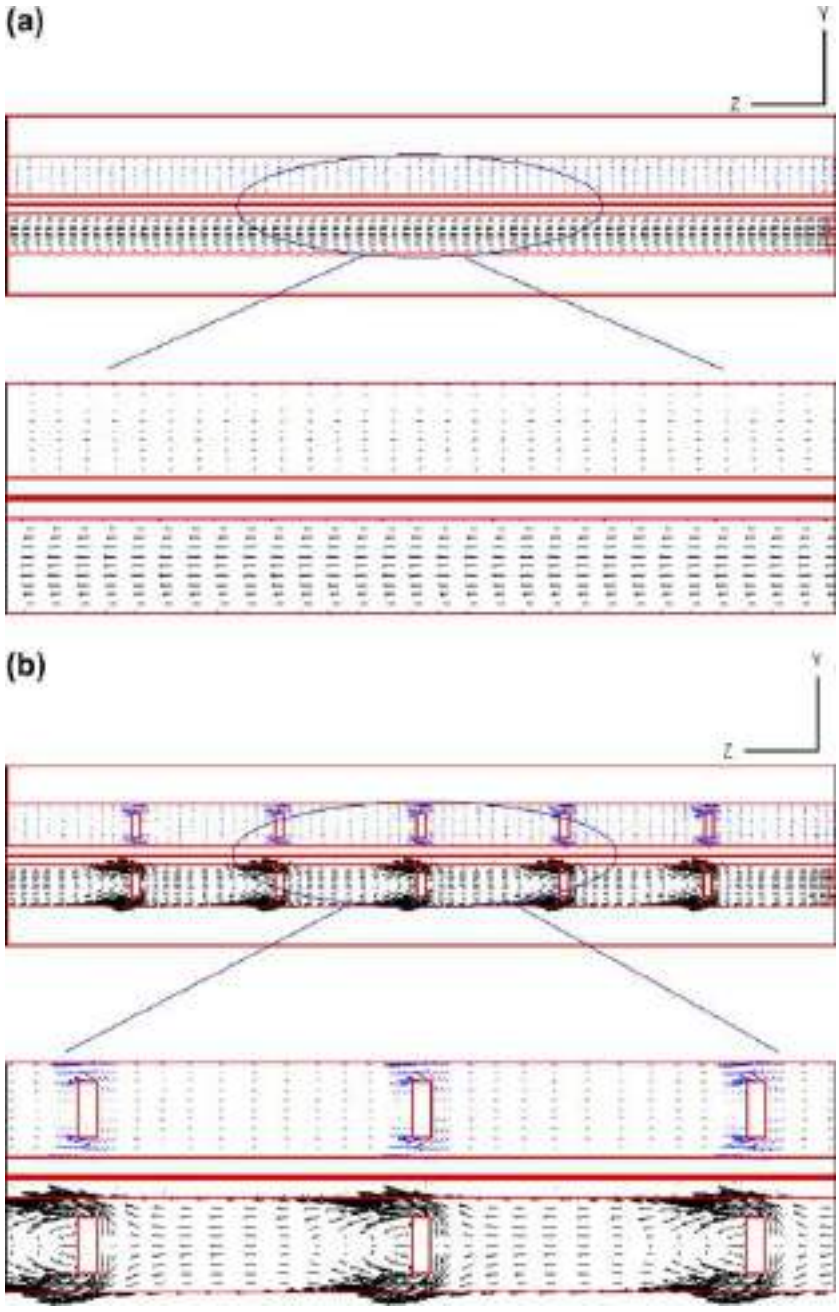

Figure 14 Velocity Vectors presented by (Wu and Ku, 2011) (a) Straight Channel (b) With Baffles

Author(s) & Year	Channel / Model Type	Tool / Method	Key Parameter(s)	Key Finding / Result
Hashemi & Ghazikhani (2012)	Straight & serpentine — single phase	3D non-isothermal CFD	O_2/H_2 distribution, current density, temperature	Straight channel showed progressive O_2 depletion from inlet to outlet, non-uniform current density. Serpentine yielded better uniformity. Both validated against experimental polarisation curves.
Sivertsen & Djilali (2005)	Straight channel — single phase, 3D	CFD, single computational domain	Velocity, species concentration, current density	Single-phase model validated against experimental polarisation data. 3D flow structure in cathode air channel directly impacted oxygen concentration reaching the catalyst. Model accurately reproduced performance over moderate current density range.
Berning & Djilali (2003)	Straight channel — single phase, 3D non-isothermal	CFD (full 3D, FLUENT)	Current density, pressure drop, velocity, temperature	Comprehensive single-phase non-isothermal straight-channel model quantified coupled transport phenomena. Local activation overpotential prediction improved current density distribution accuracy. Established governing equation framework adopted widely by later studies.
Mohammedi et al. (2020)	Straight channel — 6 cross-section shapes	3D CFD (ANSYS Fluent)	Channel geometry, velocity, power density	Circular cross-section gave highest power density, rectangular cross-section best balance of performance and manufacturability. Velocity at sub-rib GDL surface directly governed local O_2 supply to catalyst layer.
Yin et al. (2018)	Straight + baffle plates (cathode & anode)	3D CFD (FLUENT) with UDFs	Baffle number, position, O_2 concentration	Baffle plates raised local gas velocity; O_2 concentration in GDL increased; concentration overpotential reduced; liquid water removal improved. Baffle position significantly affected spatial O_2 distribution.
Perng & Wu (2015)	Straight + trapezoidal baffles (cathode)	3D non-isothermal CFD	Baffle height, angle, through-plane velocity, net power	60° angle at 1.125 mm height → ~90% net power improvement vs. unbaffled channel. Through-plane velocity at GDL increased non-linearly with height; beyond optimal height, pressure drop penalty dominated.
Chen et al. (2024)	Serpentine + rectangular, trapezoidal, semicircular baffles (cathode)	3D CFD (FLUENT)	Baffle shape, O_2 mass fraction at CL–GDL interface	Rectangular baffles → highest O_2 mass fraction at cathode CL–GDL (0.196 vs. 0.193 trapezoidal, 0.188 semicircular, 0.184 no baffle). Most uniform spatial O_2 distribution. Attributed to sharper flow deflection and larger effective convective area.
Xu et al. (2025)	Straight + rectangular baffles (cathode)	3D non-isothermal CFD	Baffle height, number, length; current density, pressure contours	9 rectangular baffles at 0.75 mm height increased current density from 1.390 to 1.524 A/cm² at 0.4 V (+9.6%). Distinct high-pressure upstream / low-pressure downstream zones confirmed baffle-driven forced convection into GDL.
Ghasabehi et al. (2024)	Parallel + baffles + taper (cathode)	3D CFD + AI optimisation	Baffle number, taper ratio, output power density	Optimal: 8 baffles + taper ratio 2.23 → 67% increase in power density; net power 0.93 W cm^{-2}. Baffle–taper interaction amplified GDL velocity and O_2 uniformity along channel length.
Wang et al. (2020)	Parallel vs. staggered trapezoid baffles (cathode)	3D CFD + experimental	Baffle arrangement, crossflow, O_2 distribution	Staggered arrangement generated inter-channel crossflow; more uniform O_2 distribution and superior liquid water removal. Validated experimentally with good agreement on polarisation curves.

Table 1 Summary of Literature Review

2.3 Research Gap

The review of the literature in the previous sections provides a consistent body of work in three areas: the basic description of the performance of straight-channel PEMFCs through single-phase CFD modelling; the reported mass transport limitations of the straight-channel geometry at high current density operation; and the demonstrated effectiveness of baffles, and especially rectangular baffles, in the cathode flow channel for increasing forced convection, through-plane GDL velocity, and reactant gas (oxygen) transport. Up to 90% improvement in net power has been documented with baffles (depending on baffle

geometry and operating conditions), and rectangular baffles have been demonstrated to be the most effective baffle shape for cathode-side reactant transport due to maximisation in the oxygen mass fraction and optimal distribution at the CL-GDL interface.

But there are some specific areas where additional understanding would be beneficial. First, although the baffle height has been noted as the most critical geometric feature, the isolated effect of baffle height variation on the static pressure distribution, magnitude of the velocity vectors, and reactant transport within the cathode GDL, catalyst layer, and baffle zones - within a single-phase modelling approach - have not been systematically reported at multiple baffle heights for a straight-channel geometry, using a rectangular baffle shape. The works that have considered baffle height variations usually employ a trapezoidal or other non-rectangular geometry, or double baffling of the anode and cathode to render individual isolation of cathode-specific, baffle height-dependent transport response for a rectangular geometry unviable.

Second, although single-phase modelling has been extensively used to investigate straight-channel PEMFCs, its extension to systematically variable rectangular baffle height in the cathode-only baffled straight channel - with detailed spatial reporting (in terms of baffle height) of static pressure and velocity distributions in the GDL, catalyst layer, and baffle regions - has not been previously reported. While the single-phase assumption is physically reasonable for investigating the basic physical convective transport phenomena due to the baffles at moderate operating conditions, its use facilitates direct, computationally efficient parametric studies, avoiding two-phase water transport modelling complexity. A dedicated three-dimensional single-phase computational fluid dynamics (CFD) study in ANSYS Fluent that explicitly retains only the rectangular baffle height as a variable in the cathode-only baffled straight channel with detailed static pressure and velocity reporting across the GDL, catalyst layer and baffle domains, would effectively fill this gap and provide quantitative insights into the physically relevant, practical design considerations for selecting the height of a rectangular baffle in the cathode side of a PEM fuel cell.

Chapter 3: Methodology

The proton exchange membrane fuel cells (PEMFCs) modelling is a complex of interplay between electrochemical reactions, fluid flow, and multi-species transportation processes at various length and time scales. Because of this complexity, a computational fluid dynamics (CFD)-based framework is embraced to come up with a holistic and physically sound numerical model. The general approach to the research is systematic and comprises of:

- Physicochemical model development,
- Application of numerical solution algorithms,
- Characterisation of materials and use of boundary conditions, and
- Model validation and performance evaluation.

The overall aim of this research is to construct a three-dimensional, steady-state, single-phase PEM fuel cell model that could analyse the reactant transport constraints and enhance the cell efficiency, especially in the case of a high current density (>7000 A/m^2). It is a porous media, electrochemical kinetics, and species transport model, which is solved by a CFD solver (ANSYS Fluent 2025 R2) with personalised C++ user-defined functions (UDFs).

3.1 Modelling of PEM Fuel Cells

PEM fuel cell computational modelling is an effective instrument in the study of internal processes which are hard to measure in experiments. The CFD modelling in the study is used to obtain the following:

- Examine mass transport processes using porous layers (GDL and CL) which is essential in determining the transport constraints at high current densities.
- Investigate reactant distribution and its effect on performance.
- Predict current density distribution at the catalyst layer–membrane interface.
- Consider design changes, such as flow channel arrangements and baffle use, to improve the reactant delivery.
- Study about the effects of porosity and permeability on transport behaviour.

Offer a model on how to enhance the efficiency and homogeneity of electrochemical reactions in the fuel cell. Though CFD models can be used to carry out transient multiphase simulations, the current work is based on a single-phase steady-state model, and the water

is in the vapour state. This simplification enables the investigation of the reactant transport limitations in detail which is the main aim of this study.

3.2 Model Development

A three-dimensional single-cell PEM fuel cell is considered as the computational domain. The model is the fundamental layers that cause transport and electrochemical reactions, such as:

- Anode Flow Channel
- Anode Gas Diffusion Layer (GDL)
- Anode Catalyst Layer (CL)
- PEM (Proton Exchange Membrane)
- Cathode Catalyst Layer (CL)
- Cathode Gas Diffusion Layer (GDL)
- Cathode Flow Channel

The flow channels have the role of transporting reactants (hydrogen at the anode and oxygen/air at the cathode) and products away. The gas diffusion layers (GDLs) serve as porous media which facilitate uniform distribution of reactants and transport to the catalyst layers. The electrochemical reactions take place in the catalyst layers (CLs). The membrane permits the movement of protons but not electrons and reactant gases.

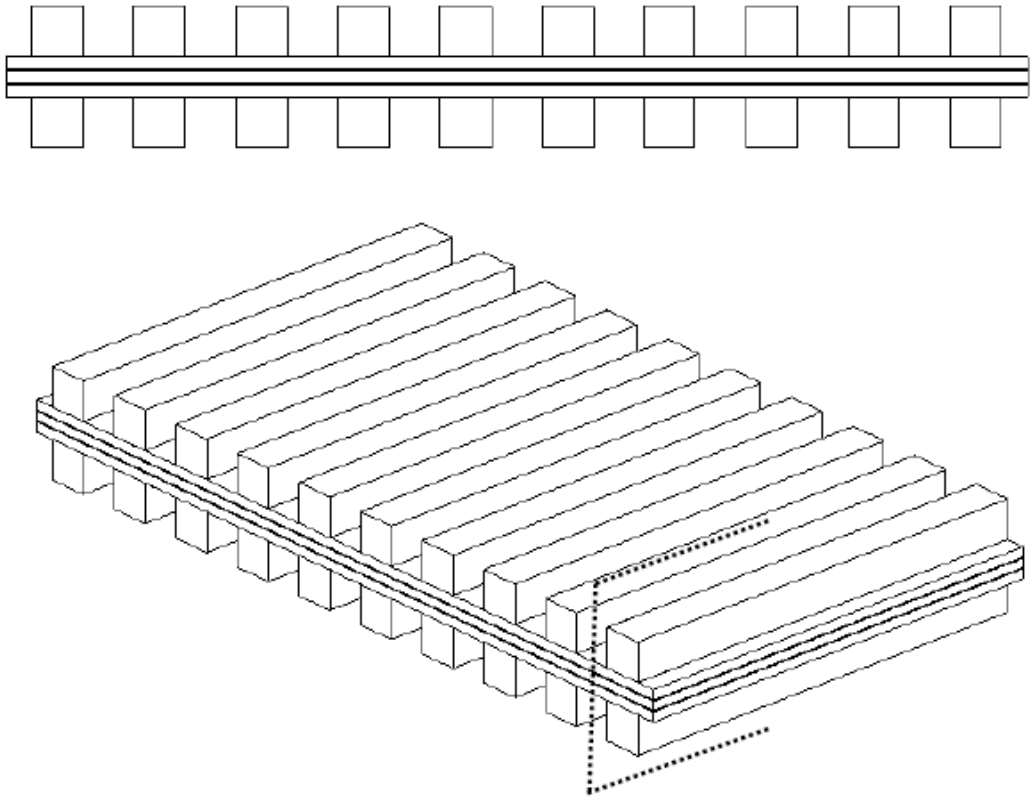

Figure 15 3D Model of Fuel Cells (Islam, 2012)

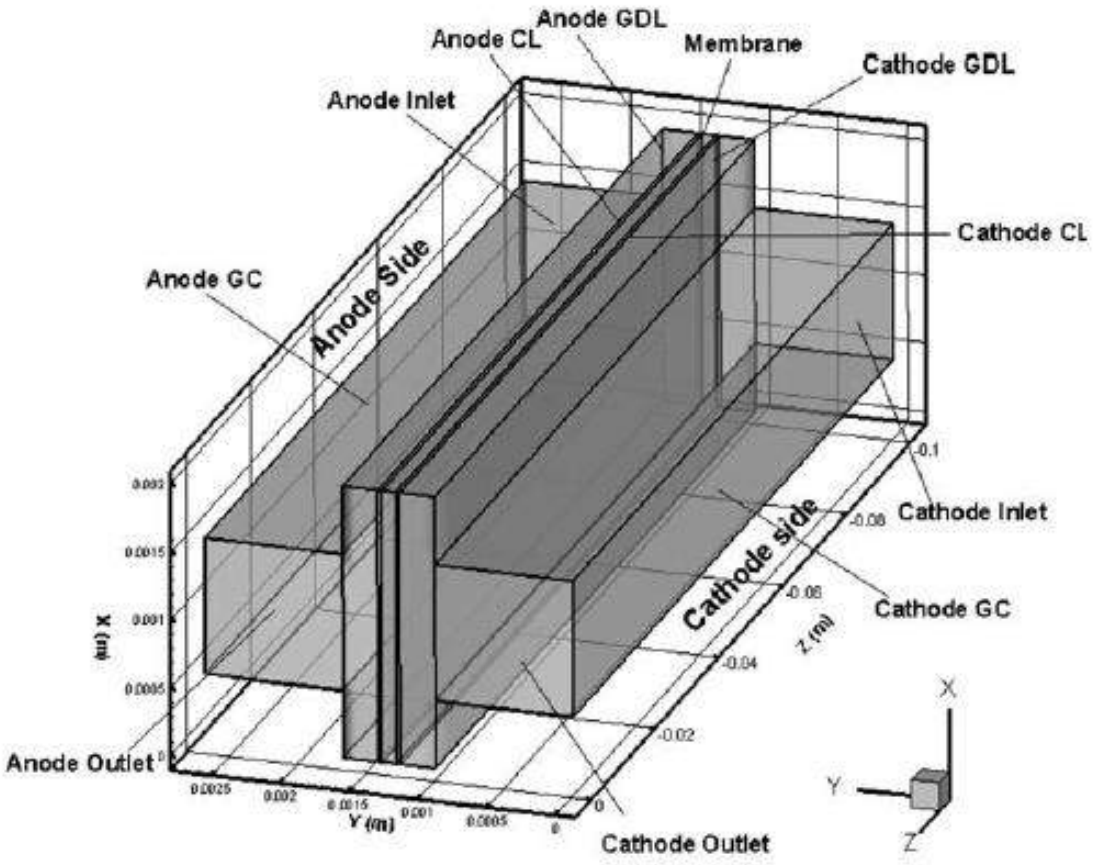

Figure 16 Schematic Diagram of PEM Fuel Cell Model (Hossain, Islam and Pollard, 2012)

The model is set to enable: to support the project objectives.

- Modification of flow-field geometry (including baffles),
- Variation of porous properties (porosity and permeability), and
- Adjustment of operating conditions such as humidity.

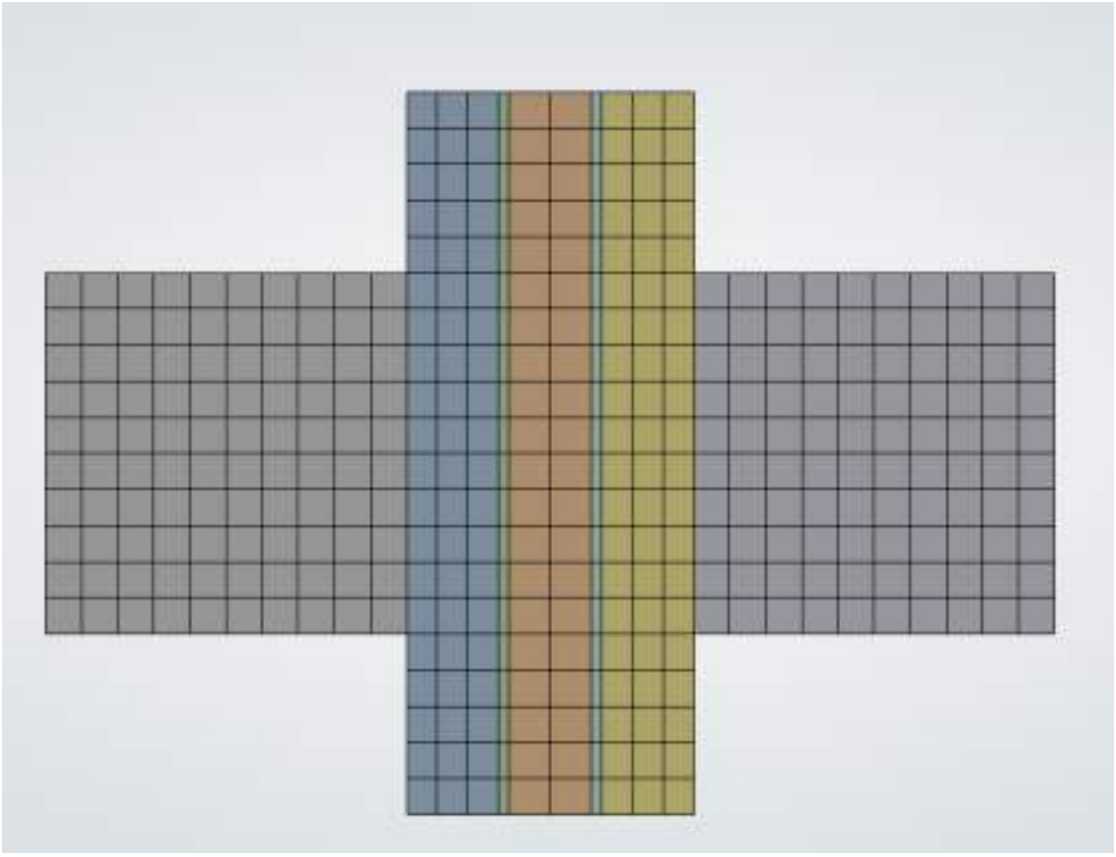

Figure 17 Numerical Grid Front

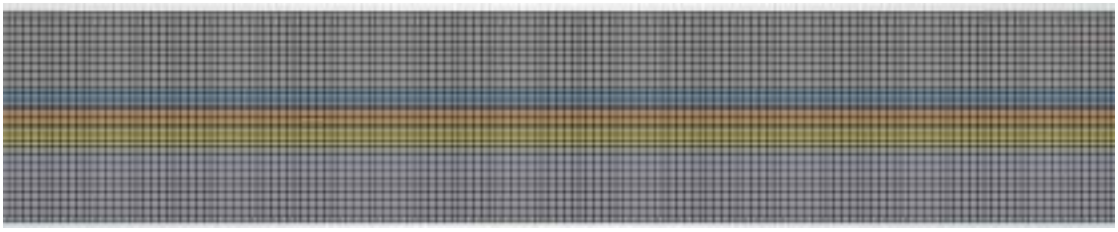

Figure 18 Numerical Grid along the Channel Length

3.3 Assumptions

To make the computations physically accurate and computationally feasible, the following assumptions are made:

- The fuel cell is used in steady state.
- It is assumed that the system is isothermal and does not have temperature gradients.
- Gas mixtures are ideal gases.
- The channels flow is laminar (Reynolds number < 100).
- The membrane is non-permeable to gases of reactants.

- It is based on a single-phase model; all the produced water is assumed to be in vapour phase, and the formation of liquid water is not considered.
- The electrochemical reactions take place exclusively in the catalyst layers.
- At the catalyst layer–membrane interface, zero velocity gradient and zero species gradient conditions are applied.

Single phase assumption is an intentional modelling decision to decouple the transport constraints of reactants but ignores the effect of flooding which can be important at extremely high current densities.

3.4 Governing Equations

The governing equations used in the steady-state model of a PEM fuel cell currently include the mass, momentum and species transport equations. The chemical reactions and mass transport processes in the membrane were accounted for via source terms at the anode and cathode catalyst layer boundaries. The energy equation was not considered in the governing equations due to the assumption of isothermal condition in the entire computational domain.

The mass conservation equation (continuity equation):

$$\nabla.(\rho\,\vec{u}) = S_m$$

where,

$\rho = Fluid\ Density$

$\vec{u} = velocity\ vector$

$S_m = Source\ Term$

The momentum equation:

$$\nabla.(\rho\vec{u}\vec{u}) = -\nabla P + \nabla.(\mu\nabla.\vec{u}) + S_u$$

where,

$P = Pressure$

$S_u = Source\ Term$

For the porous parts of the computational domain (the gas diffusion layers and catalyst layers), the effect of the resistance to the gas flow through the porous medium was modelled by adding a Darcy's law source term to the momentum equations. This was the viscous drag force of the porous structure on the gas flow and is given by

$$S_u = -\frac{u\vec{u}}{K}$$

The species conservation equation:

$$\nabla.\left(\rho\vec{u}\overrightarrow{X_k}\right) = \nabla.\left(D_k^{eff}\rho\nabla\overrightarrow{X_k}\right) + S_k$$

where,

$k = represents\ to\ different\ species$

$X_k = Mass\ Fraction\ of\ species(k)$

$D_k^{eff} = Effective\ Diffusion\ Coefficient$

The species conservation equations solved for hydrogen and water vapours in anode side:

$$\nabla.\left(\rho\vec{u}\overrightarrow{X_{H_2}}\right) = \nabla.\left(D_{H_2}^{eff}\rho\nabla\overrightarrow{X_{H_2}}\right) + S_{H_2}$$

$$\nabla.\left(\rho\vec{u}\overrightarrow{X_{wv_a}}\right) = \nabla.\left(D_{wv_a}^{eff}\rho\nabla\overrightarrow{X_{wv_a}}\right) + S_{aw}$$

The species conservation equations solved for oxygen and water vapours in cathode side:

$$\nabla.\left(\rho\vec{u}\overrightarrow{X_{O_2}}\right) = \nabla.\left(D_{O_2}^{eff}\rho\nabla\overrightarrow{X_{O_2}}\right) + S_{O_2}$$

$$\nabla.\left(\rho\vec{u}\overrightarrow{X_{wv_c}}\right) = \nabla.\left(D_{wv_c}^{eff}\rho\nabla\overrightarrow{X_{wv_c}}\right) + S_{cw}$$

The diffusivity (diffusion coefficient) in the gas channel was expressed as

$$D_k = D_{k,ref}\left(\frac{T}{T_{ref}}\right)^{3/2}\left(\frac{P_{ref}}{P}\right)$$

Where $D_{k,ref}$ is the reference value at T_{ref} and P_{ref}.

The effective diffusivity is described by the (Islam, 2012):

$$D_k^{eff} = f(\varepsilon)D_k$$

The function expressed by Bruggeman correlation:

$$f(\varepsilon) = \varepsilon^{1.5}$$

Percolation theory-based diffusion model for random fibrous medium suggested by (Tomadakis and Sotirchos, 1993 references need to be added in bib)

$$f(\varepsilon) = \varepsilon\left(\frac{\varepsilon - \varepsilon_p}{1 - \varepsilon_p}\right)^{\alpha}$$

$where, \varepsilon_p(Percolation\ Threshold) = 0.11$

$\alpha\ (emperical\ constant) = 0.521(in - plane)$

$\alpha = 0.785(cross - plane)$

The above values were taken from (Islam, 2012).

The source terms (S_k) in the species conservation equations were set to zero throughout the entire computational domain, except at the catalyst layers, where the electrochemical reactions took place. The species source terms in the anode and cathode catalyst layers were given by:

- The hydrogen consumption due to the electrochemical oxidation reaction in the anode catalyst layer:

$$S_{H_2} = -\frac{IA}{2F} M_{H_2}$$

- The oxygen consumption due to the electrochemical reduction reaction in the cathode catalyst layer:

$$S_{O_2} = -\frac{IA}{4F} M_{O_2}$$

- The water generation from the oxygen reduction reaction and water flux due to electrochemical and transport effects in the cathode catalyst layer were described as:

$$S_{cw} = -\frac{[1 + 2\alpha]IA}{2F} M_{H_2O}$$

- Flux of water due to electrochemical effects at the anode CL:

$$S_{aw} = -\frac{\alpha IA}{F} M_{H_2O}$$

PEM fuel cell Zones	S_m	S_u	S_k
Gas channels	0	0	0
Gas diffusion layers	0	$S_u = -\frac{\mu \vec{u}}{K}$	0
Catalyst layers	0	$S_u = -\frac{\mu \vec{u}}{K}$	Cathode side: $S_{O_2} = -\frac{IA}{4F} M_{O_2}$ $S_{cw} = \frac{[1+2\alpha]IA}{2F} M_{H_2O}$ Anode side: $S_{H_2} = -\frac{IA}{2F} M_{H_2}$ $S_{aw} = -\frac{\alpha IA}{F} M_{H_2O}$
Membrane	0	0	0

Figure 19 Source Terms for Fuel Cell Model (Islam, 2012)

Auxiliary Equations

(Lum and McGuirk 2005) defined the net water transfer coefficient as the water transport across the membrane, which was due to the combined effects of the electro-osmotic drag (anode to cathode) and the back diffusion (cathode to anode).

$$\alpha = n_d - \frac{FD_{H_2O}(C_{H_2O_c} - C_{H_2O_a})}{It_m}$$

where,

$D_{H_2O} = Water\ Diffusion\ Coefficient$

$C_{H_2O_c} = Molar\ Concentration\ of\ Water\ at\ Cathode$

$C_{H_2O_a} = Molar\ Concentration\ of\ Water\ at\ Anode$

$I = Average\ Current\ Density$

$t_m = Membrane\ Thickness$

$F = Faraday's\ Constant$

The electro-osmotic drag coefficient is the number of water molecules moved from the anode to the cathode side of the membrane per migrating proton, and was defined as (Lum and McGuirk, 2005)

$$n_d = 0.0049 + 2.02a_a - 4.53a_a^2 + 4.09a_a^3;\ a_a \leq 1$$

$$n_d = 1.59 + 0.159(a_a - 1);\ a_a > 1$$

Electro-osmotic drag:

$$a_k = \frac{X_{H_2O,K}P}{P_{H_2O,K}^{sat}}$$

Water Diffusion Coefficient in terms of electro-osmotic drag coefficient and the cell temperature:

$$D_{H_2O} = 5.5e^{-11}n_d exp[2416(\frac{1}{303} - \frac{1}{T})]$$

Water vapour saturation pressure:

$$\begin{aligned} P_{H_2O,K}^{sat} = [&0.000644367 + 0.000213948(T - 273.0) + 3.4329e^{-5}(T - 273.0)^2 \\ &- 2.70381e^{-7}(T - 273.0)^3 + 8.7769e^{-9}(T - 273.0)^4 \\ &- 3.14035e^{-13}(T - 273.0)^5 + 3.82148e^{-14}(T - 273.0)^6]1.013e^5 \end{aligned}$$

Polarization Characteristics

When the cell generates electrical current, the cell potential reduces below the open circuit potential (theoretically available potential) by irreversible losses, known as polarisation or overpotential losses. The cell potential was then given by (Hossain, Islam and Pollard, 2012):

$$V_{cell} = E - \eta_{act} - \eta_{ohm} - \eta_{conc}$$

where,

$E = Equilibrium\ Thermodynamic\ Potential$

$\eta_{act} = Activation\ Overpotential$

$\eta_{ohm} = Ohmic\ Overpotential$

$\eta_{conc} = Concentration\ Overpotential$

where E can be calculated by using Nernst equation (Min, 2009):

$$E = 1.23 - 0.9 \times 10^{-3}(T - 298) + 2.3\frac{RT}{4F}\log(p_h^2 p_o)$$

- Activation Overpotential (η_{act}):

  Butler-Volmer equation (Hossain, Islam and Pollard, 2012):

$$i_a = 2i_{a,ref}(\frac{C_h}{C_{h,ref}})^{1/2}\sinh(\frac{\alpha_a n_a F \eta_a}{RT})$$

$$i_c = 2i_{c,ref}(\frac{C_o}{C_{o,ref}})^{1/2}\sinh(\frac{\alpha_c n_c F \eta_c}{RT})$$

  where (Hossain, Islam and Pollard, 2012)),

  $i_{c,ref} = current\ exchange\ density\ at\ cathode$

  $i_{a,ref} = current\ exchange\ density\ at\ anode$

  $n = Electron\ Number\ of\ Reaction$

  $\alpha = Transfer\ Coefficient$

- Ohmic Overpotential (η_{ohm}):

  The overpotential which occurs due to resistance to electron and ion transfer is termed as ohmic overpotential and can be expressed as (Hossain, Islam and Pollard, 2012):

$$\eta_{ohm} = \eta_{ohm}^{el} + \eta_{ohm}^{pro} = 1(R^{el} + R^{pro})$$

  where,

  $R^{el} = Resistance\ to\ Electron\ Transfer$

  $R^{pro} = Resistance\ to\ Proton\ Transfer$

$$R^{pro} = \frac{t_m}{k_m}$$

  where,

  $t_m = Height\ of\ the\ Membrane$

  $k_m = Phase\ conductivity\ of\ the\ Membrane$

  The membrane phase conductivity expressed as (Hossain, Islam and Pollard, 2012):

$$k_m = 100(0.00514\left(\frac{M_{m,dry}}{\rho_{m,dry}}\right)C_{H_2O_a} - 0.00326) \times \exp\left[1268(\frac{1}{303} - \frac{1}{T})\right]$$

- Concentration Overpotential (η_{conc}):

$$\eta_{conc} = -\frac{RT}{nF}\ln\left(1 - \frac{1}{I_L}\right)$$

where,

$I_L = Limiting\ Current$

$$I_L = \frac{nFD_hC_{k,o}}{H_d}$$

3.5 Numerical Implementation

ANSYS Fluent 2025 R2 is used to solve the governing equations, with further physics added as C++ User Defined Functions (UDFs). These UDFs are used to:

- Define terms of source of electrochemical reactions,
- Adopt consumption and generation rates of species,
- Use effective transport properties in porous media, and
- Couple electrochemical reactions with transport equations.

The numerical approximation uses a steady-state solver, and discretisation schemes are used to achieve accuracy and stability. When residuals become below acceptable limits and when key parameters (current density, species concentration) level off then convergence is attained. The UDF code was taken from (Islam, 2012).

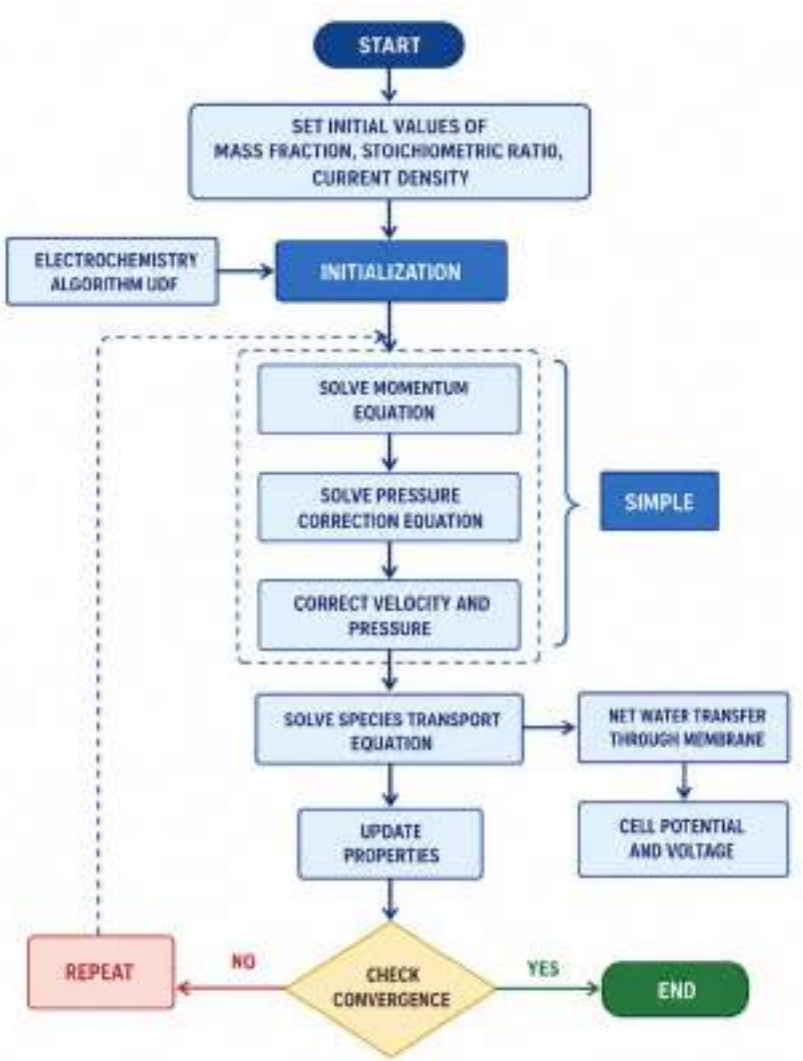

Figure 20 Numerical Process Flow Chart

3.6 Boundary Conditions

Appropriate boundary conditions were applied to accurately represent operating conditions:

- Anode inlet: hydrogen fed with defined velocity, pressure, temperature and humidity.
- Cathode inlet: oxygen/air fed by specific operating conditions.
- Outlets: pressure outlet conditions.
- Walls: no-slip boundary condition.
- Electrical boundaries: applied voltage/current at one electrode and fixed potential at the other.

The parametric study includes humidity conditions to determine the impact of humidity conditions on membrane hydration and performance. The graphical representation of boundary conditions are shown in figure 21.

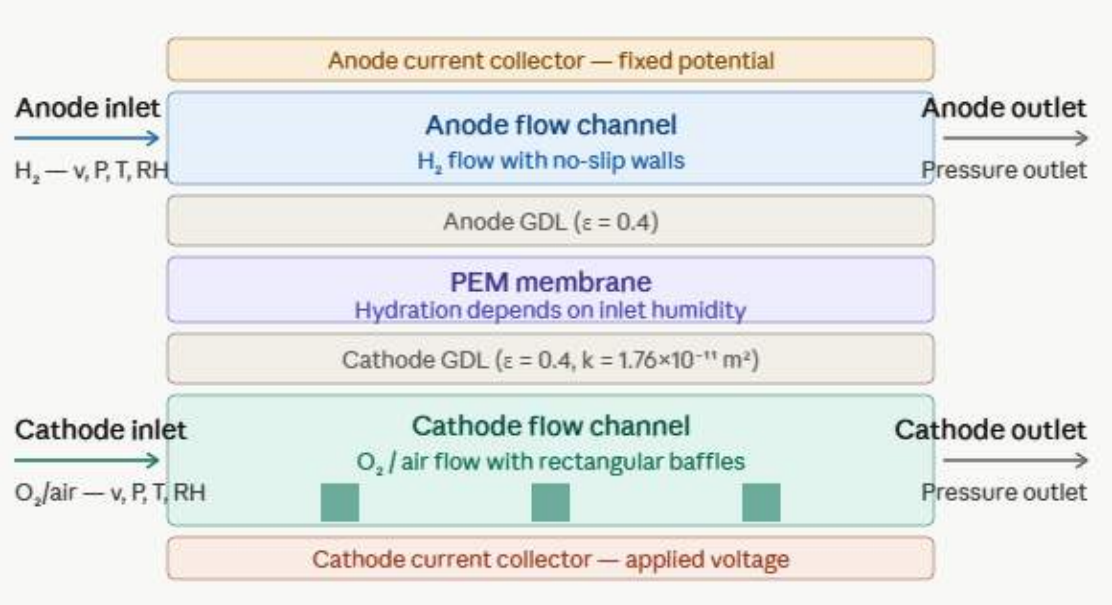

Figure 21 Graphical Representation of Boundary Conditions

Inlet Conditions and Values	
Very Low Humidity (VLH)	
Parameter	**Value**
ANODE	
Inlet Velocity	1.735 m/s
Mass Fraction of H_2	0.727
Mass Fraction of H_2O	0.273
CATHODE	
Inlet Velocity	7.33 m/s
Mass Fraction of O_2	0.225
Mass Fraction of N_2	0.751
Mass Fraction of H_2O	0.024
Low Humidity (LH)	
ANODE	
Inlet Velocity	1.83 m/s
Mass Fraction of H_2	0.635

Mass Fraction of H_2O	0.365
CATHODE	
Inlet Velocity	7.91 m/s
Mass Fraction of O_2	0.225
Mass Fraction of N_2	0.734
Mass Fraction of H_2O	0.046
High Humidity (HH)	
ANODE	
Inlet Velocity	2.21 m/s
Mass Fraction of H_2	0.406
Mass Fraction of H_2O	0.594
CATHODE	
Inlet Velocity	9.05 m/s
Mass Fraction of O_2	0.21
Mass Fraction of N_2	0.705
Mass Fraction of H_2O	0.085
Very High Humidity (VHH)	
ANODE	
Inlet Velocity	2.56 m/s
Mass Fraction of H_2	0.295
Mass Fraction of H_2O	0.705
CATHODE	
Inlet Velocity	12.9 m/s
Mass Fraction of O_2	0.187
Mass Fraction of N_2	0.61
Mass Fraction of H_2O	0.203

Table 2 Inlet Conditions and Values (Lum and McGuirk, 2005)

3.7 Modelling Parameters

	No.	PARAMETERS	SYMBOL & VALUE	REFERENCE(S)
GEOMETRICAL PARAMETERS	1	Gas Channel Length	$L = 100\ \text{mm}$	(Hossain, Islam and Pollard, 2012)
	2	Gas Channel Width	$W = 1\ \text{mm}$	(Hossain, Islam and Pollard, 2012) (Min, 2009)
	3	Gas Channel Height	$H_{ch} = 1\ \text{mm}$	(Hossain, Islam and Pollard, 2012) (Min, 2009)
	4	Diffusion Layer Height	$H_d = 0.254\ \text{mm}$	(Hossain, Islam and Pollard, 2012) (Min, 2009) (Liu et al., 2006)
	5	Catalyst Layer Height	$H_{cl} = 0.0287\ \text{mm}$	(Hossain, Islam and Pollard, 2012) (Min, 2009) (Liu et al., 2006)
	6	Land Area Width	$W_l = 1\ \text{mm}$	(Hossain, Islam and Pollard, 2012) (Min, 2009)
PHYSICAL PROPERTIES	7	Membrane Thickness	$t_m = 0.23\ \text{mm}$	(Hossain, Islam and Pollard, 2012)
	8	Permeability	$K = 1.76 \times 10^{-11}\ \text{m}^2$	(Hossain, Islam and Pollard, 2012) (Min, 2009) (Liu et al., 2006)
	9	Faraday Constant	$F = 96{,}485.309\ \text{C/mol}$	(Hossain, Islam and Pollard, 2012)
	10	GDL Porosity	$\epsilon_{GDL} = 0.4$	(Hossain, Islam and Pollard, 2012) (Liu et al., 2006)
	11	CL Porosity	$\epsilon_{CL} = 0.4$	(Hossain, Islam and Pollard, 2012)
	12	Dry Mass of Membrane	$M_{m,dry} = 1.1\ \text{kg/mol}$	(Hossain, Islam and Pollard, 2012)
	13	Dry Density of Membrane	$\rho_{m,dry} = 2000\ \text{kg/m}^3$	(Hossain, Islam and Pollard, 2012)
	14	Fuel/air stoichiometric ratio	$\xi_a/\xi_c = 5/5$	(Hossain, Islam and Pollard, 2012)
OPERATING CONDITIONS	15	Operating Pressure	$P = 101{,}325\ \text{Pa}$	(Hossain, Islam and Pollard, 2012)
	16	Operating Temperature	$T = 323\ \text{K}$	(Hossain, Islam and Pollard, 2012)
	17	Electron Number of Anode Reaction	$n_a = 4$	(Hossain, Islam and Pollard, 2012)
	18	Electron Number of Cathode Reaction	$n_c = 2$	(Hossain, Islam and Pollard, 2012)
	19	Relative Humidity of Inlet Fuel	$RH_a = 100\%$	(Hossain, Islam and Pollard, 2012)
	20	Relative Humidity of Inlet Air	$RH_c = 0\%$	(Hossain, Islam and Pollard, 2012)
	21	Oxygen Mass Fraction of Inlet Air	$\omega_{O_2} = 0.232$	(Hossain, Islam and Pollard, 2012)
ELECTROCHEMICAL PARAMETERS	22	Anode Exchange Current Density	$i_{a,ref} = 2.0 \times 10^5\ \text{A/m}^3$	(Hossain, Islam and Pollard, 2012) (Min, 2009)
	23	Cathode Exchange Current Density	$i_{c,ref} = 160\ \text{A/m}^3$	(Hossain, Islam and Pollard, 2012) (Min, 2009)
	24	Hydrogen Reference Concentration	$C_{h,ref} = 56.4\ \text{mol/m}^3$	(Hossain, Islam and Pollard, 2012) (Min, 2009)
	25	Oxygen Reference Concentration	$C_{o,ref} = 3.39\ \text{mol/m}^3$	(Hossain, Islam and Pollard, 2012) (Min, 2009)
TRANSPORT & KINETIC PARAMETERS	26	Hydrogen (H_2) diffusion coefficient at reference state	$D_{h,ref} = 0.915 \times 10^{-4}\ \text{m}^2/\text{s}$	(Hossain, Islam and Pollard, 2012) (Min, 2009)
	27	Oxygen (O_2) diffusion coefficient at reference state	$D_{o,ref} = 0.22 \times 10^{-4}\ \text{m}^2/\text{s}$	(Hossain, Islam and Pollard, 2012) (Min, 2009)
	28	Water Vapour diffusion coefficient at reference state	$D_{w,ref} = 0.256 \times 10^{-4}\ \text{m}^2/\text{s}$	(Hossain, Islam and Pollard, 2012) (Min, 2009)
	29	Anode Transfer Coefficient	$\alpha_a = 0.5$	(Hossain, Islam and Pollard, 2012) (Min, 2009)
	30	Cathode Transfer Coefficient	$\alpha_c = 0.5$	(Hossain, Islam and Pollard, 2012) (Min, 2009)

Table 3 Modelling Parameters of the Study

Chapter 4: Parametric Study

The influence of relative humidity on the voltage-current density curve of a straight-channel PEM fuel cell was investigated by a parametric study of a three-dimensional, single-phase, CFD model, using ANSYS Fluent. The four cases (very low humidity (VLH), low humidity (LH), high humidity (HH), and very high humidity (VHH) were based on the validated three-dimensional PEMFC model of (Lum and McGuirk 2005), who developed and solved a complete anode-cathode model using the finite volume method and validated it against global polarisation and local current density measurements using a segmented cell. The cathode inlet flow velocity increases from 7.33 m/s (VLH) to 12.9 m/s (VHH) and the anode inlet flow velocity from 1.735 m/s (VLH) to 2.56 m/s (VHH), with increasing water vapour mass fractions on both sides. The oxygen mass fraction on the cathode side drops from 0.225 at VLH to 0.187 at VHH correspondingly due to dilution by the extra water vapour.

4.1 Mesh Convergence Study

A grid independence study was also performed to check the convergence behaviour of the current single phase PEM fuel cell model. Grid independence analysis is crucial to make sure that none of the results are so strongly influenced by the mesh resolution that the numerical result becomes a rather fragile outcome. A good solution should be consistent and stable: that is, if the mesh is made finer the results of the solution should show little change.

In numerical modelling, the truncation error is the difference between the exact continuous equation and the version of the equation that has been discretised. This error may increase with the solution process and cause divergence and/or unreliable predictions if the numerical solution method is unstable. Hence the resulting truncation error should tend towards zero as the value of the mesh spacing tends towards zero, which means the numerical solution should converge to the value as the mesh spacing becomes smaller (Islam, 2012).

Three different mesh densities were tested in this study with element counts of approximately 122,300, 220,000 and 500,200 elements respectively. To make a direct comparison between the various cell performances predicted by the simulations, all the simulations are done under identical operating and boundary conditions. The obtained polarisation curves for the three cases of different mesh are shown in Figure 22.

The comparison revealed that the prediction of the cell voltage was almost the same for all three mesh densities even though the computational times were higher for the smaller meshes. This means that a further mesh refinement made no important difference to the numerical prediction of the polarisation behaviour. Hence it was believed that the 122,300 element mesh was an adequate model to be used to predict cell performance at varying current densities and further offer a reasonable cost savings for the computational cost.

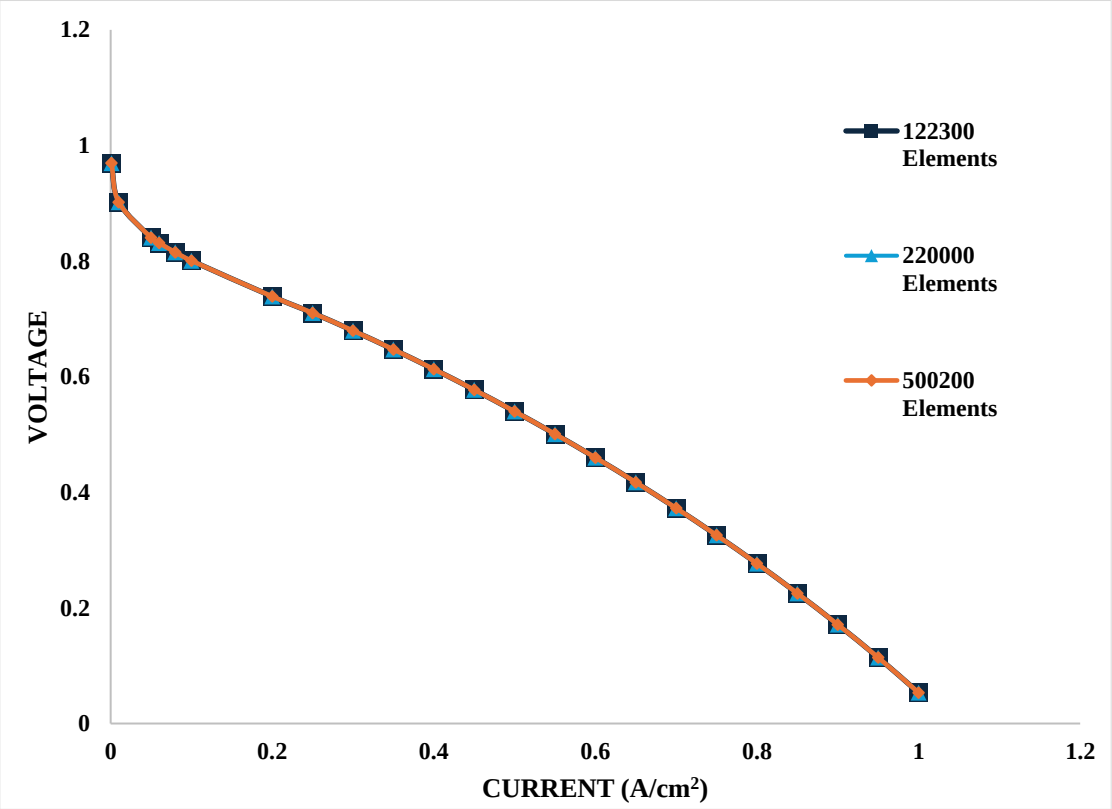

Figure 22 Mesh Independence Study

4.2 Polarisation Curves at different humidity conditions

The four different humidity cases all displayed the typical three-region polarisation curve of a PEM fuel cell. The four cases all started at the theoretical open-circuit voltage of around 1.0 V, with the VLH and LH cases starting at slightly higher voltages than the HH and VHH cases, due to the slightly higher oxygen partial pressure at the cathode at lower humidities where the effect of water vapour dilution was negligible. Polarisation curves are shown in Figure 23.

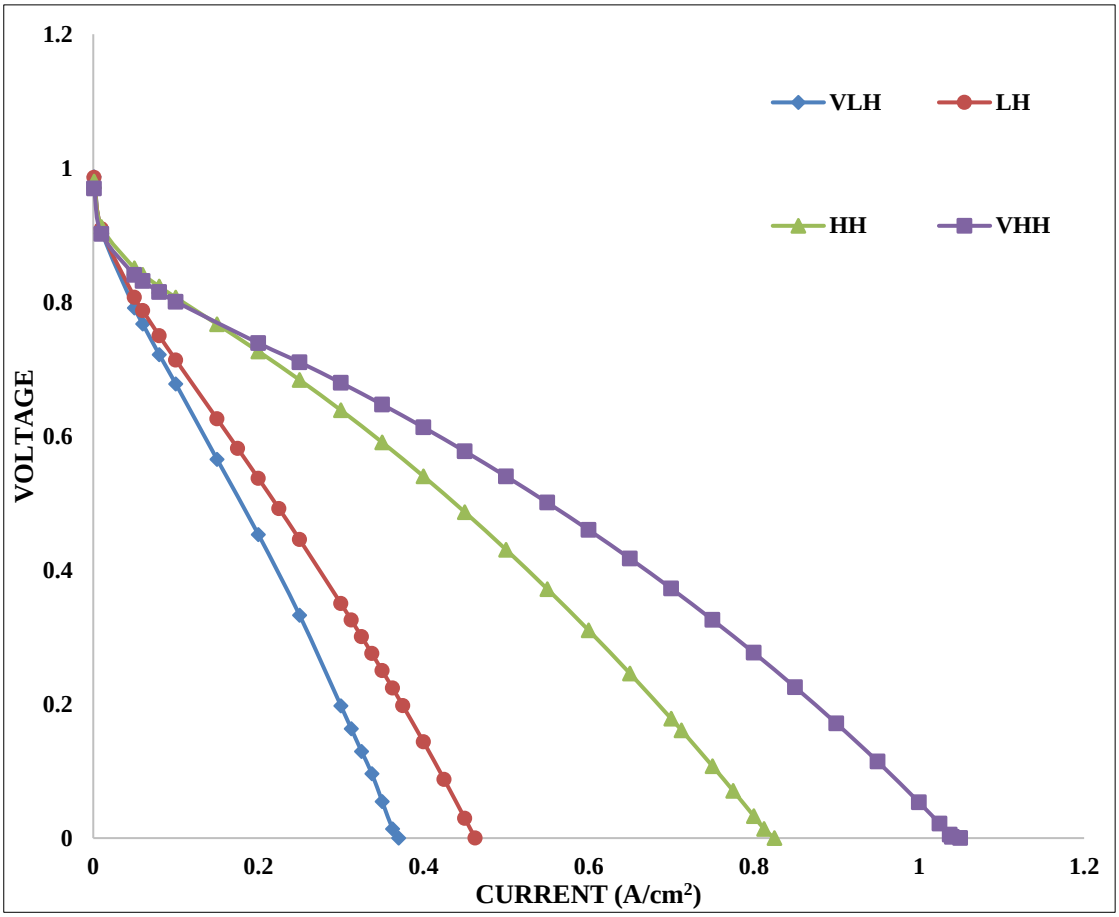

Figure 23 Voltage vs Current Densities Polarisation Curves for Straight Channel PEMFC

During the period of activation loss (0 to 0.03 A/cm²) the VLH and LH curves showed a more pronounced drop than the HH and VHH curves because of the reduced membrane ionic conductivity at lower water content. The membrane conductivity was related to the membrane hydration level (Lum and McGuirk, 2005) and the anode water mass fraction increased from 0.273 for the VLH case to 0.705 for the VHH case, which led to significantly different cell resistances at low current densities. The membrane conductivity model developed by (Springer, Zawodzinski and Gottesfeld,1991) and used by Islam (2012) confirmed that the membrane conductivity was approximately proportional to the membrane water content, which was in turn related to the local water activity on the anode side.

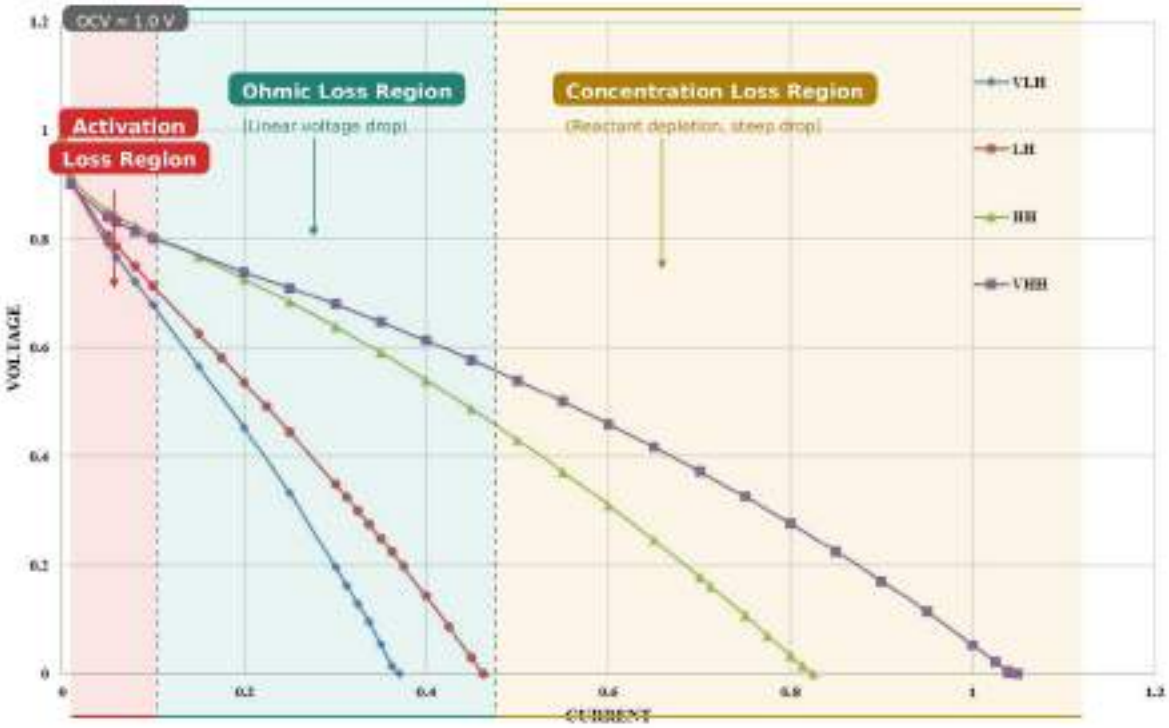

Figure 24 Losses Regions in Polarisation Curves

The greatest variations among the four cases were observed in the ohmic region as shown in figure 24. The VLH curve had the highest slope, with the VHH curve having the lowest slope, and thus the lowest resistance. At a reference current density of 0.2 A/cm², the voltage was about 0.45 V for the VLH case and 0.74 V for the VHH case - a 64% improvement. This agreed with the reports of (Hashemi, Rowshanzamir and Rezakazemi, 2012) that membrane hydration was the primary factor affecting the cell resistance in straight-channel PEMFCs. (Lee and Hwang, 2009) also noticed in a numerical study using parallel flow channels that the membrane ion conductivity was enhanced with increased cathode relative humidity, and that the highest membrane ion conductivity occurred at the channel inlet. More recently, (Soomro et al., 2023) also confirmed using 3D CFD modelling that fully humidified conditions produced about 10% higher current density than low humidity, thus confirming that humidity was a key performance metric.

In the concentration loss regime (figure 24), the limiting current density rose from around 0.35 A/cm² at VLH to 1.05 A/cm² at VHH - a 200% increase. This was despite a 17% decrease in the cathode side oxygen mass fraction (from 0.225 to 0.187) due to water vapour dilution, since the 76% increase in cathode inlet velocity (from 7.33 m/s to 12.9 m/s) improved convective transport of reactant gas to the catalyst layer. As pointed out by (Lum and McGuirk, 2005), the increased inlet velocity enabled more reactant gas to reach

the catalyst layer, while also assisting water removal. It was also found that the HH and VHH curves merged at low current density, implying that further increases in humidity would have little effect when the membrane was close to saturation. (Kulikovsky and Reshetenko, 2026) pointed out that water management was still important to optimise PEMFC performance, as excessive liquid water could significantly slow down oxygen diffusion - a scenario that was not captured by the current single-phase model, which inevitably over-estimated the VHH performance as noted by (Lum and McGuirk, 2005).

4.3 Current vs Power Curves at different humidity conditions

The power-current density of the straight-channel PEM fuel cell with four different inlet humidities were investigated to compare the peak power and the range of current densities in each case. The four curves all demonstrated the typical parabolic shape, starting from zero power at the open circuit voltage, reaching a maximum value and then dropping again to zero power at the limiting current density as shown in Figure 25.

The VLH case showed the lowest peak power of 0.09 at a current density of 0.2 A/cm². The LH case produced a slightly higher value of peak power of 0.11 at a current density of 0.25 A/cm². A significant increase in peak power was obtained for the HH case, where 0.2189 was reached at a current density of 0.45 A/cm². The highest peak power was observed in the VHH case at 0.2759 with a current density of 0.6 A/cm². Thus, the peak power under the VHH case was approximately three times that under the VLH case, and was a 211% improvement achieved by increasing the humidification of the inlets.

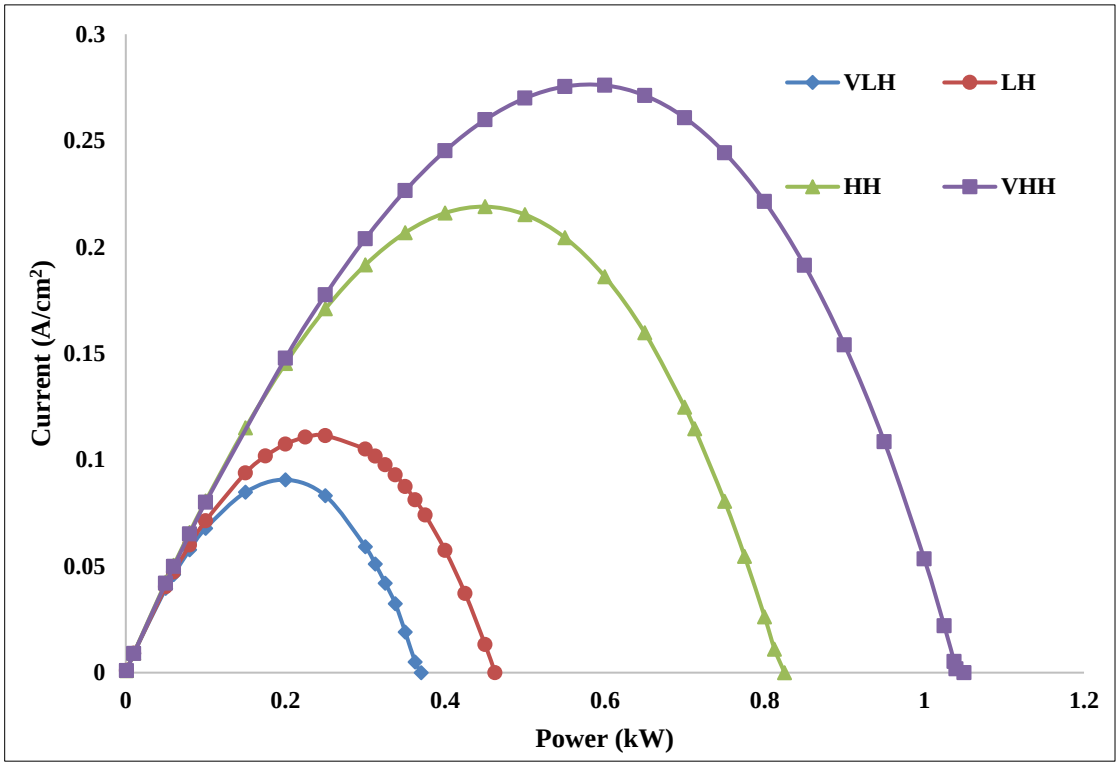

Figure 25 Current vs Power Characteristics of PEMFCs

The reason for these differences was that the membrane ionic conductivity was strongly linked to water concentration. According to (Lum and McGuirk 2005), the current extracted from a PEMFC is highly dependent on the membrane hydration, and for increasing humidity levels the membrane conductivity increased, allowing for higher current densities to be maintained before the ohmic loss became significant. The membrane conductivity model developed by (Springer, Zawodzinski and Gottesfeld, 1991) and applied by (Islam, 2012) showed that the membrane ion conductivity was indeed a function of the water content on the anode side of the membrane, which increased from a mass fraction of 0.273 at VLH to 0.705 at VHH. These results were in agreement with the numerical study performed by (Lee and Hwang, 2009), who studied the performance of PEM fuel cells with parallel flow channels at various cathode relative humidity conditions, and found membrane ion conductivity to increase with increasing relative humidity, with the highest membrane ion conductivity observed at the inlet of the channel. Likewise, (Soomro et al., 2023), who applied a 3D-CFD model, showed that a fully humidified gas stream flowing through the channels resulted in about 10% higher current density than at low humidity, confirming that humidity was a key operating variable of the PEMFC.

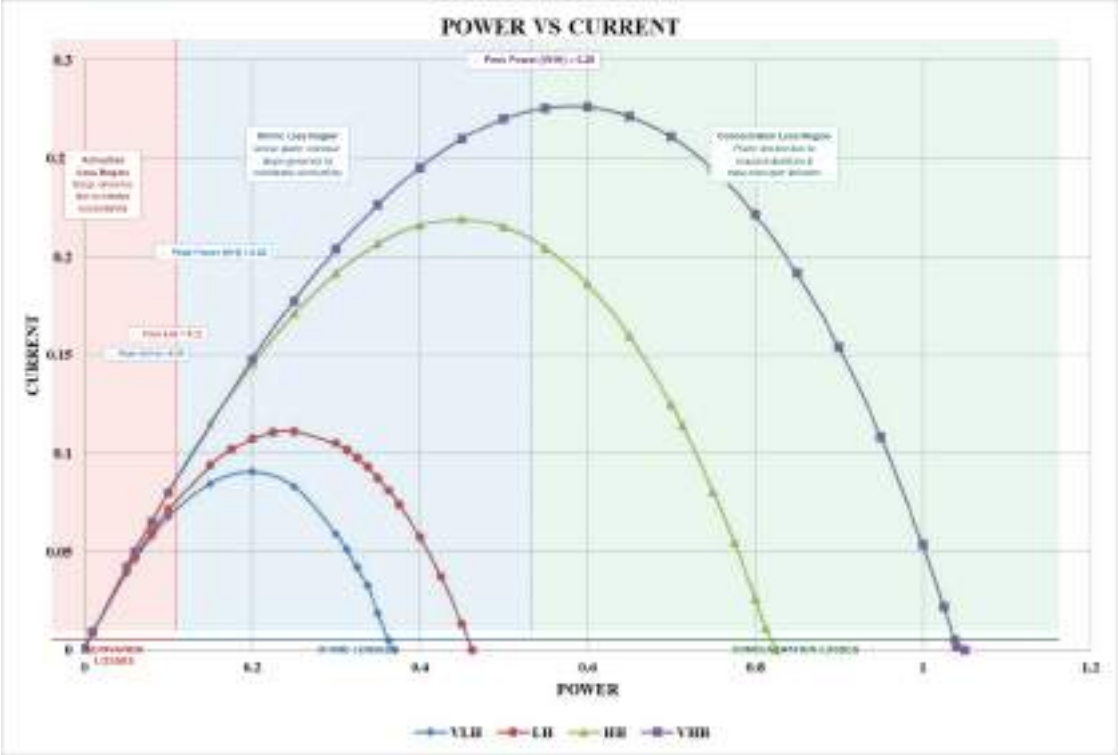

Figure 26 Losses Regions in Power vs Current Curves

The power curves were also of varying width in the four cases as shown in figure 26. The VLH curve was relatively "narrow" (current density range of 0-0.35 A/cm² to reach zero power). The VHH curve was much broader, reaching a current density of around 1.05 A/cm². This suggests that the VHH condition was able to maintain electrochemical activity over a greater range, in agreement with the results of (Hashemi, Rowshanzamir and Rezakazemi 2012) and (Berning and Djilali 2003). It was also noted that the HH and VHH curves were spaced further apart than the VLH and LH curves, suggesting that the humidification effects were not linear. But the single-phase model was unable to account for water flooding, and as such, the VHH curve was likely to have over-estimated the performance, as discussed by (Lum and McGuirk, 2005). As (Kulikovsky and Reshetenko, 2026) pointed out, one of the key issues in improving PEM fuel cell performance is the effective management of water, as the presence of liquid water can significantly slow down the transport of oxygen to the reaction sites - something that is impossible to model in the current single-phase approach.

4.4 Effect of Porosity

The influence of GDL porosity on cell performance was evaluated for three different values (0.4, 0.6 and 0.8) at constant permeability of 1.76×10^{-11} m² under the VHH

condition that was chosen due to the broadest operating range and to decouple the GDL transport from the membrane dehydration effects (Lum and McGuirk, 2005).

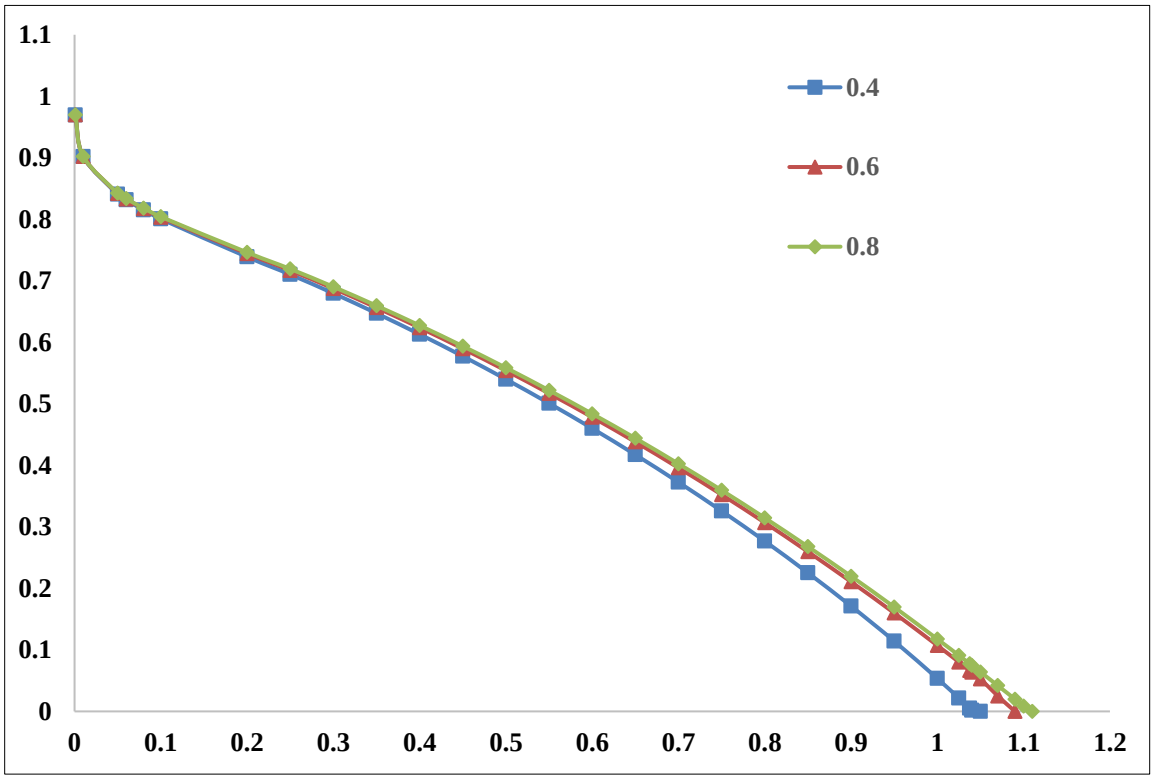

Figure 27 Current vs Voltage on different porosities

At lower current densities, the three curves overlap as shown in figure 27, suggesting that when oxygen was not scared, the effect of porosity was negligible. The curves split at currents greater than 0.5 A/cm² - the 0.4 case reached its limiting current at around 1.0 A/cm², whereas 0.6 and 0.8 cases continued to around 1.05 and 1.08 A/cm² respectively. This was due to the increased void fraction which decreased resistance to oxygen transport within the GDL, with the effective diffusivity in the GDL scaling as the square of porosity according to the Bruggeman correlation (Berning and Djilali, 2003). As (Hossain, Islam and Pollard, 2012) and (Islam, 2012) reported, the effective diffusivity of the GDL was a key factor in species transport and had the most impact at high current densities where mass transport limited the cell performance. The gain between 0.6 and 0.8 was less than that between 0.4 and 0.6, suggesting that the benefits of increasing porosity diminish with increasing porosity.

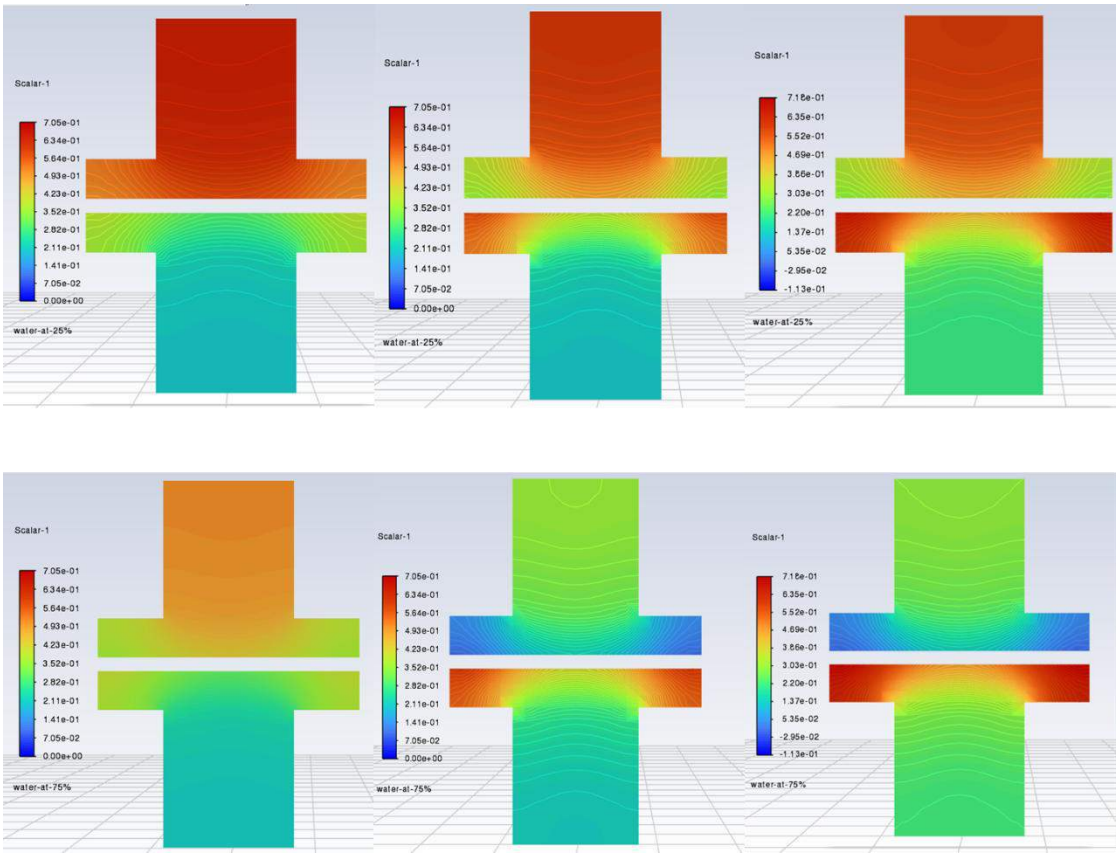

Figure 28 Water Vapour Mass Fraction Contour Plot at 0.4 Porosity, at channel length 25mm(near to inlet)(Top) and at 75mm(near to outlet)(Bottom) on three different current densities 0.25(left), 0.7(middle), 1.0(right) Acm^{-2}

Mass fraction contours of the water vapour mass fraction at 0.4 GDL porosity clearly show a dependence on current density as well as on the axial position as shown in figure 28. The distribution of the mass fraction of the vapour also remains relatively moderate and uniform across all three current densities, but in the region just outside the inlet (25 mm) the mass fraction of the vapour becomes significantly larger, particularly at current densities of 0.7 and 1.0 Acm^{-2}, which reflects progressive accumulation of water along the channel as the electrochemical reaction proceeds, similar to the results reported by (Berning and Djilali, 2003) and (Sivertsen and Djilali, 2005) shown in figure 28. The increasing concentration gradients across the GDL channel interface with increasing current densities are indicators of increasing diffusion resistance which directly contributes to the limitations in the transport of reactants in high-load operating conditions.

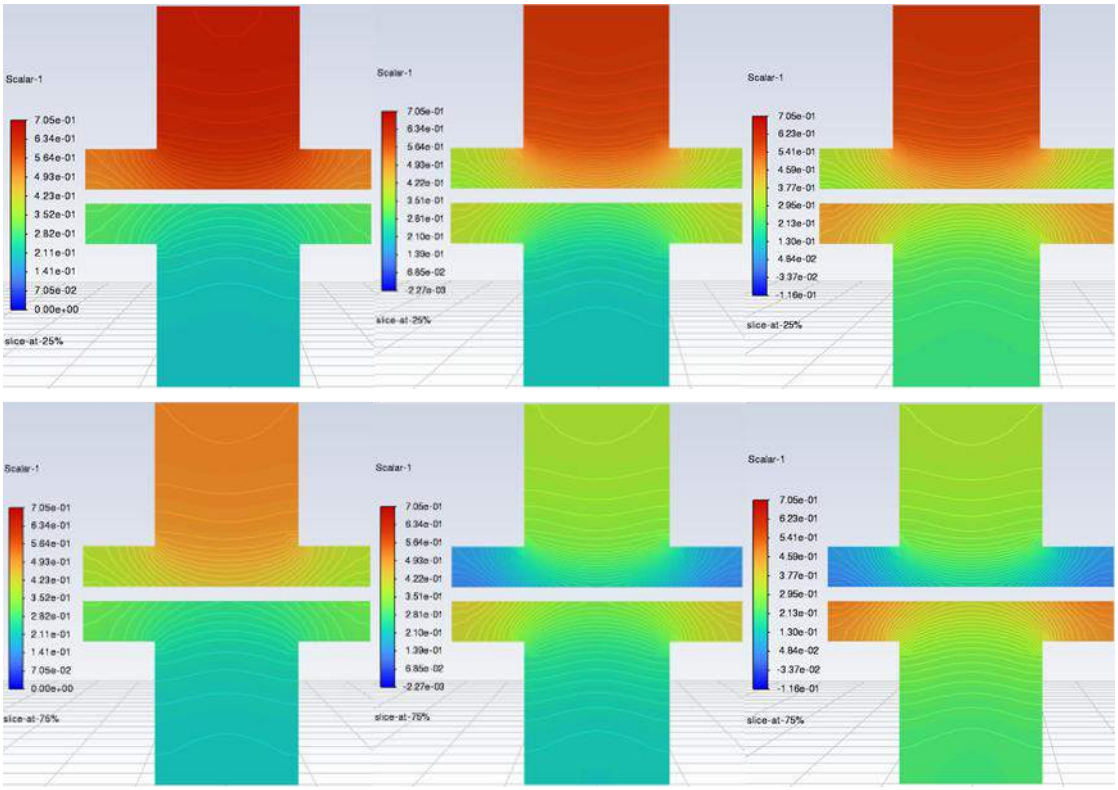

Figure 29 Water Vapour Mass Fraction Contour Plot at 0.6 Porosity, at channel length 25mm(near to inlet)(Top) and at 75mm(near to outlet)(Bottom) on three different current densities 0.25(left), 0.7(middle), 1.0(right) Acm^{-2}

With the porosity of 0.6, mass fraction contours of water vapours display the same overall trends as the 0.4 case porosity, namely, increasing accumulation towards inlet, outlet and steepening gradients with increasing current density. Nevertheless, the gradients of the GDL-channel interface are found to be, on the whole, smoother at 0.6 porosity (figure 29), which indicates an increase in the effective diffusivity due to the higher void fraction, as is the case with the Bruggeman correction where the effective diffusivity scales with porosity to the power of 1.5 (Berning and Djilali, 2003). This implies that the increased porosity moderately enhances the ability to transport water vapour away without the catalyst layer under high current density conditions where diffusion limitations are the most prominent trend observed. The scalar values seen at 1.0 Acm^{-2} agrees with the contour interpolation artefact seen in the 0.4 porosity results.

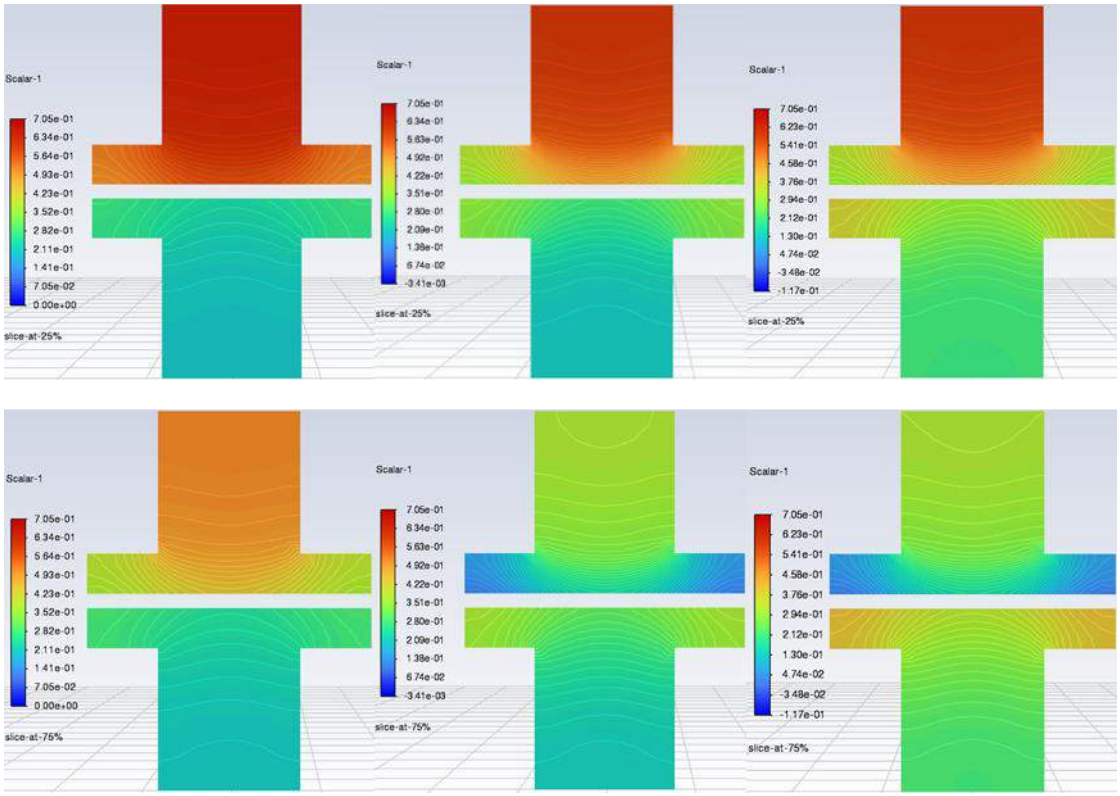

Figure 30 Water Vapour Mass Fraction Contour Plot at 0.8 Porosity, at channel length 25mm(near to inlet)(Top) and at 75mm(near to outlet)(Bottom) on three different current densities 0.25(left), 0.7(middle), 1.0(right) Acm^{-2}

The water vapour mass fraction contours at 0.8 GDL (as shown in figure 30) porosity have the same overall behaviour as that of 0.4 and 0.6 - the mass fraction of vapour rises with distance to the inlet (25 mm) and the outlet (75 mm). The peculiarity here is that the gradients of the GDL channel interface seem the smoothest of the three cases of porosity, again in keeping with the Bruggeman correction (Berning & Djilali, 2003). Transport of water vapour between the catalyst layer and the channel is therefore most efficient at this porosity which reduces localised saturation when operating with high current densities. Nevertheless, the marginal change between 0.6 and 0.8 seems smaller than the marginal change between 0.4 and 0.6, implying diminishing returns, a behaviour that has also been observed by Mohammedi et al. (2020) and Ghasabehi et al. (2024) where excessive high porosity can be detrimental to electrical conductivity and mechanical stability of the GDL despite enhancing mass transport. The negative scalar values at 1.0 Acm^{-2} (down to -1.17 x 10^{-1}) once again represent the contour interpolation artefact that was observed in the previous cases.

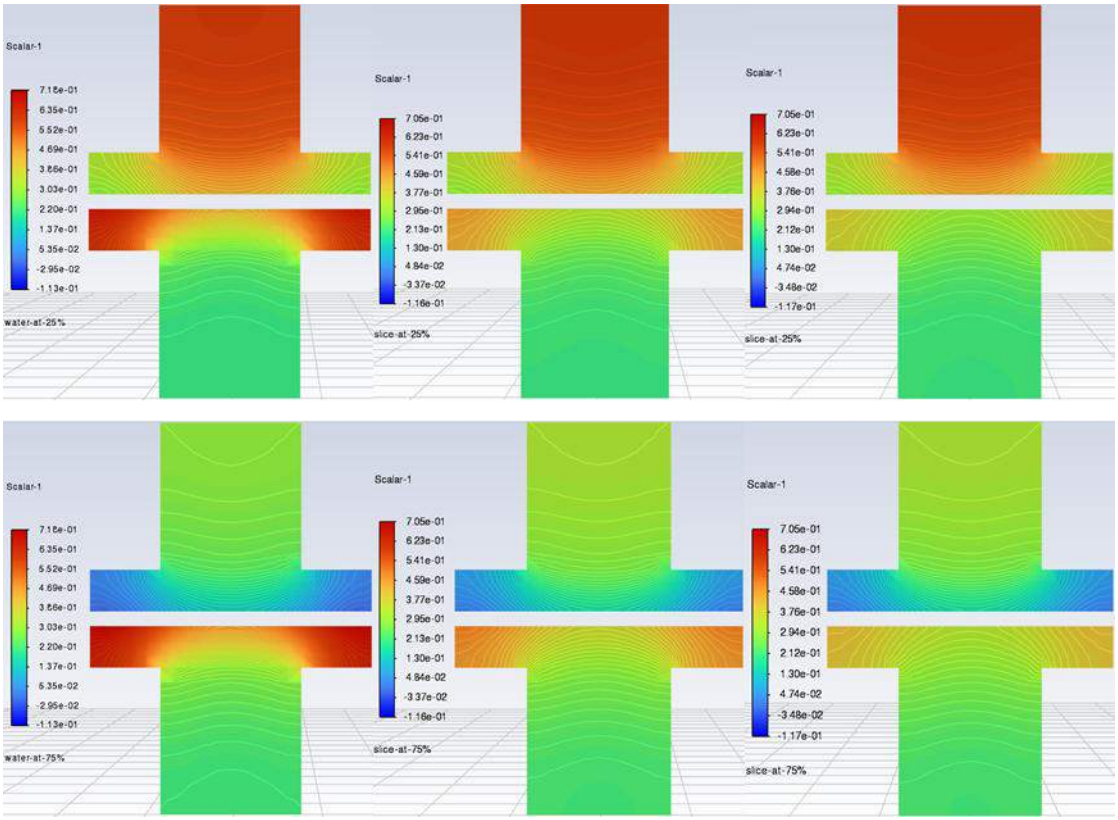

Figure 31 Water vapour Mass fraction contour plot at 1.0 Acm^{-2} on different porosity 0.4(left), 0.6(middle), 0.8(right) at 25mm(near to inlet)(Top) and 75mm(near to outlet)(Bottom)

The comparison at a fixed current density of 1.0 Acm^{-2} (as shown in figure 31) isolates the influence of the porosity of GDL on the distribution of water vapour. It increases at an under-rib convection rate and cross-diffusion - a critical pathway frequently rate-limiting at high current densities - is becoming increasingly homogeneous across the channel with sharp gradients towards the rib areas at 0.4 porosity, 0.6 porosity, and 0.8 porosity, respectively. It also seems that the vapour fraction in the core of the channels is a little lower at 0.8 porosity, indicating that it might evacuate product water at a faster rate and it might be less prone to floods. The influence of porosity is enhanced further downstream (75 mm) where cumulative water production magnifies the influence of the diffusion bottleneck on the performance in the lower-porosity scenario, confirming that porosity optimisation has its most significant practical effect under high-current, downstream operating conditions.

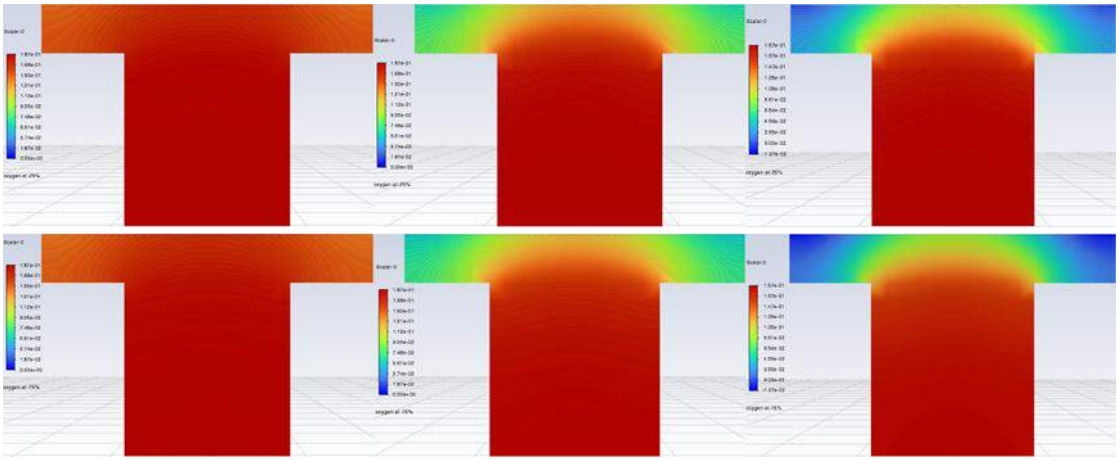

Figure 32 Oxygen Mass Fraction Contour Plot at 0.4 Porosity, at channel length 25mm(near to inlet)(Top) and at 75mm(near to outlet)(Bottom) on three different current densities 0.25(left), 0.7(middle), 1.0(right) Acm^{-2}

The contours of the oxygen mass fraction at 0.4 GDL (as shown in figure 32) porosity depict a complementary relationship to the vapour generating regions cavities mentioned above - as oxygen is consumed at the cathode catalyst layer, the location of oxygen consumption complements the regions of vapour generation. The channel and GDL at 0.25 Acm^{-2} are nearly uniformly saturated with oxygen, showing plenty of reactant availability and negligible diffusion limitation. An identifiable depletion zone is formed within the GDL underneath the channel and the lowest oxygen concentration is seen at the catalyst layer interface - a clear indication of reactant transport limitation. This depletion further downstream (75 mm), cumulative oxygen consumption with decreasing partial pressure results in steepest concentration gradients. This behaviour is consistent with mass transport of oxygen (controlled by diffusion), as demonstrated by Fick, and is also compatible with classical observations such as by (Springer et al. 1991) and Berning and Djilali (2003), where mass starvation to high current density becomes the performance limiting mode in PEM fuel cells in cathodes.

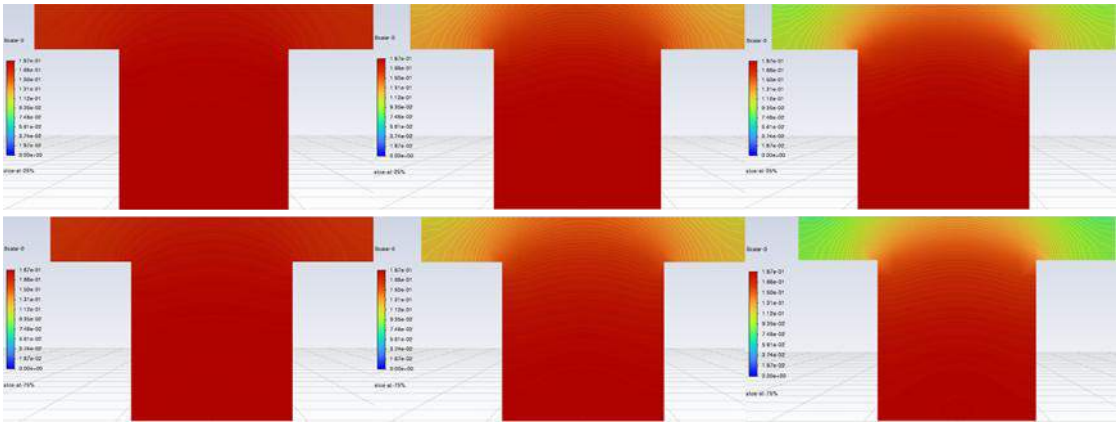

Figure 33 Oxygen Mass Fraction Contour Plot at 0.6 Porosity, at channel length 25mm(near to inlet)(Top) and at 75mm(near to outlet)(Bottom) on three different current densities 0.25(left), 0.7(middle), 1.0(right) Acm^{-2}

The oxygen mass fraction contours at the 0.6 GDL (as shown in figure 33) porosity indicates that the depletion zone in the GDL is decidedly less extreme and more laterally dispersed than the porosity of the GDL at 0.4 GDL porosity. At a lower concentration of 1.0 Acm^{-2}, oxygen reaches the catalyst layer in at least higher residual concentration, and gradient across the GDL thickness is less steep - indicating reduced difficulty in diffusion according to the higher residual concentration available due to the higher open volume fraction. Nevertheless, the steepest oxygen starvation was observed at a downstream location (75 mm), with the 0.4 porosity scenario leading to a better oxygen availability; at 0.6 porosity, the under-rib regions are also observed to better retain oxygen, which suggests enhanced cross-diffusion. This confirms that an increase in porosity can be used to directly counter the limit of reactant transport at higher current densities seen in the studies by (Sivertsen and Djilali, 2005) and (Mohammedi et al., 2020).

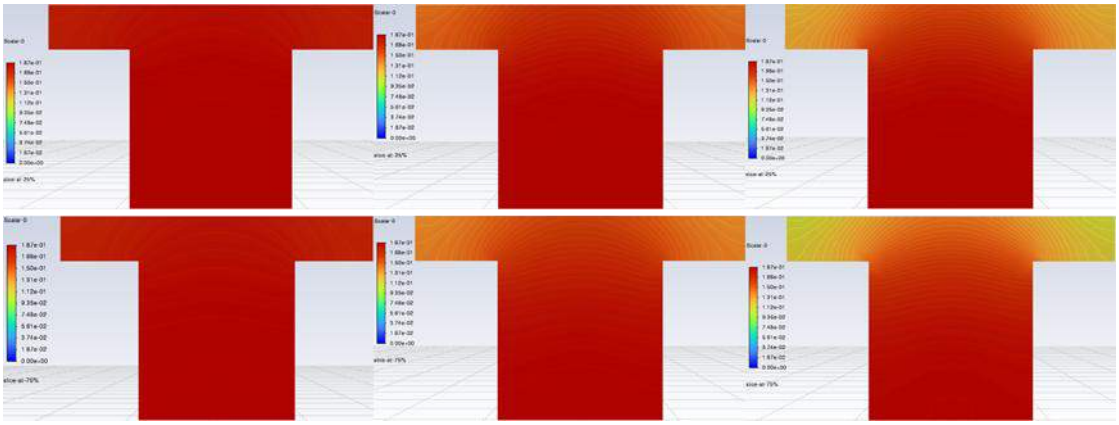

Figure 34 Oxygen Mass Fraction Contour Plot at 0.8 Porosity, at channel length 25mm(near to inlet)(Top) and at 75mm(near to outlet)(Bottom) on three different current densities 0.25(left), 0.7(middle), 1.0(right) Acm^{-2}

The oxygen distribution is most uniform at 0.8 porosity (as shown in figure 34), with the interface between the catalyst layer and the gas phase holding the most residual oxygen even at 1.0 Acm^{-2}. The visual appearance of the footprint of lateral depletion beneath the channel is clearly reduced, and the availability of gas-phase oxygen beneath the ribs is approaching that of the core of the channel itself which indicating that gas-phase diffusion is no longer the limiting factor at this pore size. This downstream (75 mm) penalty of 0.4 and 0.6 respectively is largely suppressed here, implying that convective-diffusive coupling in the GDL is effective enough to replenish consumed oxygen across the channel length (Perng & Wu, 2015).

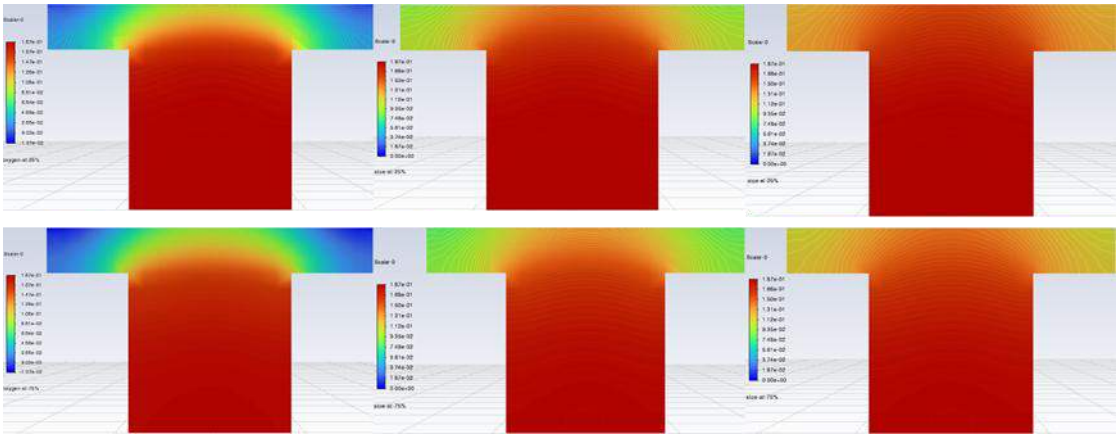

Figure 35 Oxygen Mass fraction contour plot at 1.0 Acm^{-2} on different porosity 0.4(left), 0.6(middle), 0.8(right) at 25mm(near to inlet)(Top) and 75mm(near to outlet)(Bottom)

The side-by-side comparison of porosity indicates that there has been a definite progression of the shape and depth of the depletion plume above the channel at a constant of 1.0 Acm^{-2} as shown in figure 35. With the plume being deep, narrow, and cuts sharply into the GDL, it signifies over local consumption that the oxygen replenishment to the plume in this area is being outpaced by the consumption. The plume at 0.6 porosity expanded and shallowed indicates that the refilling of the depleted areas by diffusive flux transverse to the plume is occurring more readily. When porosity is 0.8, the plume becomes very wide and diffuse and near the equilibrium concentration of the bulk stream diffusion is an important signature of a diffusion-dominated equilibrium in which the GDL no longer exerts any meaningful resistance. This reduction of the inlet-to-outlet contrast also decreases gradually with the porosity and indicates that the decay of axial reactants along the channel is the limiting factor only when the porosity has become sufficiently relaxed (Ghasabehi et al., 2024).

4.5 Effect of Permeability

The polarisation curves show that the performance of the PEM fuel cell is dependent on the GDL permeability in the three target loss regions as shown in figure 36. In the region of loss of activation (low current density, up to 0.1 Acm^{-2}), all three curves follow closely since the activation overpotential is controlled by catalyst kinetics and is mostly independent of GDL permeability. The curves are almost indistinguishable by the ohmic loss region (at approximately 0.06 Acm^{-2}) because the ohmic resistance is determined by the resistances of the membrane and contacts, and not by the transport properties of gases at the same temperature. This apparent separation is already observed in the region of loss of concentration (above ~0.7 Acm^{-2}) where transport of the reactants is already the rate-limiting factor. In this case, higher permeability case (K = $1.76x10^{-8}$) supports higher voltages and reaches a significantly higher limiting current density (approximately 1.05 Acm^{-2}), and lower permeability cases ($1.76x10^{-11}$ and $1.76x10^{-12}$) fail earlier, at a relatively lower limiting current density (~1.02-1.03 Acm^{-2}). It also means that at a certain point, additional penalty cannot be achieved by further reduced permeability thus meaning that at a certain point, the two lower permeability curves almost coincide implying that at a certain minimum, we can achieve additional penalty by further reduced permeability arguing that the two lower permeability curves almost coincide, at a certain minimum.

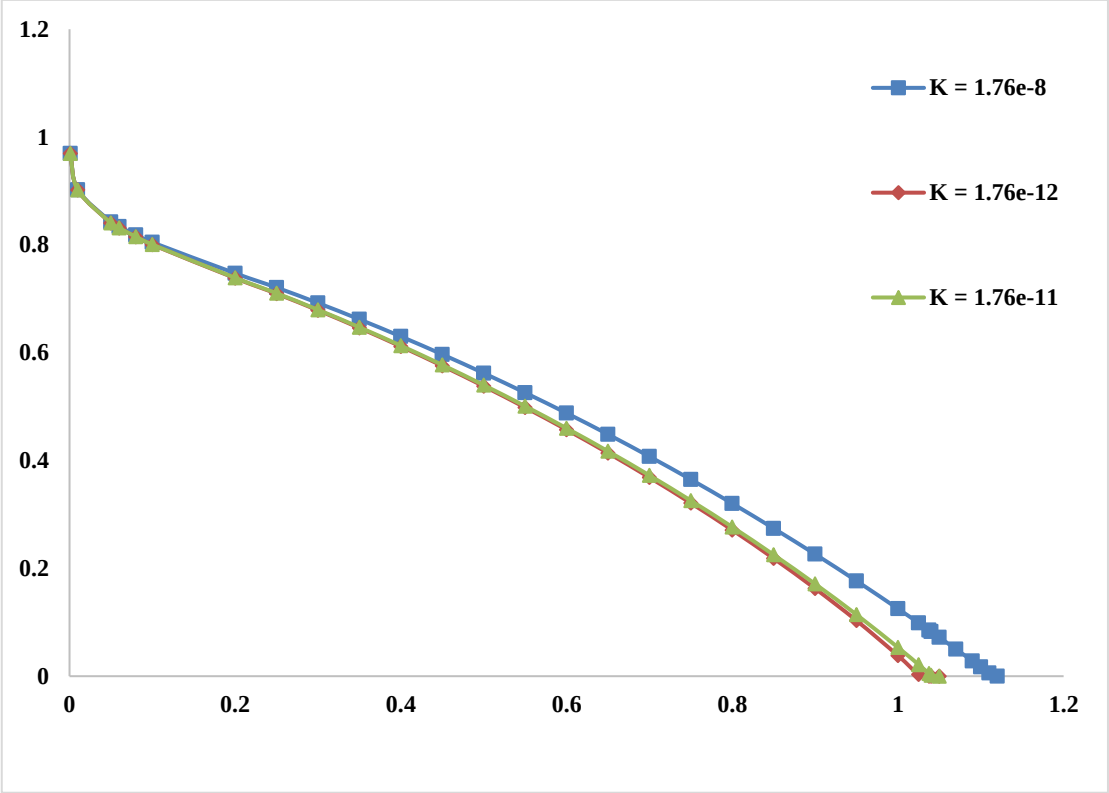

Figure 36 Polarisation Curves on different Permeabilities

The chosen K = 1.76 x 10^{-11} is well-justified physical and methodological grounds. The value lies within realistic permeability range reported in the commercial carbon-paper GDLs under realistic fuel cell compression conditions, making this value directly comparable to the experimental literature and even configurations of industry relevance (Berning and Djilali, 2003; Mohammedi et al., 2020). The extremely high value of 1.76 x 10^{-8} would over- characterize convective transport and obscure the diffusion- limited behaviour the present thesis specifically seeks to explore. By the choice of 1.76 x 10^{-11}, under high current densities, the study is capturing realistic transport-limited behaviour when operating under physically significant conditions where the effects of geometric modification of the rectangular cathode baffles can be assessed under physically meaningful operating conditions in which the impact of geometric modification of the rectangular cathode baffles is to be evaluated.

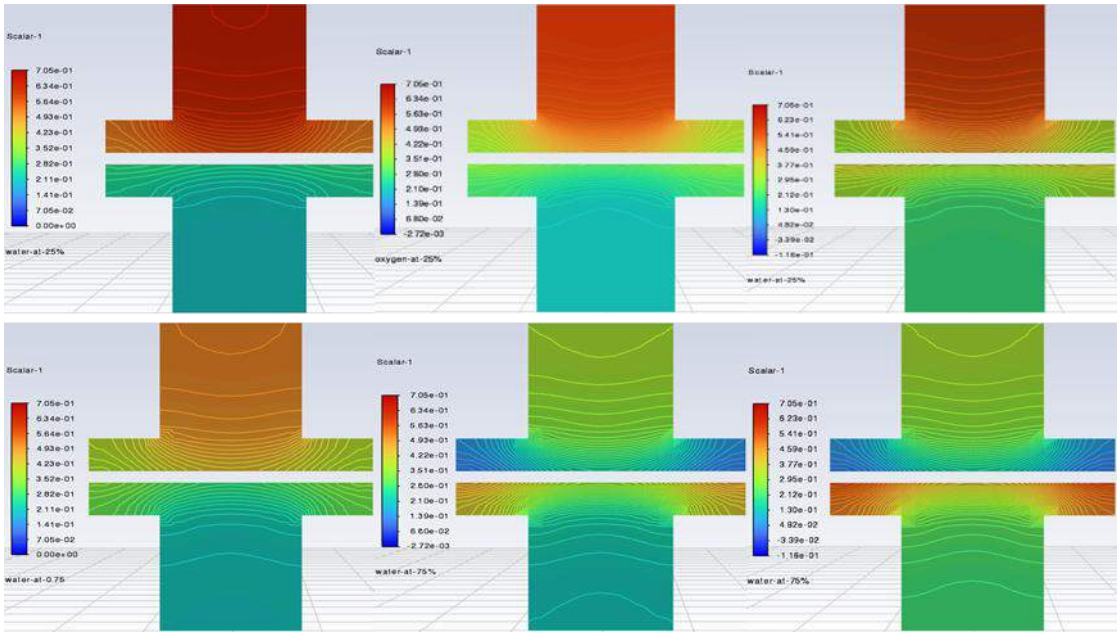

Figure 37 Water Vapour Mass Fraction on K = 1.76e-8 & three current densities 0.25(Left), 0.7(Middle), 1.0(Right) at two different channel lengths 25mm (near to inlet) (Top) & 75mm (near to outlet) (Bottom)

The profiles (figure 37) reveal that the maximum mass fraction of water vapour (=7.05 × 10^{-1}) at the membrane-CL interface due to electro-osmotic drag, with a decreasing concentration gradient through the GDL into the channel core driven by back-diffusion and convective removal. The gradient is shallow, at 0.25 A/cm^2 the high-vapour layer deepens and extends deep into the GDL, and the production rate surpasses the removal rate, approaching saturation conditions that favour flooding (Berning and Djilali, 2003; Ghasabehi et al., 2024).

Streamwise, the slice at the channel length 25 mm is laterally symmetric, whereas at 75 mm, the region of high concentration is expanded through cumulative build-up of water on the channel (Perng and Wu, 2015). The H_2O-O_2 relationship observed along the reaction path, is typical of (Springer et al., 1991).

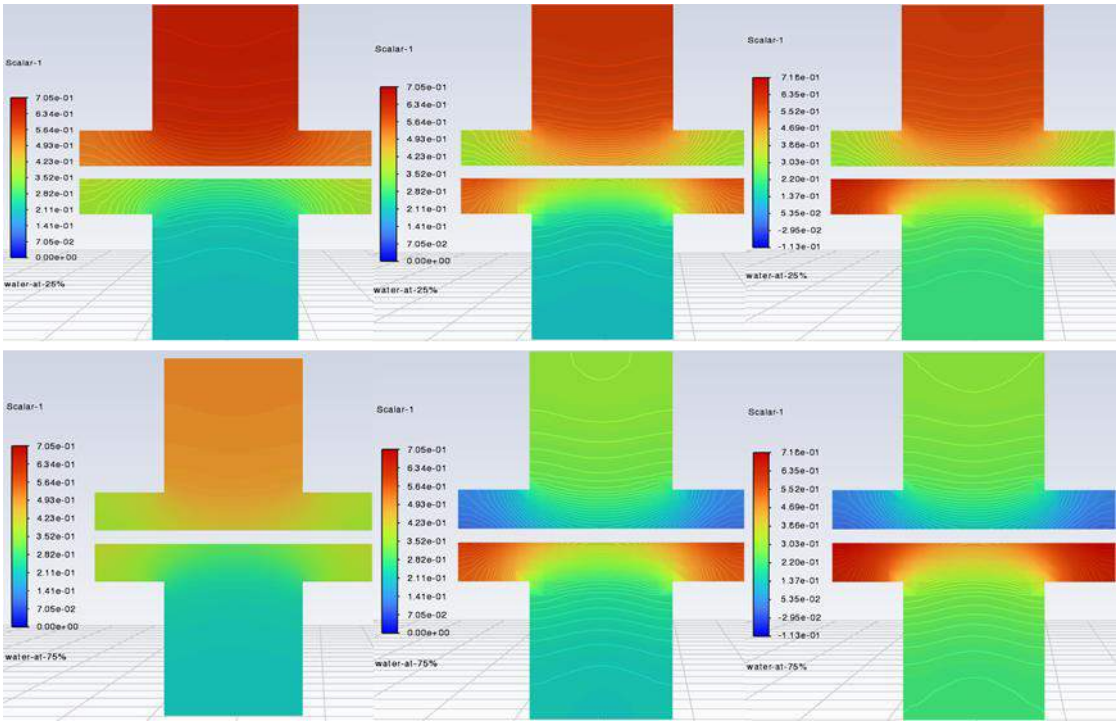

Figure 38 Water Vapour Mass Fraction on K = 1.76e-11 & three current densities 0.25(Left), 0.7(Middle), 1.0(Right) at two different channel lengths 25mm (near to inlet) (Top) & 75mm (near to outlet) (Bottom)

Such a reduction of K, change of 1.76 x 10^{-8} impressed by 1.76 x 10^{-11} sharp, reduces the convective movement of the GDL, and causes the high-concentration band to move closer to the CL-GDL interface. The 75 mm slice at 0.7 and 1.0 A/cm^2 and the lower K show that the thickness accumulation in the reactant and membrane interface is heavier and the reactant-deficit at the contacts of the reactant and membrane is more localised and restricted (thicker mass) at the membrane interface and the reactant-deficit localised and restricted (negative scalar values) (Sivertsen and Djilali, 2005; Mohammedi et al., 2020). The case of higher K by contrast, has smoother gradients and higher distribution of vapour across the GDL, associated with improved crossflow and better management of liquid water (Li et al., 2025).

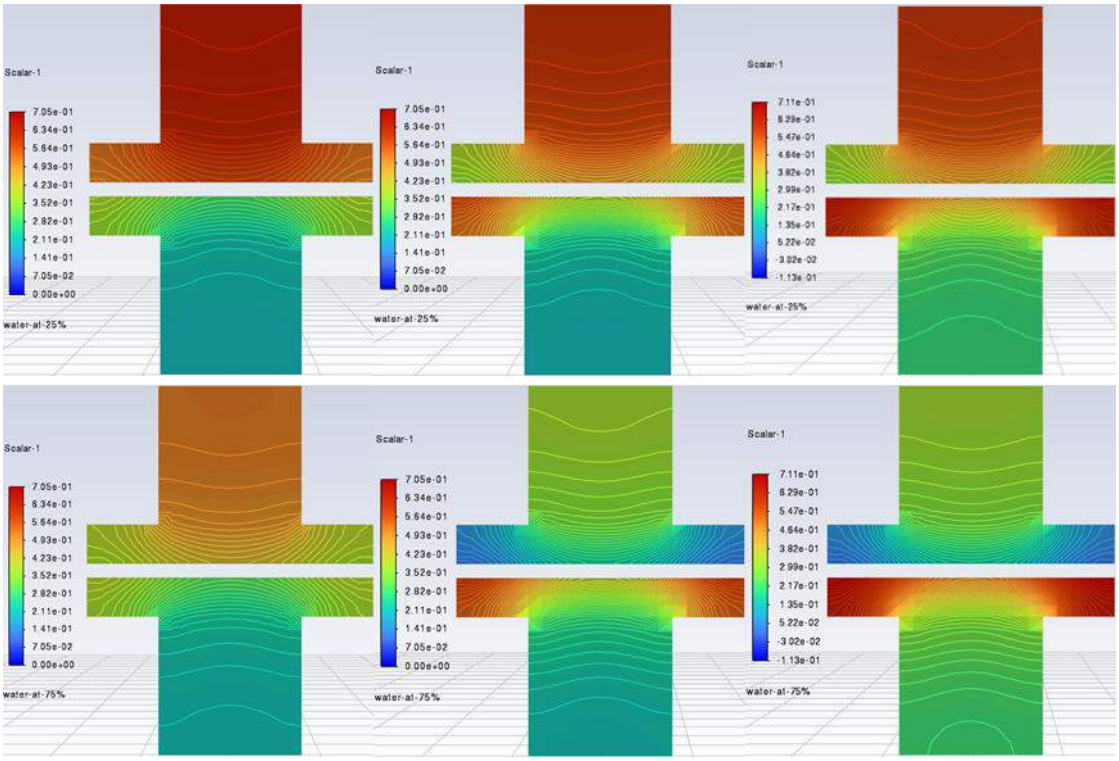

Figure 39 Water Vapour Mass Fraction on K = 1.76e-12 & three current densities 0.25(Left), 0.7(Middle), 1.0(Right) at two different channel lengths 25mm (near to inlet) (Top) & 75mm (near to outlet) (Bottom)

The steepest of the three cases is at K = 1.76 x 10^{-12}, which has the steepest through-plane vapour gradient. The reactant-deficit zones (negative scalar values down to -1.13 x 10^{-1}) appear earlier and also extend further laterally at 0.7 and 1.0 A/cm^2, especially at the 75 mm slice, indicating that convective transport can now be ignored and diffusion can no longer evacuate the product water. Compared to K = 1.76 × 10^{-8}, the difference is greater: smooth, widely distributed vapour field of the large-K case are replaced by sharp interfacial concentration and strong downstream stratification, confirming strong negative dependence of local saturation on GDL permeability when operating under high current (Mohammedi et al., 2020; Li et al., 2025).

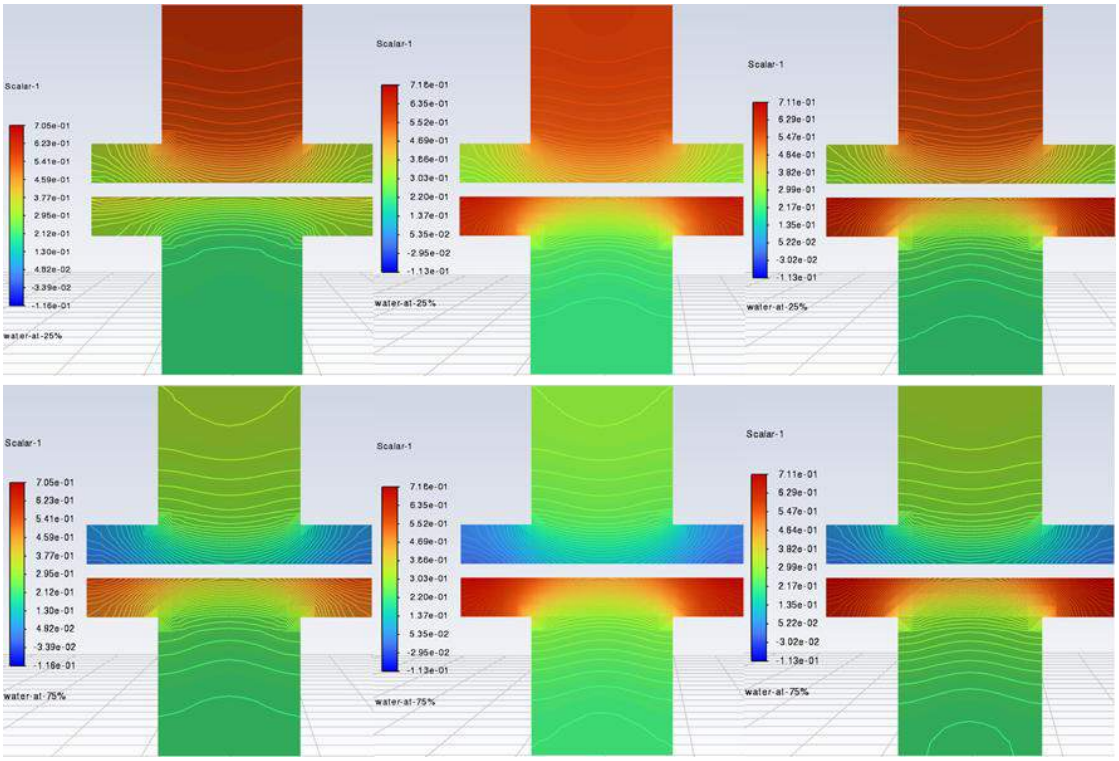

Figure 40 Water Vapour Mass Fraction on three different permeabilities K=1.76e-8(Left), K=1.76e-11(Middle), K=1.76e-12(Right) and on fixed current density of 1.0 at two different channel lengths 25mm(near to inlet)(Top) & 75mm(near to outlet) (Bottom)

In the side-by-side comparison (figure 40), the contribution of the GDL permeability to the water management is isolated at fixed high-current condition (1.0 A/cm^2). The K = 1.76 x 10^{-8} case presents a diffuse vapour field with broad lateral dispersion with weak interfacial confinement, indicating excessive convective bypass through the GDL that would, in practice, compromise mechanical integrity and control weak interfacial confinement. The opposite extreme of K = 1.76 x 10^{-12} case shows deep downstream stratification, deep accumulation of reactants between the reactor and the main boiler, and marked downstream stratification at 75 mm, which are characteristic of imminent flooding and mass-transport-limited operation.

This middle value K =1.76 x 10^{-11} case still has a clear, through-plane gradient with moderate interfacial vapour build-up but no saturation-induced breakdown. This range is also congruent to experimentally reported intrinsic permeabilities of commercial carbon-paper GDLs (Sivertsen and Djilali, 2005; Mohammedi et al., 2020), making it the most representative baseline to the current study.

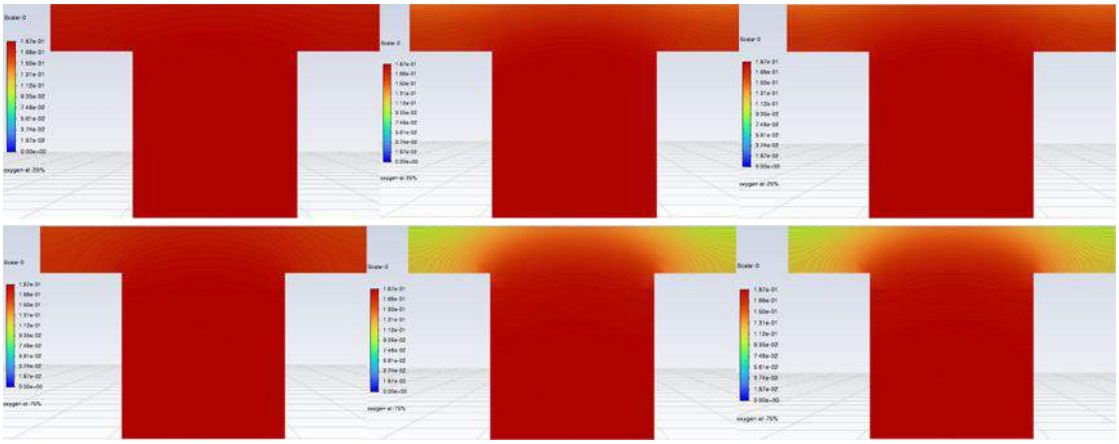

Figure 41 Oxygen Mass Fraction on K = 1.76e-8 & three current densities 0.25(Left), 0.7(Middle), 1.0(Right) at two different channel lengths 25mm (near to inlet) (Top) & 75mm (near to outlet) (Bottom)

At K = 1.76 x 10^{-8} the difference between inlet and outlet mass fraction of oxygen remains close to the inlet value (almost 1.87 x 10^{-1}) throughout the channel, and GDL across all three current densities (as shown in figure 41). At 25 mm there is near-uniform distribution with slight CL-side depletion, whereas with 0.7 and 1.0 A/cm^2 minimal CL-side depletion is observed at the GDL-CL interface. The large through-plane permeability maintains a vigorous convective O_2 supply and to keep localised starvation, just as a diffuse vapour field occurs previously at the same K (Berning and Djilali, 2003; Ghasabehi et al., 2024).

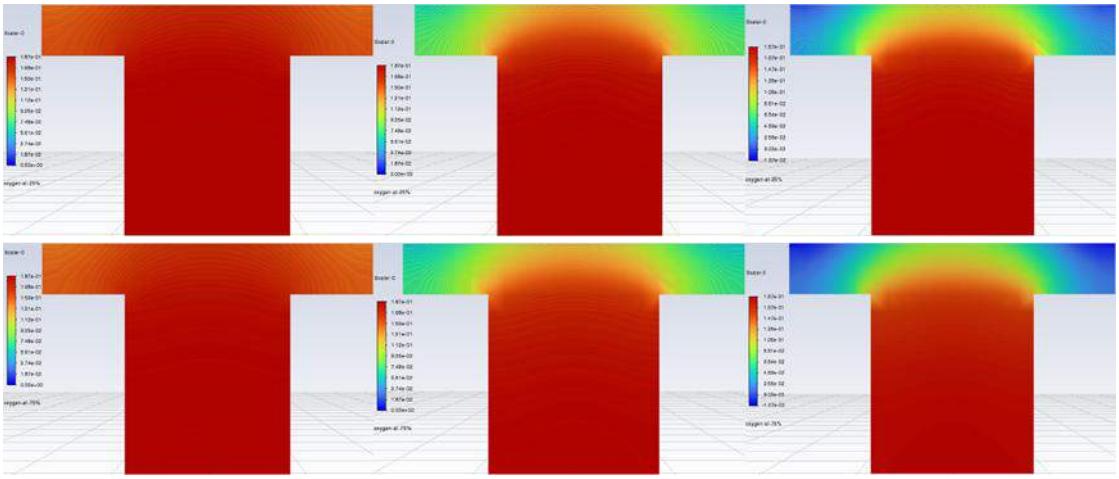

Figure 42 Oxygen Mass Fraction on K = 1.76e-11 & three current densities 0.25(Left), 0.7(Middle), 1.0(Right) at two different channel lengths 25mm (near to inlet) (Top) & 75mm (near to outlet) (Bottom)

At K = 1.76 × 10^{-11}, more oxygen depletion is observed than at K = 1.76 × 10^{-8} (as shown in figure 42). When the field reaches 0.25 A/cm^2 the field is still comparable to the high-K scenario, but with the field reaching 0.7 and 1.0 A/cm^2 a clear area of

depletion forms at the interface of the GDL and CL, and extends into the channel, with the 75 mm slice showing the strongest concentration drop (down to approximately 10^{-2}). The decrease in convective delivery of O_2 by diffusion due to the decreased value of the through-plane permeability is expected to occur (Sivertsen and Djilali, 2005; Mohammedi et al., 2020).

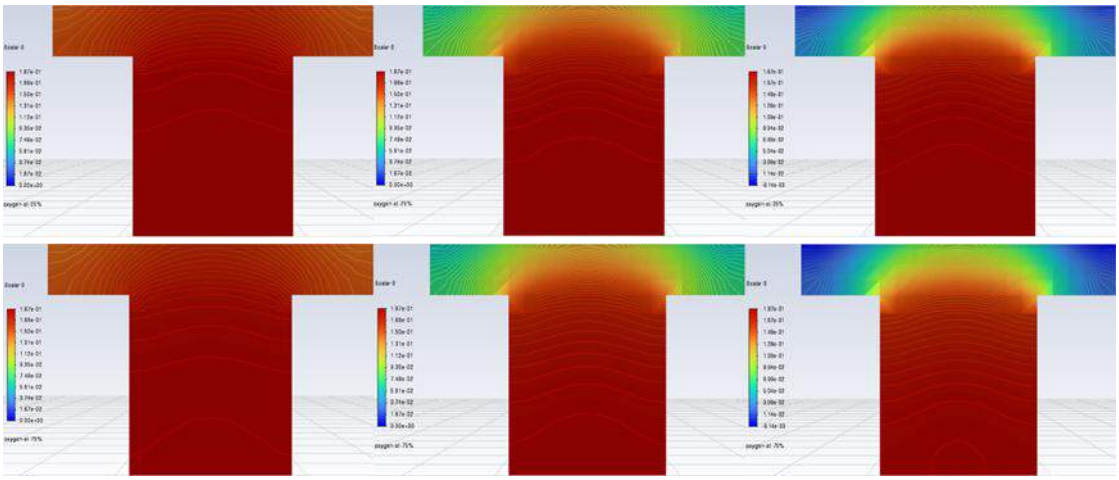

Figure 43 Oxygen Mass Fraction on K = 1.76e-12 & three current densities 0.25(Left), 0.7(Middle), 1.0(Right) at two different channel lengths 25mm (near to inlet) (Top) & 75mm (near to outlet) (Bottom)

At K = 1.76 x 10^{-12}, it is the most severe case of the three permeabilities, in the depletion of oxygen (as shown in figure 43). Although the field is smooth at 0.25 A/cm^2 the CL-side depletion is evident and the field shows minima of about 6 x 10^{-3} in the field that are at 75 mm slice with further spreading of the depletion zone well along the channel. The starvation region is wider and more intense than K = 1.76 × 10^{-11}, and it proves ineffectiveness of a single diffusive method of transporting O_2 to support the reactions requirement.

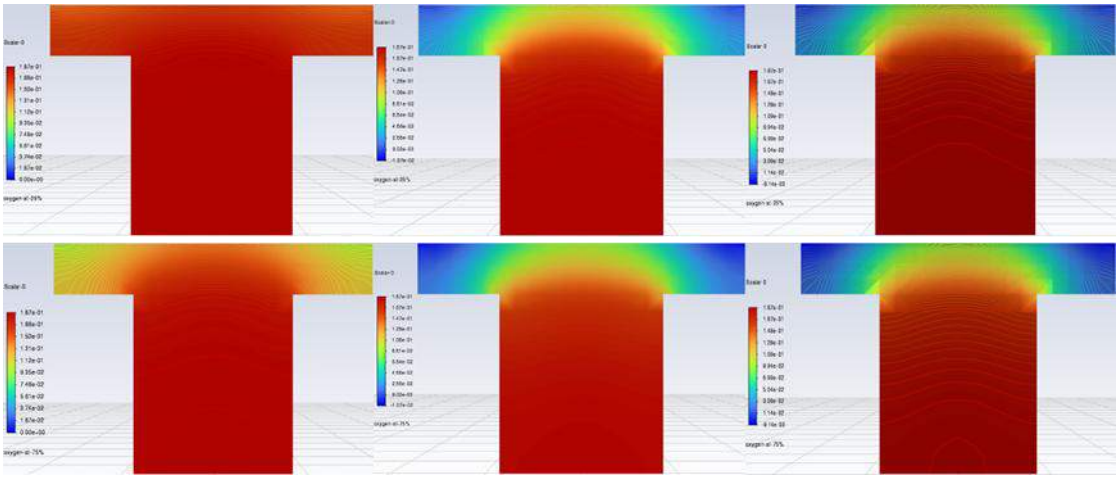

Figure 44 Oxygen Mass Fraction on three different permeabilities K=1.76e-8(Left), K=1.76e-11(Middle), K=1.76e-12(Right) and on fixed current density of 1.0 at two different channel lengths 25mm(near to inlet)(Top) & 75mm(near to outlet) (Bottom)

Under fixed currents value of 1.0 A/cm^2, the side-to-side comparison demonstrates three different transport regimes. K = 1.76 × 10^{-8} ensures that there is a near uniform distribution of O_2 across the GDL and channel with negligible CL-side depletion, which reflects convection-dominated supply (as shown in figure 44). K = 1.76 x 10^{-12} indicates that severe interfacial starvation (~6 x 10^{-3}) takes place and there is lateral extension to the channel indicating that it is diffusion-limited transport and performance is soon to collapse. The depletion gradient between these extremes is clear yet moderate in depleting reactants to the CL yet still realistically captures mass-transport resistance.

This intermediate value was chosen to be used in the study because it lies within the range of non-physical convect (higher K) bypass or lower K artificial starvation (Sivertsen and Djilali, 2005; Mohammedi et al., 2020).

Chapter 5: Effects of Partially Blocking Channels (Baffles)

In conventional straight cathode channel, reactant transportation from the flow channel to the catalyst layer is mainly based on molecular diffusion in the GDL. However, at high current densities, this diffusion-based mechanism is not enough: oxygen consumption rate is greater than the replenishment; a large concentration overpotential appears and a liquid water layer forms in the pores of GDL which closes the available transport paths, leading to the characteristic voltage drop seen in the polarisation curve. To overcome this, rectangular baffle plates were added across the cathode flow channel geometry models as shown in figure 45, 46, 47.

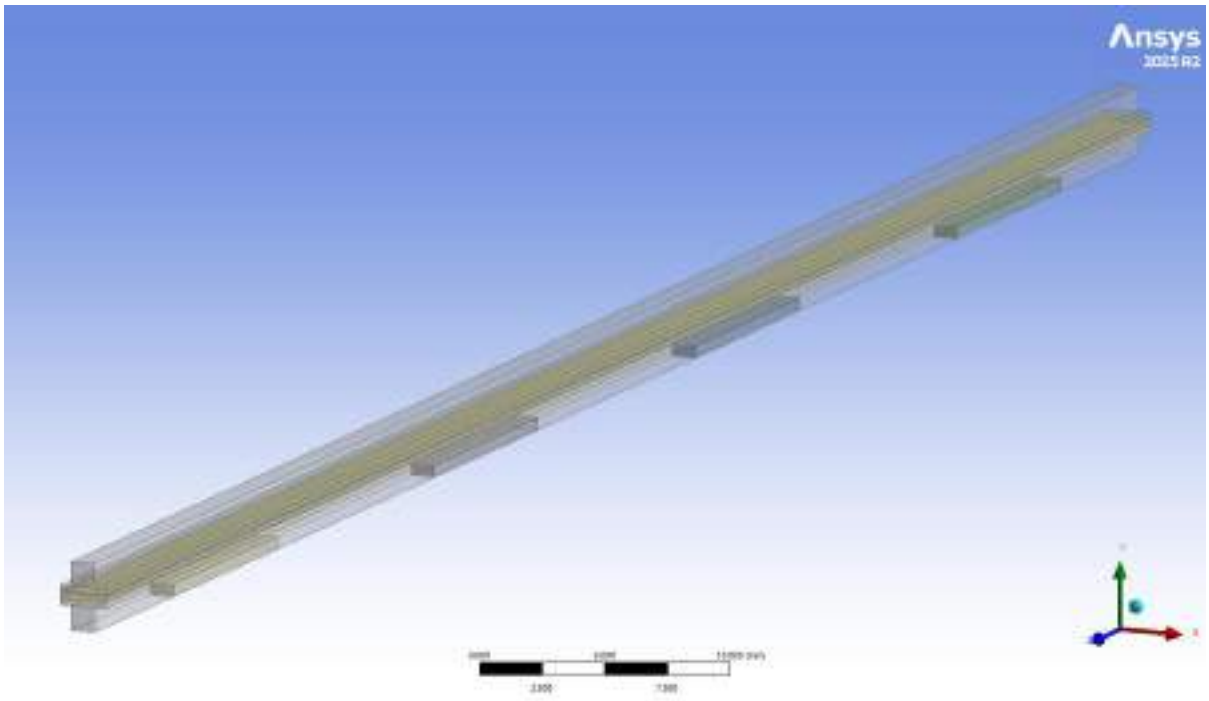

Figure 45 Isometric View of PEMFC with Baffles

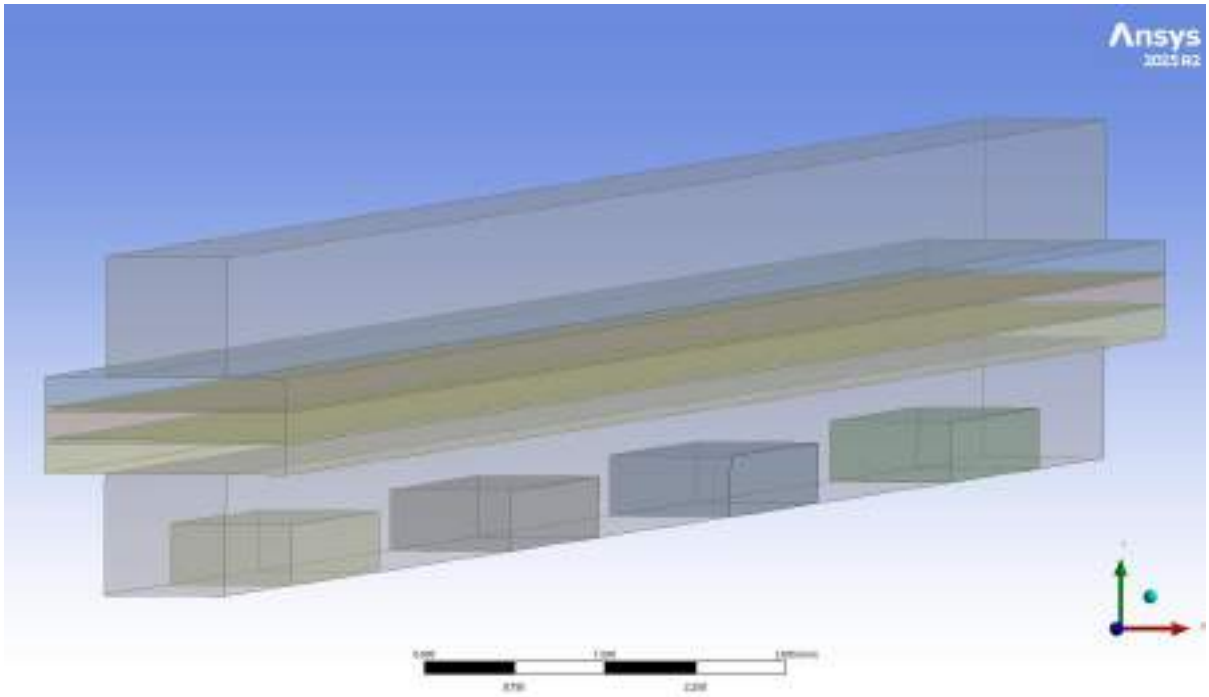

Figure 46 Isometric View of PEMFC with Baffles

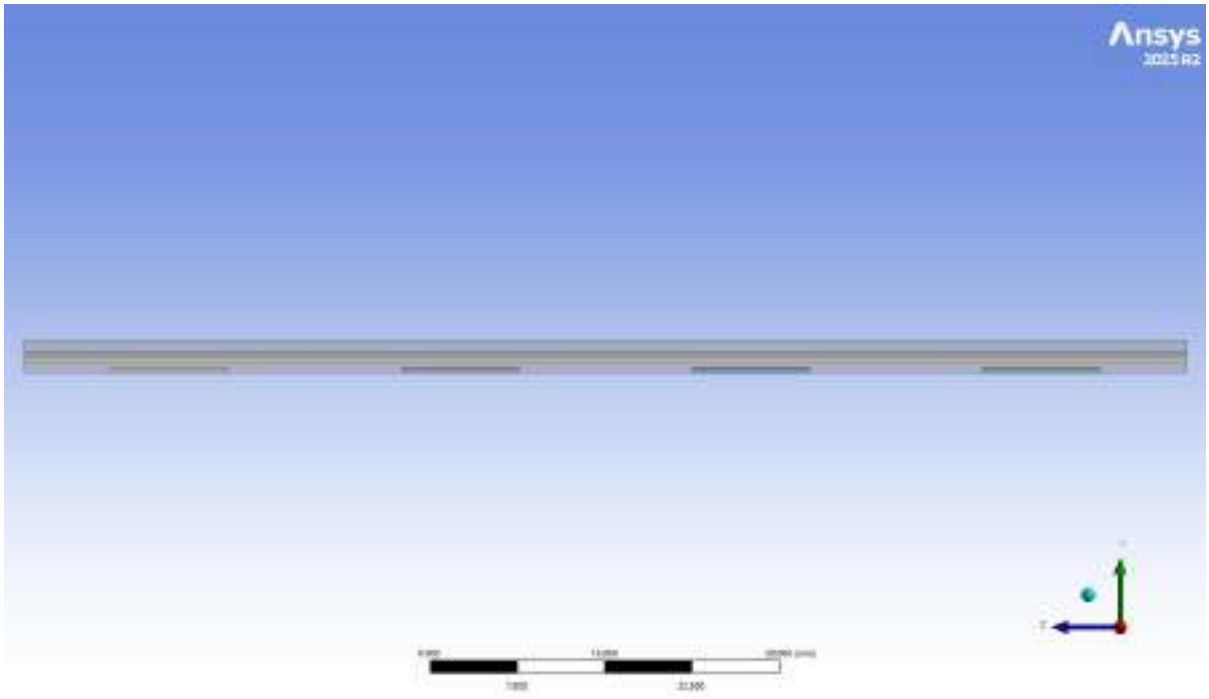

Figure 47 Side View of PEMFC with Baffles

The baffles partially close the cross section of the channel, which results in an increase of the mainstream cathode flow velocity through the remaining gap between the baffle tip and the GDL surface. This local acceleration creates a pressure gradient pointing towards the porous electrode, changing the predominant transport mechanism of the reactant from passive

diffusion to forced convection. (Soong et al. 2005) and (Yin et al. 2018) have shown that this convective penetration results in oxygen-enriched regions in the GDL and CL, which will directly reduce the oxygen concentration overpotential and enhance the delivery of reactant to the active reaction sites. The geometry models show the cathode channel assembly which consists of the flow channel, the GDL, and the catalyst layer; rectangular baffles were placed on the channel wall at regular intervals along the length of the channel.

The main goal of this parametric study was to increase the through-plane mass velocity flux in the cathode GDL and CL to increase convective transport of oxygen to the electrochemically active surface and to reduce reactant starvation at the high current densities. This performance increase comes with a necessary increase in channel pressure drop, however, because there is more flow resistance added because of each baffle. Thus, the balance between better convective transport and higher-pressure penalty is the key engineering challenge of optimization of the baffles and both effects are studied systematically for all of the cases studied here.

Two parametric studies were carried out: one changing the number of baffles (Cases 1–3) and the other changing the baffle height (Cases 4–7) while keeping the number of baffles constant at four, to systematically quantify the effect of baffle blockage on velocity distribution and pressure drop within the cathode porous layers.

CASE	Details
CASE 0	Straight Channel (No Baffles)
CASE 1	Number of Baffles (***2***) with fixed height (*0.5mm*) and depth(*10mm*)
CASE 2	Number of Baffles (***3***) with fixed height (*0.5mm*) and depth(*10mm*)
CASE 3	Number of Baffles (***4***) with fixed height (*0.5mm*) and depth(*10mm*)
CASE 4	Height (***0.2mm***) with fixed number of Baffles (*4*) and depth(*10mm*)
CASE 5	Height (***0.3mm***) with fixed number of Baffles (*4*) and depth(*10mm*)
CASE 6	Height (***0.4mm***) with fixed number of Baffles (*4*) and depth(*10mm*)
CASE 7	Height (***0.5mm***) with fixed number of Baffles (*4*) and depth(*10mm*)

Table 4 Baffle Cases and Details

5.1 Effect of Baffles on Velocity Magnitude

The figure 48 shows the velocity in the cathode GDL and CL as a function of the number of baffles, while the figure 49 shows the velocity response as a function of the height of the baffles, with the number of baffles fixed at four. These two parametric sweeps are

combined to separately identify the contribution of the number and intensity of baffle blockages to the reactant transport by convection in the cathode porous layers.

The straight channel (Case 0) had a cathode GDL velocity of 0.003098 m/s, and a cathode CL velocity of 0.002140 m/s, representing the diffusion-dominated transport regime for an unobstructed channel as shown in figure 48. The two baffles (Case 1) produced cathode GDL velocity of 0.008653 m/s and cathode CL velocity of 0.007145 m/s, which were 179.3% and 234.0% higher, respectively, than the baseline. The initial large step indicates that even a small partial blockage is enough to make a fundamental change of the dominant transport mechanism from diffusion to forced convection, which is in line with the results of (Yin et al., 2018) that a single baffle plate is enough to create localised oxygen enrichment zones through convective penetration in the GDL. When the number of baffles increased to three (Case 2), cathode GDL and CL velocities were further increased by 37.1% and 37.8% respectively from case 1 and by 283.1% and 360.1% respectively from the baseline, where velocities were 0.01186 m/s and 0.009843 m/s at cathode GDL and CL respectively. The maximum velocities of 0.014781 m/s in GDL and 0.012313 m/s in CL were obtained with four baffles (Case 3) with further improvement of 24.5% and 25.1% over Case 2 and 377.1% and 475.4% over Case 0, respectively. The progression is nearly linear with each baffle number, meaning that each baffle increases the convective forcing by an approximately constant amount which is physically related to the fact that each baffle produces an independent pressure diversion event that provides an additional through-plane convective flux into the porous electrode. This monotonic increase is in line

with the findings of (Li et al., 2025), which also observed an increase in species transport efficiency with increasing number of baffles, up to an optimum.

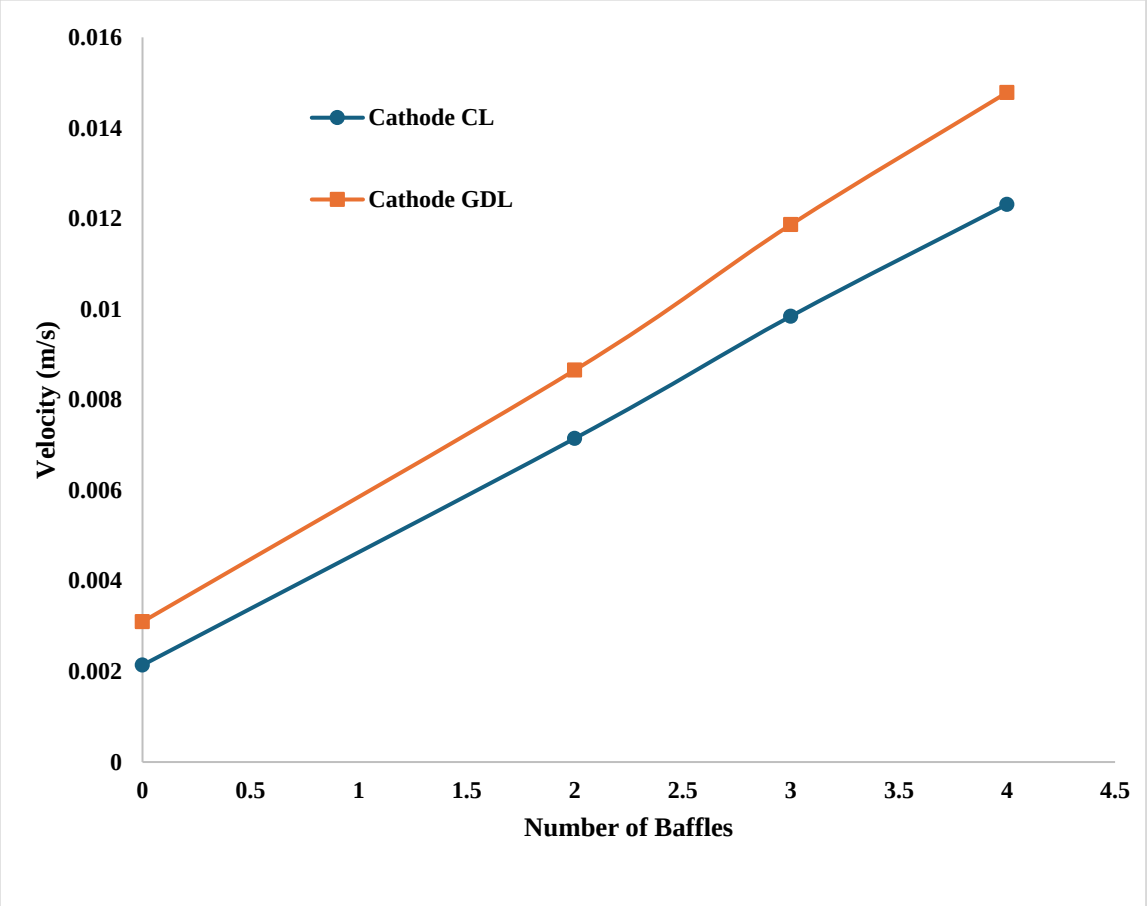

Figure 48 Cathodic Velocities' Behaviour on Number of Baffles

Unlike the linear response to baffle number, there is a clear non-linear exponentially accelerating response to baffle height as shown in figure 49. For Case 4 with h = 0.2 mm, the velocities of cathode GDL and CL were 0.004107 m/s and 0.003074 m/s respectively, which were increased by 32.6% and 43.7% from the base case of straight channel. Interestingly, the CL velocity for this small baffle height (0.003074 m/s), is slightly lower than the baseline GDL velocity (0.003098 m/s), indicating that small baffles generate only a weak local pressure gradient that is inadequate to cause a large amount of convective penetration deep into the porous structure. When height is increased to h = 0.3 mm (Case 5) raised cathode GDL and CL velocities to 0.005650 m/s and 0.004635 m/s, corresponding to increments of 37.6% and 50.8% over Case 4. Further increase to h = 0.4 mm (Case 6) produced velocities of 0.008485 m/s and 0.007175 m/s, representing increments of 50.2% and 54.8% over Case 5. Finally, at h = 0.5 mm (Case 7), the maximum velocities of 0.014781 m/s and 0.012313 m/s were obtained, which were 74.2% and 71.6%

higher than those of Case 6 and 377.1% and 475.4% higher than the baseline velocity. The percentage increases for successive baffle heights are also increasing progressively (from about 33% to 74%) and this further verifies that the relationship between baffle height and induced convective velocity is highly non-linear with the higher baffle height inducing a proportionately higher velocity. This behaviour is controlled by the gap ratio defined by (Soong et al., 2005) and as the baffle height approaches the channel height, the gap ratio decreases sharply and the local flow acceleration through the constricted gap grows exponentially because of the inverse relationship between cross sectional area and velocity imposed by mass continuity.

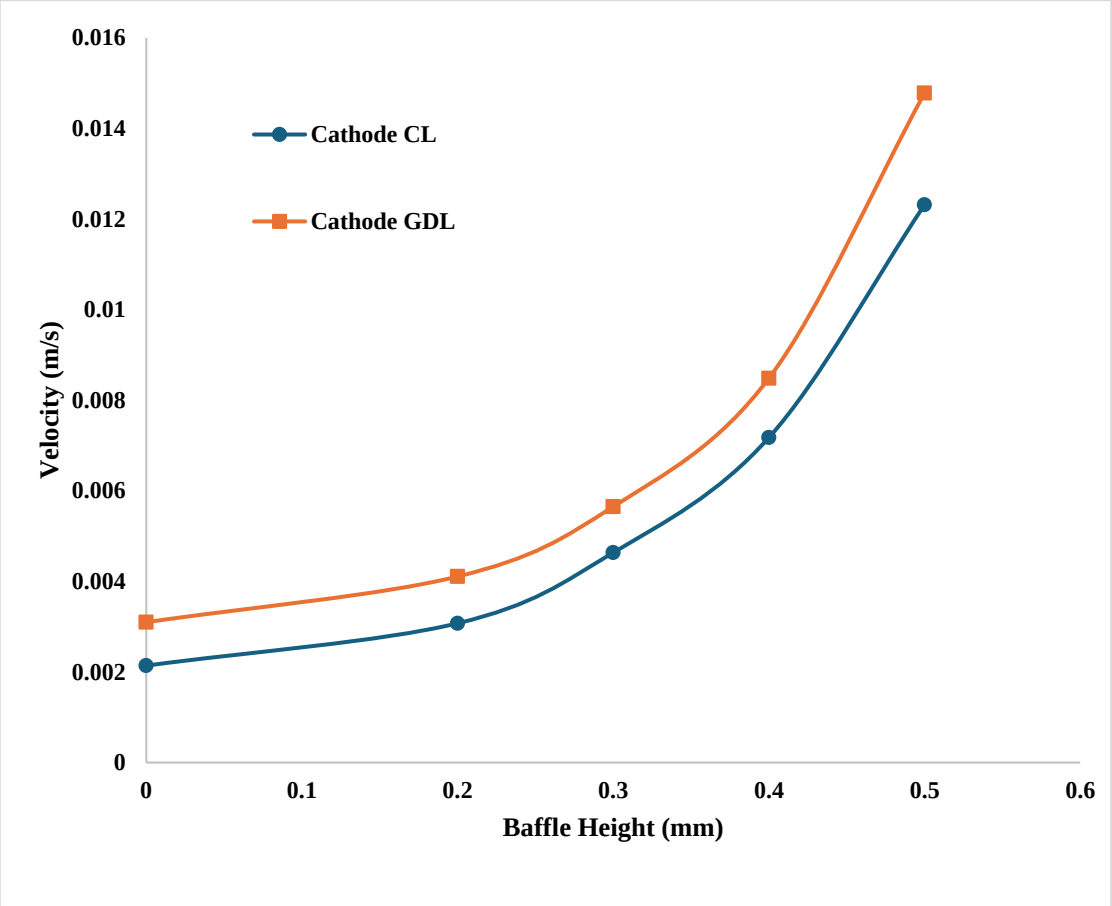

Figure 49 Cathodic Velocities' Behaviour on Baffle's Height

The two parametric sweeps were directly compared, and it is found that baffle height is a more powerful control parameter than baffle number for improving the through plane convective velocity in the cathode porous layers. The resulting velocity change is almost linear as the number of baffles varies from 0 to 4, where the effect of the baffles is to provide a number of relatively weak convection events along the channel, while the velocity change as the height of the baffles at fixed N = 4 is approximately exponential,

due to the strong convection zones created by the baffles being much fewer in number. Both Case 3 (N = 4, h = 0.5 mm) and Case 7 (N = 4, h = 0.5 mm) have the same physical setup and produce the same maximum velocity (0.014781 m/s in GDL and 0.012313 m/s in CL), respectively, thus providing an internal consistency check to verify the reliability of the CFD solution. For both cases, the velocity of the GDL was always about 17–25% higher than the velocity of the CL and this was the same for all baffle configurations. This systematic attenuation between the two porous layers is physically expected since the convective flow passes through the GDL thickness towards the CL and the momentum is dissipated by viscous drag as described by Darcy's law and, at the higher velocities created by the larger baffles.

Overall, the measured velocity trends show both the baffle number and the baffle height to be viable design parameters to improve the delivery of reactants to the catalyst layer and thus directly alleviate the diffusion-limited reactant transport and GDL flooding issues causing concentration overpotential in high current density operation. The height response is however very non-linear, meaning that the baffle height optimisation must be done with more care; the velocity response is very sensitive to the geometric changes, and the design margins and manufacturing tolerances will be closer. This sensitivity, together with the pressure drop penalty associated with it and discussed in the next section, represents the core of the optimisation problem tackled in this work.

The figure 50 shows the velocity magnitude contours in the cathode flow channel and neighbouring porous electrode for the four baffle configurations investigated during the number of baffles sweep at a fixed baffle height of 0.5 mm. The area-averaged velocity analysis quantified the through-plane convective enhancement seen in the peak local velocity, which progressively increases as seen visually from ~25.0 m/s in the base line

straight channel to 35.5, 36.2, and 36.6 m/s for the 2, 3, and 4 baffle configurations, respectively.

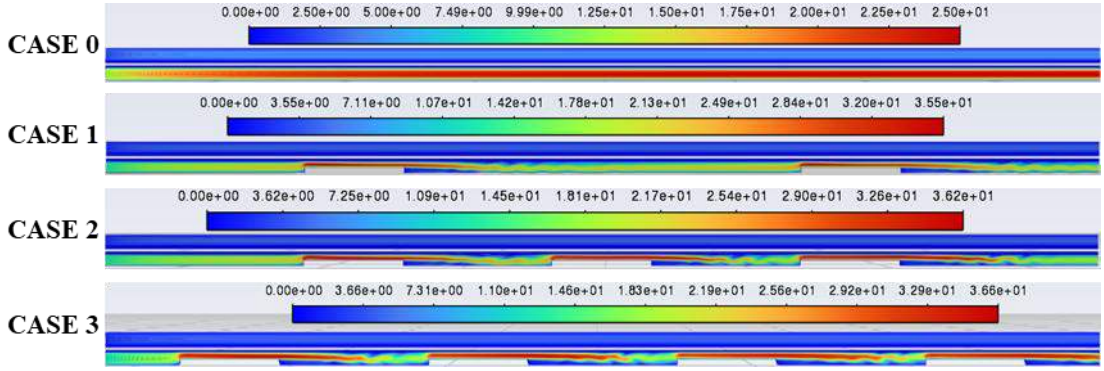

Figure 50 Comparison of Velocity Contours on Different Number of Baffles

Case 0 shows the velocity field is fully developed and same throughout the channel length and negligibly small velocity in the porous electrode under the channel. This validates the assumption by (Soong et al., 2005) and (Yin et al., 2018) that straight channels are characterised by almost exclusively molecular diffusion and that this is the cause of concentration overpotential at high current densities.

Case 1 introduces two baffles, and it creates a completely different flow pattern. Each baffle cross section is lowered to accelerate the mainstream flows as localised red zones immediately above each baffle tip and narrow the channel gap above the baffle.The contours show high velocity penetration directly beneath each baffle into the GDL, meaning that a part of the gas is pushed down into the porous layer instead of flowing along the channel.

While in Cases 2 and 3 additional baffles are added, a greater number of high velocity regions are repeated around the channel length and the convective penetration in the GDL is increasingly significant and spatially distributed. This spread of convective forcing to multiple localized points results in a more uniform supply of reactants along the entire channel, as contrasted to the oxygen starved downstream of the catalyst layer in a conventional channel, which was also noted by (Yin et al., 2018) who observed that the more baffles present, the more uniform the local current density at the catalyst layer.

The figure 51 shows the velocity magnitude contours in the cathode flow channel and the surrounding porous electrode for five baffle heights (h) of 0, 0.2 mm, 0.3 mm, 0.4 mm and 0.5 mm when the baffle count is fixed at four. From the velocity contour analysis, the non-

linear intensification of forced convection with the decrease in gap ratio is quantified, and the peak local velocity progressively increases from ~25.0 m/s in the baseline straight channel to 27.5, 29.3, 32.3 and 36.6 m/s for baffle heights of 0.2, 0.3, 0.4 and 0.5 mm, respectively, offering direct visual evidence.

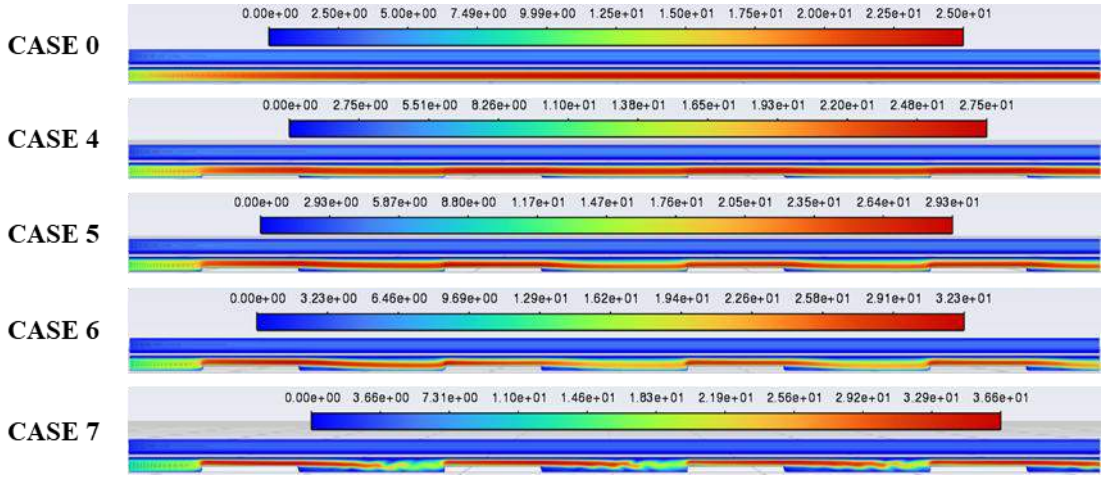

Figure 51 Comparison of Velocity Contours on Different Heights of Baffles

Case 0 corresponds to the velocity field being uniform and fully developed all throughout the channel length and there is negligible velocity in the porous electrode underneath. This is consistent with Soong et al. (2005) and Yin et al. (2018) which reported that diffusion-limited transport is the main contribution to the concentration overpotential at high current densities in the unobstructed configuration. Only a slight difference in flow field with the baseline is observed in case 4 (h = 0.2 mm), where a weak localised acceleration above each baffle is observed and little convective penetration into the GDL occurs. This suggests that at small baffle heights, the gap ratio is still large enough that a significant through-plane convection does not result from the baffles — small baffles are more like passive flow disturbances.

The increase in baffle height (Case 5, h = 0.3 mm and Case 6, h = 0.4 mm) shows contours with progressively stronger constriction of flow above each baffle, and increasingly well-defined, high velocity zones penetrating into the GDL. This is referred to as over-block convection mechanism in the work of (Wang et al., 2020) where the upstream pressure increase of each baffle creates a through plane convective flux which increases as the gap is reduced. This behaviour was formalised by (Soong et al., 2005) when they introduced the gap ratio parameter; it shows that there is an inverse relationship between the cross-sectional area and the velocity, and hence as the gap becomes smaller the local flow

acceleration becomes an increasing exponential. The velocity contour in Case 7 (h = 0.5 mm) show the most aggressive flow field compared to all configurations, with extensive red high velocity zones above each baffle, and deep convective penetration extending across the entire thickness of the porous electrode as would be expected to correlate with the steep velocity rise between Case 6 and Case 7 in the area-averaged data.

Thus, a comparison of contours indicates that the increase in the intensity of forced convection through the gap ratio is a function of baffle height; the two mechanisms of intensification (local flow acceleration through the constricted gap and convective penetration into the porous GDL) all increase with increasing baffle height, and so the velocity enhancement is exponential and the pressure loss is steep.

5.2 Effect of Baffles on Pressure

In all cases the static pressure decreased monotonically from the inlet to the outlet corresponding to the accumulated pressure drop in the cathode channel. Case 0 with no baffle showed an almost negligible and linear variation, as the flow could only interact with the viscous wall friction, and this is consistent for conventional parallel channels as reported by (Perng and Wu 2015) for laminar developed-flow cases. Upon the addition of baffles, the distinctive stepped oscillatory profile was over imposed on the general upward trend, the amplitude of which and the number of oscillations grew with the number of baffles (each dip (tooth shaped) in the graph represents the baffle as case 3 curve has 4 dip because it has 4 baffles), with Case 3 experiencing the steepest overall pressure rise followed by Case 2 and then Case 1 as shown in figure 52.

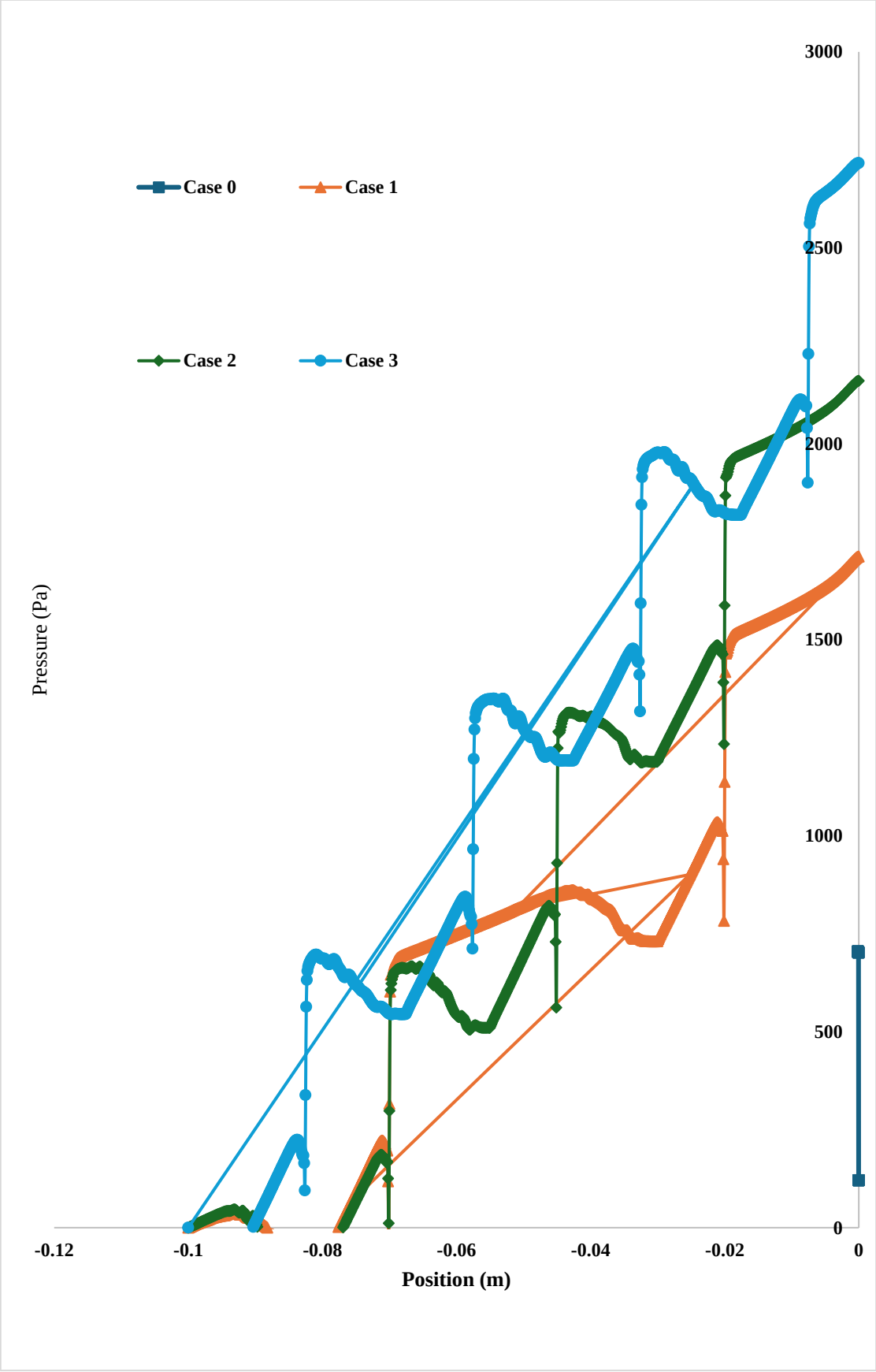

Figure 52 Pressure Drop along the channel length on different number of Baffles

This progressive intensification of the baffle count was because each baffle introduced a separate local loss to the overall pressure budget of the channel (Mohammedi et al., 2020). Each fluctuation in the curve was associated with each baffle and was made up of three distinct features: a pressure jump near the baffle face due to an abrupt area contraction and flow acceleration over the baffle tip; a localised pressure recovery immediately downstream of each baffle as the jet expanded back to the full width of the channel; and a shallow trough corresponding to the recirculation and separation zone created behind each baffle, where the momentum dissipated before reattachment occurred and a pressure increase occurred upstream of the reattached shock. As accounted by (Perng and Wu 2015) and subsequently validated by (Ghasabehi et al., 2024), the main method of baffle conversion of the hydraulic work into forced under-rib convection and irreversible viscous loss is contraction–expansion–recirculation. Thus, the curves showed a saw-tooth shape with decreasing period and increasing peak-to-trough amplitude with increasing baffle count, representing an increasing number of pockets of recirculation along the same channel length and increasing number of loss events as the baffles were increased, consistent with what (Li et al., 2025) observed.

Case 0 as shown in figure 53 (no obstruction) had the same baseline behaviour, with a near flat, friction dominated profile. The qualitative form of the curves for the baffled configurations (Cases 4–7) was retained, meaning that each curve had the periodic sequence of upstream pressure build up, sharp drop in vertical pressure across the baffle and downstream recovery trough, which was found by (Perng and Wu 2015) to be dependent on the channel blockage ratio, but the magnitudes of each feature scaled linearly with the baffle's height. Case 4 (the shorter baffles) had only mild undulations and the lowest overall pressure rise because the baffles were less blocking, which meant that there was less flow acceleration and less strong recirculation zones. Case 5 exhibited slightly more oscillations and a moderately greater increase, and Case 6 exhibited much greater troughs and sharper jumps. Case 7, i.e. the highest baffles presence, showed the most noticeable fluctuations; the largest pressure jumps between the baffles, and the deepest trough after the baffles, and the highest peak values associated with the baffles have been obtained. (Ghasabehi et al., 2024) observed that as the baffle gets closer to the gas-diffusion-layer (GDL) interface, the through plane velocity component increases rapidly, which in turn introduces a larger stagnation pressure on the windward side of the baffle and a larger pull of the wake induced suction on the leeward side; this was the same

mechanism that caused the progressive amplification that was observed here. A higher baffle height thus increased the effective blockage ratio, enhanced the local jetting and separation, and amplified the level of periodic fluctuations in amplitude and the channel pressure drop.

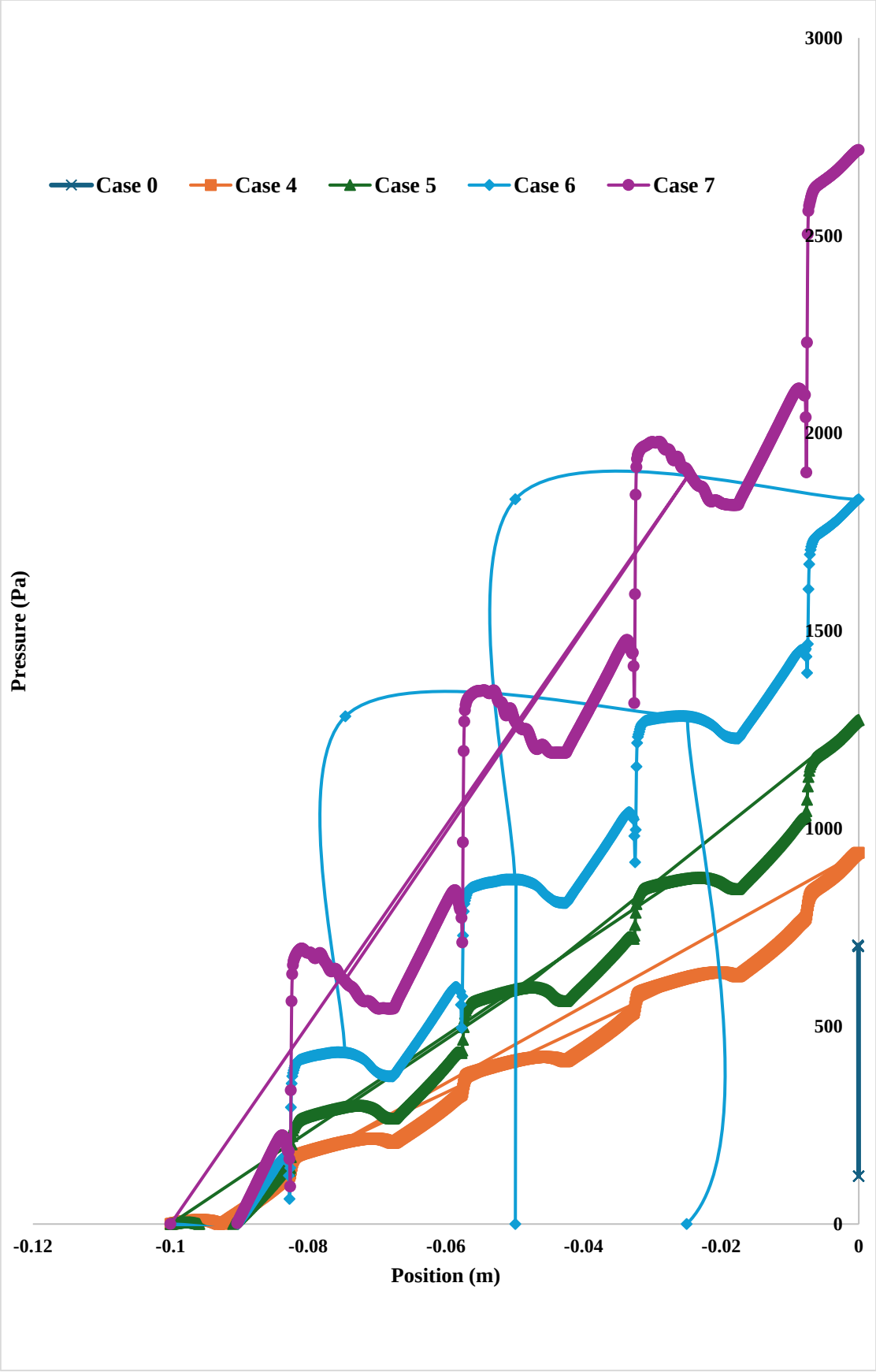

Figure 53 Pressure Drop along the channel length on different baffle heights

The four contour strips in the figure 54 showed the static-pressure field along the cathode channel, with the inlet on the left side to the outlet on the right side of each strip; in each strip red indicated the highest local pressure and blue the lowest with the uniform colour gradient always in the flow direction indicating the expected static-pressure drop from inlet to outlet.

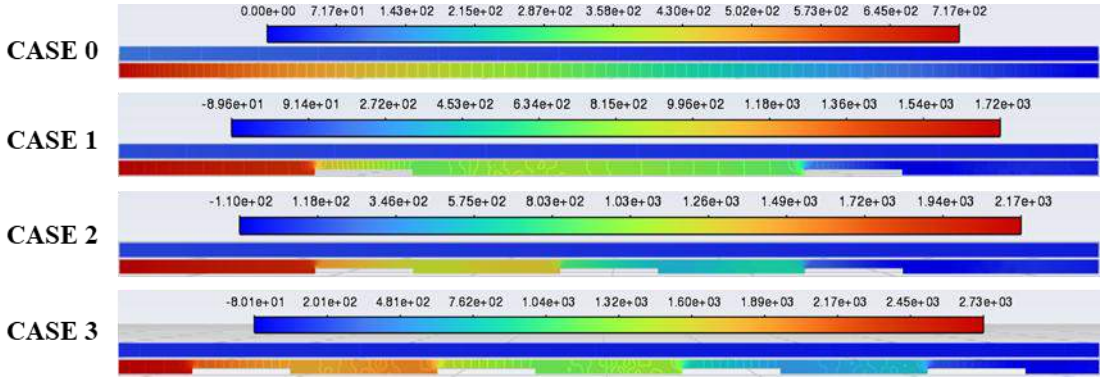

Figure 54 Comparison of Pressure Distribution on Different Number of Baffles

In the un-baffled reference (Case 0) the contour changed gradually and smoothly as a function of the spectral colour band, avoiding any sharp colour breaks, which meant a gradual and almost linear fall in pressure due to viscous wall friction, consistent with the smooth axial profiles reported by (Perng and Wu, 2015). The two baffles (Case 1) was added and gave the contour a clear stepped structure with a band of warmer colours immediately upstream of the baffles and a sharp drop to a cooler band immediately on the leeward side of the baffles, indicating the contraction–expansion event across the baffle. This stepped pattern was periodically repeated along the channel as the baffle count was increased in Case 2 and Case 3, resulting in a series of alternating warm to cool colour blocks, each block representing one baffle, and each interface being a discrete pressure jump. The full colour range also increased gradually from Case 0 to Case 3, suggesting that the inlet to outlet pressure difference also increased as more obstructions were added, and the resulting range of colour, along with the occurrences of the colour discontinuities sharpened and increased in frequency, as would be expected with the addition of a series of localised loss events along the channel, as described by (Mohammedi et al., 2020) and (Ghasabehi et al., 2024). The low-pressure recirculation wake that trailed every obstruction was always on the leeward (downstream) side of each baffle, and the windward (upstream) side was always somewhat warmer.

The five contour strips showed (figure 55) the static-pressure field along the cathode channel, with the inlet (left) at the highest local pressure (red) and the outlet (right) at the lowest local pressure (blue); thus, the predominant gradient is from red at the inlet to blue at the outlet, indicating that the pressure is decreasing in the flow direction as it was expected to.

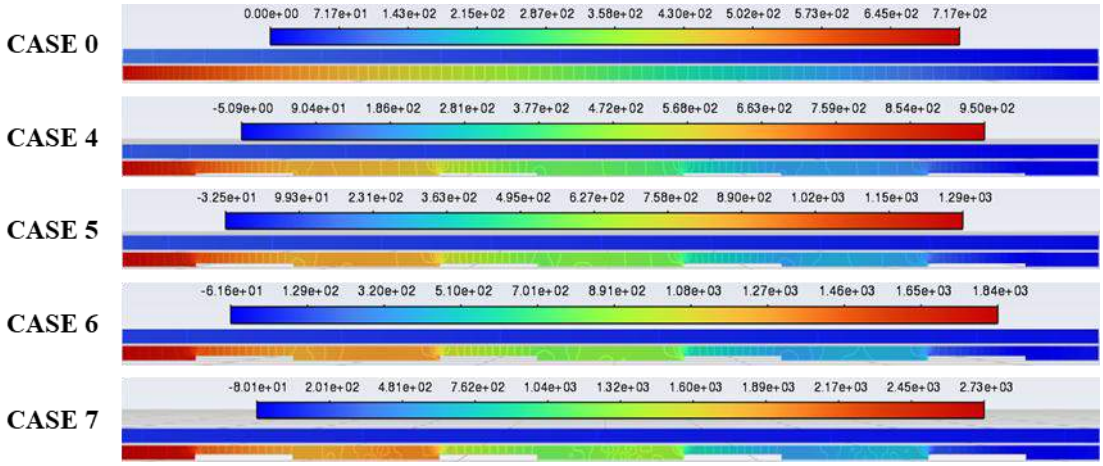

Figure 55 Comparison of Pressure Distribution on Different Heights of Baffles

The un-baffled reference (Case 0) showed the colour to change rather smoothly and almost uniformly with channel length, suggesting a uniform and friction-dominated pressure decay without any localised disturbances, as seen in the laminar developed-flow by (Perng and Wu 2015). With the use of the shorter (Case 4) baffles, weak contraction–expansion events were evident by the appearance of faint stepwise colour discontinuities at the baffle locations; the colour bands on either side of a baffle were only slightly different, indicating a low blockage ratio and a small local pressure jump. This stepwise structure became more pronounced as the baffle height was increased in Case 5 and Case 6, with the warm bands becoming deeper orange in colour upstream of the baffle and the leeward bands becoming noticeably cooler in colour to show the strong jetting over the baffle tip and the strong wake recirculation. For the highest baffles (Case 7) the contour line had the maximum colour discontinuities, where the transition from deep red on the windward side to very cooler bands windward side of each baffle represented the largest local pressure jumps, or the most active wake regions. The overall colour range also increased gradually between the seven cases, Early increment of baffle height resulted in increment of blockage ratio in the channel, which increased both local and cumulative pressure variations across the channel,

consistent with the parametric investigations by (Ghasabehi et al., 2024) and (Li et al., 2025).

Based on the analysis, overall, the Case 3 or 7 (both are with same configuration in this study) (baffle height 0.5 mm, number of baffles 4, baffle depth 10 mm) exhibited the best performance compared to the others. The study resulted in the highest velocity in the cathode catalyst layer, suggesting improved transport of reactants to the electrochemically active portion of the PEM fuel cell. Increased velocity in this area helps to increase oxygen delivery to the cathode catalyst layer where oxygen reduction reaction occurs. This can help to minimize losses in concentrations, increase utilisation of reactants, and enhance the electrochemical performance. According to the results, the level of flow redirection and channel blocking at the particular baffle height is a good balance to enhance penetration of the reactant into the gas diffusion layer to reach the catalyst layer. Thus, the optimum configuration is Case 3 or 7 from the point of view of the velocity of the cathode catalyst layers and the mass transport enhancement.

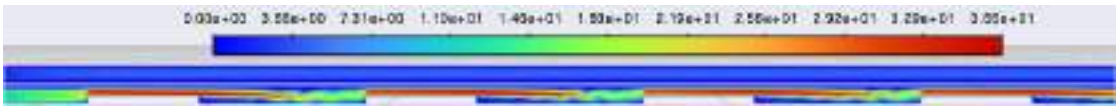

Figure 56 Velocity Contour of Case 3 or 7

Chapter 6: Conclusions, Limitations and Recommendations

6.1 Conclusions

The objective of this study was to examine the transport limitation of reactants in a low-temperature PEM fuel cell by developing a three-dimensional, single-phase, steady-state CFD model using ANSYS Fluent, where the main target was on improving the transport of oxygen at the cathode side in a high current density fuel cell by altering the geometry of rectangular baffle of different height. Each of the six objectives outlined in section 1.5 was met and the findings are summarised below.

The first objective was achieved in the literature review, which revealed that there was a clear gap in the existing literature, that of systematically studying the rectangular baffle height in a cathode-only baffled straight channel with detailed reporting of the pressure and velocity across the GDL, catalyst layer and baffle regions. The second objective was achieved by building a 3D single-phase model whose model independence was verified with the usage of three meshes: 122,300, 220,000, and 500,200 elements; further refinement of the model beyond 122,300 elements did not result in any significant change in the expected polarisation behaviour, thus indicating that numerical convergence was attained based on the work of (Hossain, Islam and Pollard, 2012, Islam, 2012). Indirect validation was done by comparing the results of the predicted polarisation, velocity and pressure trends with the well-known numerical and experimental literature (SIVERTSEN and DJILALI, 2005, Berning and Djilali, 2003, Lum and McGuirk, 2005) surveyed in Chapter 2.

The third objective was achieved by conducting the humidity parametric study, where it was observed that the limiting current density increased from ~0.35 A/cm² (in VLH) to ~1.05 A/cm2 (in VHH) or 200% improvement and also the maximum power density increased from 0.09 W/cm2 to 0.276 W/cm2 or 211% improvement. These results verified that, for straight channel PEMFCs under flooding threshold, hydration level of the membrane is the key parameter for performance and the increasing closeness of HH and VHH curves represented less returns to increase in hydration level as the membrane approached saturation. These results are consistent with the membrane conductivity model developed by (Springer, Zawodzinski and Gottesfeld, 1991) and applied by (Islam, 2012) and confirmed the finding of (Lum and McGuirk 2005) that the membrane hydration is

the most important performance parameter for straight-channel PEMFCs below the flooding limit.

The fourth objective was met with the porosity and permeability sweeps. Because of Bruggeman scaling it was observed that as the GDL porosity was increased from 0.4 to 0.8, the limiting current density increased from ~1.0 A/cm2 to 1.08 A/cm2, but with diminishing returns for GDL porosities greater than 0.6. A value of intermediate permeability, 1.76×10^{-11} m², was kept as the baseline, as it was located in the range of experimentally reported permeabilities for commercial carbon-paper GDLs(SIVERTSEN and DJILALI, 2005), and it did not reach the non-physical convective bypass at the highest permeability.

Two parametric sweeps were used to satisfy the fifth and sixth objectives which both related to baffle height and number of baffles optimisation. As the number of baffles increased, velocities of both the cathode GDL and the cathode CL increased approximately linearly to 0.01478 m/s and 0.01231 m/s, respectively, for the four-baffle case, resulting in 377.1% and 475.4% increases over the unobstructed baseline. In contrast, the velocity response to baffle height was found to be highly non-linear, with the change between heights of 0.4 mm and of 0.5 mm reaching a maximum of 74.2% in the GDL and 71.6% in the CL, a trend that could be explained by the gap area to local velocity inverse relationship required by mass continuity. The resulting pressure loss increased linearly with the blockage, and the blockage created a distinct contraction-expansion-recirculation process each baffle (Perng and Wu, 2015, Ghasabehi et al., 2024). Based on this, the configuration for 4 rectangular 0.5 mm high and 10 mm deep baffles (Case 3 / Case 7) was considered optimal, since it produced the deepest penetration of convection into the GDL and highest velocity of the reactants at the active catalyst surface; the same velocity outputs for Cases 3 and 7, arrived independently via the two sweeps, provided an internal consistency check of the numerical model. Hence, the aim of the project, to improve oxygen distribution to the cathode under high current density operation by systematically varying the parameters, has been fully achieved, both quantitatively and mechanistically.

6.2 Relevance and Impact on Society and the Environment

This work is not limited in its relevance to the computational results. The PEM fuel cell is considered to be a front-runner technology with fuel cell electric vehicle applications and distributed power generation/portable applications and produces only water as a by-

product; however, bipolar plates and the flow field design represent a large share of the overall weight and cost of the fuel cell stack. Any type of geometric optimisation that enhances the utilization of the reactants can directly result into reduced platinum loading, reduced system costs and increased commercial availability. This work proposes a new baffle configuration that achieves a greater than fourfold improvement in through-plane convective velocity in the catalyst layer compared to a straight channel, and points to a practical engineering pathway to realize efficiency improvements in PEMFCs without changing the fundamental material chemistry. The environmental implication is that by making the transport of electrons to the cathode more efficient, it is possible to run the cell at a lower cell voltage compared to the ideal thermodynamic voltage, thus lowering the amount of consumed hydrogen per unit of electrical energy generated, a direct contribution to decarbonisation and the broader challenges of the hydrogen economy.

6.3 Research Limitations

Several limitations are acknowledged. The model was single-phase and steady-state and thus the formation, accumulation and removal of liquid water in the GDLs pores was not captured, so the performance under fully humidified conditions is probably over-predicted and the VHH polarisation curve in Section 4.2 should be considered as an upper bound rather than a fully realistic operating limit. Only baffles on the cathode side were set, and the impact of bilateral baffling on the hydrogen transport and the back-diffusion of water was not investigated in the present work. The geometric envelope chosen for the baffle parametric study was based on a constant height of 10 mm and a constant number of baffles of four, so the generality of the optimisation result is only valid for this constraint. The optimum was chosen through velocity only without a quantitative assessment of a parasitic pumping power penalty. Validation was indirect by comparing with the literature, rather than with a specific experimental data. It was assumed that the temperature at the membrane remains constant, and that the temperature dependency of the membrane conductivity, water phase change and electrochemical reaction is neglected, and the cell was modelled in a one channel configuration without considering stack effect like flow maldistribution between channels and thermal coupling between channels.

6.4 Recommendations

The following recommendations are directly related to the limitations found above. Future work will involve generalizing the present model to a two-phase equation, which includes

liquid water flow, capillary pressure and saturation-dependent diffusivity; with such a model, it is possible to quantify the effect of baffle-induced convection on flooding mitigation under more realistic conditions of high humidity. The indirect validation can be done by an experimental campaign on an instrumented single-cell fixture using the optimal baffle configuration found here, in which the velocity and pressure trends predicted in this work can be compared to the measured polarisation, pressure-drop and, if possible, particle image velocimetry data. However, baffle depth and inter-baffle spacing should also be investigated as design variables in the subsequent parametric studies, in addition to baffle number and height, and other shapes of baffles (e.g. trapezoidal and inverted half-elliptic baffles) (Mohammedi, Sahli and Ben Moussa, 2020, Kaiser et al., 2023), should also be considered along with the optimal baffle height found in this study. Future studies should present a figure of merit, parasitic-power loss assessed through net power density, which equals the gross or stack power minus parasitic power in this case, to ensure that the velocity gain is compared objectively with the parasitic-power loss. Future extensions will include non-isothermal coupling, transient drive cycles representing FCEV duty cycles, and bilateral baffle configuration, to capture the whole range of geometric optimisations. The implication for practice is that for the parametric range studied here, the 0.5 mm rectangular baffle, placed four times over a depth of 10 mm is considered the optimum, giving a directly manufacturable design recommendation for the cathode flow plate manufacturers who want to reduce the concentration losses at high current density, if the resulting higher pressure drop does not exceed the parasitic power budget of the desired application.

References

Abubakar Unguwanrimi Yakubu, Zhao, J., Jiang, Q., Ye, X., Liu, J., Yu, Q. and Xiong, S. (2024). A Comprehensive Review of Primary Cooling Techniques and Thermal Management Strategies for Polymer Electrolyte Membrane Fuel Cells PEMFC. *Heliyon*, 10(19), pp.e38556–e38556. doi:https://doi.org/10.1016/j.heliyon.2024.e38556.

Berning, T. and Djilali, N. (2003). A 3D, Multiphase, Multicomponent Model of the Cathode and Anode of a PEM Fuel Cell. *Journal of the Electrochemical Society*. doi:https://doi.org/10.1149/1.1621412%CD%94.

Chen, H., Guo, H., Ye, F. and Ma, C.F. (2020). An Experimental Study of Cell Performance and Pressure Drop of Proton Exchange Membrane Fuel Cells with Baffled Flow Channels. *Journal of Power Sources*, 472, p.228456. doi:https://doi.org/10.1016/j.jpowsour.2020.228456.

Deng, X., Zhang, E., Lei, J., Jia, D., Liu, Y. and Shuchao, H.E. (2022). Numerical Study on the Effect of an Improved Three-Partition Baffle Flow Field on Proton Exchange Membrane Fuel Cell Performance. *ACS Omega*, 7(47), pp.42872–42882. doi:https://doi.org/10.1021/acsomega.2c04949.

Dutta, S., Shimpalee, S. and Van Zee, J.W. (2001). Numerical Prediction of mass-exchange between Cathode and Anode Channels in a PEM Fuel Cell. *International Journal of Heat and Mass Transfer*, 44(11), pp.2029–2042. doi:https://doi.org/10.1016/s0017-9310(00)00257-x.

Eikerling, M. and Kulikovsky, A. (2014). *Polymer Electrolyte Fuel Cells*. CRC Press. doi:https://doi.org/10.1201/b17429.

Ghasabehi, M., Ghanbari, S., Asadi, M.R., Shams, M. and Kanani, H. (2024). Optimization of Baffle and Tapering Integration in the PEM Fuel Cell Flow Field Employing Artificial Intelligence. *Energy*, 302, p.131884. doi:https://doi.org/10.1016/j.energy.2024.131884.

Hashemi, F., Rowshanzamir, S. and Rezakazemi, M. (2012). CFD Simulation of PEM Fuel Cell performance: Effect of Straight and Serpentine Flow Fields. *Mathematical and Computer Modelling*, 55, pp.1540–1557. doi:https://doi.org/10.1016/j.mcm.2011.10.047.

Hossain, M., Islam, S.Z., Colley-Davies, A. and Adom, E. (2013). Water Dynamics inside a Cathode Channel of a Polymer Electrolyte Membrane Fuel cell. *Renewable Energy*, 50, pp.763–779. doi:https://doi.org/10.1016/j.renene.2012.08.041.

Hossain, M., Islam, S.Z. and Pollard, P. (2012). Numerical Study of the Effect of Effective Diffusivity and Permeability of the Gas Diffusion Layer on Fuel Cell Performance. *Proceedings of the Institution of Mechanical Engineers, Part A: Journal of Power and Energy*, 226(7), pp.907–921. doi:https://doi.org/10.1177/0957650912454402.

Islam, S.Z. (2012). *Computational Fluid Dynamics Modelling of PEM Fuel Cells to Investigate Transport Limitations*. [online] Available at: https://rgu-repository.worktribe.com/output/248204/computational-fluid-dynamics-modelling-of-pem-fuel-cells-to-investigate-transport-limitations [Accessed 27 Apr. 2026].

Jiang, D., Wang, F., Li, X., Tan, J. and Wang, C. (2023). Optimization of Flow Channels in a PEM Fuel Cell Based on a Multiobjective Evaluation. *ACS Omega*. doi:https://doi.org/10.1021/acsomega.3c08298.

Kaiser, R., Ahn, C.-Y., Kim, Y.-H. and Park, J.-C. (2023). Performance and Mass Transfer Evaluation of PEM Fuel Cells with Straight and Wavy Parallel Flow Channels of Various Wavelengths Using CFD Simulation. *International Journal of Hydrogen Energy*, 51, pp.1326–1344. doi:https://doi.org/10.1016/j.ijhydene.2023.05.025.

Kulikovsky, A. and Reshetenko, T. (2026). *A Model for Water Transport in the Membrane and an Impedance Spectroscopy Study of the Effect of Relative Humidity on PEM Fuel Cell Parameters*. [online] Available at: https://www.semanticscholar.org/paper/A-model-for-water-transport-in-the-membrane-and-an-Kulikovsky-Reshetenko/ac2719f27efdf8d0594f1634268653c7178d7176 [Accessed 28 Apr. 2026].

Lee, P.H. and Hwang, S.S. (2009). Performance Characteristics of a PEM Fuel Cell with Parallel Flow Channels at Different Cathode Relative Humidity Levels. *Sensors*, 9(11), pp.9104–9121. doi:https://doi.org/10.3390/s91109104.

Li, S., Zhang, S. and Shen, Q. (2025). Effect of Flow Field with Baffles on Performance of High Temperature Proton Exchange Membrane Fuel Cells. *Journal of Marine Science and Engineering*, 13(3), p.456. doi:https://doi.org/10.3390/jmse13030456.

Liu, X., Tao, W., Li, Z. and He, Y. (2006). Three-dimensional Transport Model of PEM Fuel Cell with Straight Flow Channels. *Journal of Power Sources*, 158(1), pp.25–35. doi:https://doi.org/10.1016/j.jpowsour.2005.08.046.

Lum, K.W. and McGuirk, J.J. (2005). Three-dimensional model of a complete polymer electrolyte membrane fuel cell – model formulation, validation and parametric studies. *Journal of Power Sources*, 143(1-2), pp.103–124. doi:https://doi.org/10.1016/j.jpowsour.2004.11.032.

Min, C.-H. (2009). Performance of a Proton Exchange Membrane Fuel Cell with a Stepped Flow Field Design. *Journal of Power Sources*, 186(2), pp.370–376. doi:https://doi.org/10.1016/j.jpowsour.2008.10.048.

Mohammedi, A., Sahli, Y. and Ben Moussa, H. (2020). 3D Investigation of the Channel cross-section Configuration Effect on the Power Delivered by PEMFCs with Straight Channels. *Fuel*, 263, p.116713. doi:https://doi.org/10.1016/j.fuel.2019.116713.

Nair, A.N., Lal, S. and Vangala, S.P.K. (2025). Understanding the Impact of Flow Fields on the Performance of Direct Methanol Fuel Cells: a Review on Design Trends. *The Chemical Record*, 25(11). doi:https://doi.org/10.1002/tcr.202500025.

Perng, S.-W. and Wu, H.-W. (2015). A three-dimensional Numerical Investigation of Trapezoid Baffles Effect on non-isothermal Reactant Transport and Cell Net Power in a PEMFC. *Applied Energy*, 143, pp.81–95. doi:https://doi.org/10.1016/j.apenergy.2014.12.059.

Pu, J., Xie, Q., Li, K., Wang, Z., Li, C., Li, J. and Zhao, Z. (2026). Overview of Integrated Packaging Single-Cell Technology for Hydrogen Proton Exchange Membrane Fuel Cells. *Energy Storage and Conversion*. doi:https://doi.org/10.59400/esc4141.

Shen, J., Du, C., Wu, D. and Yan, F. (2023). Experimental and Numerical Study of the Enhancement Effects on the Performance of PEMFC with Side Blockage in Straight flow-field. *International Journal of Hydrogen Energy*, 54, pp.1231–1241. doi:https://doi.org/10.1016/j.ijhydene.2023.08.205.

SIVERTSEN, B. and DJILALI, N. (2005). CFD-based modelling of proton exchange membrane fuel cells. *Journal of Power Sources*, 141(1), pp.65–78. doi:https://doi.org/10.1016/j.jpowsour.2004.08.054.

Soomro, I.A., Memon, F.H., Mughal, W., Khan, M.A., Ali, W., Liu, Y., Choi, K.H. and Thebo, K.H. (2023). Influence of Operating and Electrochemical Parameters on PEMFC Performance: a Simulation Study. *Membranes*, [online] 13(3), p.259. doi:https://doi.org/10.3390/membranes13030259.

Soong, C.Y., Yan, W.M., Tseng, C.Y., Liu, H.C., Chen, F. and Chu, H.S. (2005). Analysis of Reactant Gas Transport in a PEM Fuel Cell with Partially Blocked Fuel Flow Channels. *Journal of Power Sources*, 143(1-2), pp.36–47. doi:https://doi.org/10.1016/j.jpowsour.2004.11.055.

Springer, T., Zawodzinski, T. and Gottesfeld, S. (1991). Technical In-formation Bulletins 465-223,465-225, 465-246. 6. P. Wagner. *J. Electrochem. Soc*, 138(8), p.208.

Wang, Y., Pang, Y., Xu, H., Martinez, A. and Chen, K.S. (2022). PEM Fuel Cell and Electrolysis Cell Technologies and Hydrogen Infrastructure Development – a Review. *Energy & Environmental Science*, 15(6). doi:https://doi.org/10.1039/d2ee00790h.

Wei, Y., Feng, Y., Zhao, J., Li, J., Li, H. and Tan, J. (2025). Numerical Investigation of Proton Exchange Membrane Fuel Cells with Symmetrical Serpentine Channels Equipped with Baffles. *ACS Omega*, 10(1), pp.1510–1518. doi:https://doi.org/10.1021/acsomega.4c09174.

Wu, H.-W. and Ku, H.-W. (2011). The Optimal Parameters Estimation for Rectangular Cylinders Installed Transversely in the Flow Channel of PEMFC from a three-dimensional PEMFC Model and the Taguchi Method. *Applied Energy*, 88(12), pp.4879–4890. doi:https://doi.org/10.1016/j.apenergy.2011.06.034.

Xu, C., Wang, H., Li, Z. and Cheng, T. (2022). Effects of the Design and Optimization of Trapezoidal Channels and Baffles (Number and Position) on the Net Power Density of Proton-Exchange Membrane Fuel Cells. *ACS Omega*, 7(5), pp.4214–4223. doi:https://doi.org/10.1021/acsomega.1c05829.

Yi, F., Shu, X., Zhou, J., Zhang, J., Feng, C., Gong, H., Zhang, C. and Yu, W. (2025). Remaining Useful Life Prediction of PEMFC Based on Matrix Long short-term Memory. *International Journal of Hydrogen Energy*, 111, pp.228–237. doi:https://doi.org/10.1016/j.ijhydene.2025.02.302.

Yin, Y., Wang, X., Xiang Shangguan and Zhang, X. (2018). Numerical Investigation on the Characteristics of Mass Transport and Performance of PEMFC with Baffle Plates Installed in the Flow Channel. *International Journal of Hydrogen Energy*, 43(16), pp.8048–8062. doi:https://doi.org/10.1016/j.ijhydene.2018.03.037.

Zhao, J., Tu, Z. and Chan, S.H. (2021). Carbon Corrosion Mechanism and Mitigation Strategies in a Proton Exchange Membrane Fuel Cell (PEMFC): a Review. *Journal of Power Sources*, 488, p.229434. doi:https://doi.org/10.1016/j.jpowsour.2020.229434.